Measurements to Elucidate the Mechanism of Thermal and Radiation Enhanced Diffusion of Cesium, Europium, and Strontium in Silicon Carbide

by

Shyam S. Dwaraknath

A dissertation submitted in partial fulfillment
of the requirements for the degree of
Doctor of Philosophy
(Nuclear Engineering and Radiological Sciences)
in The University of Michigan
2016

Doctoral Committee:

Professor Gary S. Was, Chair
Professor Fei Gao
Professor John W. Halloran
David A. Petti, Idaho National Laboratory

This thesis is dedicated to my family and friends.

Regardless of our history

None of this would be possible without everything you have taught me.

ACKNOWLEDGEMENTS

I would first like to thank my advisor and committee chair, Dr. Gary Was, for his support and guidance in completing this work. I would also like to offer my thanks to the members of my dissertation committee, Dr. John Halloran, Dr. Dave Petti, and Dr. Fei Gaio for their time and insight.

I thank my colleagues Dr. Pantip Ampornrat, Dr. Janelle Wharry, Dr. Anne Campbell, Dr. Cheng Xu, Dr. Mike McMurtrey, Dr. Gokce Gulsoy, Dr. Tyler Moss, Kale Stephenson, Stephen Raiman, Elizabeth Getto, Anthony Monterossa, Justin Hesterberg, Stephen Taller, Gerrit Vancouvering, David Woodley and Drew Johnson for their support and encouragement.

I would like to give special thanks to Dr. Ovidiu Toader and Dr. Fabain Naab for their valuable assistance in performing ion beam analysis and ion irradiations, Dr. Zihua Zhu and Dr. Walter Henderson for their assistance in acquiring and interpreting the SIMS data, Dr. Paul Kotula for acquiring the analytic TEM images and Dr. Anton van der Ven for all the illuminating discussions.

Finally, I would like to thank my family: my late father, K.S. Dwaraknath, my mother, Hemamalini, and my brother, Sudharsan for their continued support.

This work was supported by the Department of Energy under award number NEUP-002-10.

TABLE OF CONTENTS

DEDICATION ii

ACKNOWLEDGEMENTS iii

LIST OF FIGURES vii

LIST OF TABLES xiii

ABSTRACT xv

CHAPTER

I. Introduction 1

II. Background 4

2.1 Silicon Carbide 4
2.1.1 Structure and Defects 4
2.1.2 Radiation Damage Response 6
2.2 Diffusion 7
2.2.1 Fundamentals 7
2.2.2 Bulk vs. Grain Boundary Diffusion 8
2.2.3 Bulk vs. Grain Boundary Diffusion Measurements . 10
2.3 TRISO Fuel 13
2.3.1 Fission Product Release 13
2.3.2 Experiments and Simulations to Isolate Fission Product Diffusion 17
2.4 Objective and Approach 19

III. Experimental Method 32

3.1 Materials 32
3.2 Diffusion Couple Fabrication 33

3.2.1 Substrate Preparation . . . 33
3.2.2 PyC Deposition . . . 34
3.2.3 Fission Product Implantation . . . 35
3.2.4 SiC Cap Deposition . . . 36
3.3 High Temperature Annealing . . . 38
3.4 Ion Irradiation . . . 39
3.4.1 Stage Design . . . 42
3.4.2 Temperature Monitoring . . . 43
3.5 Diffusion Profiling and Calculation . . . 44
3.5.1 ToF-SIMS . . . 44
3.5.2 Diffusion Calculation . . . 45
3.5.3 Error Analysis . . . 47
3.6 Transmission electron microscopy . . . 50

IV. Results . . . 69

4.1 Thermally Annealed Diffusion Couples . . . 69
4.1.1 Strontium . . . 71
4.1.2 Europium . . . 74
4.1.3 Cesium . . . 74
4.2 Ion Irradiated Diffusion Couples . . . 75
4.2.1 Strontium . . . 75
4.2.2 Europium . . . 76
4.2.3 Cesium . . . 76
4.2.4 Interface Concentrations . . . 76

V. Discussion . . . 114

5.1 Diffusion Couple Performance . . . 114
5.1.1 Reproducibility . . . 115
5.2 Fast Diffusion Paths . . . 117
5.3 Thermal Diffusion . . . 118
5.3.1 Bulk Diffusion . . . 118
5.3.2 Grain Boundary Diffusion . . . 119
5.4 Radiation Enhanced Diffusion . . . 122
5.4.1 Bulk Diffusion . . . 122
5.4.2 Grain Boundary Diffusion . . . 123
5.4.3 Point Defect Reaction Model . . . 125
5.5 Comparison with Reactor Data . . . 131
5.5.1 FP Release Data . . . 131
5.5.2 Fission Product Release Modeling . . . 133

VI. Conclusion . . . 162

VII. Future Work 164

BIBLIOGRAPHY 167

LIST OF FIGURES

Figure

2.1 The stacking sequence for 4 different SiC polytypes. The first is 3C-SiC which is the only cubic structure. The second and third are two hexagonal structures with a 4 place and 6 plane repeat sequence. The final is a rhombohedral structure with a 15 plane repeat sequence [13] 23

2.2 Microstructural evolution in 3C-SiC under neutron and ion irradiation [13] 24

2.3 The Fisher model of bulk and grain boundary diffusion where the grain boundary is a thin infinite slab of material embedded in the matrix. This model serves as the basis for all grain boundary diffusion coefficient calculations used today [46, 53]. 25

2.4 Schematic showing the concentration profile evolutions for the three regimes in Harrison diffusion model: (a) Bulk dominant diffusion (b) Combination of grain boundary and bulk diffusion at intermediate temperature (c) Grain boundary dominant diffusion at low temperature. 26

2.5 Arrhenius diagram of bulk diffusion and impurity diffusion in Ag [53] 27

2.6 Arrhenius diagram of grain boundary diffusion and impurity diffusion in Ag [53] 28

2.7 Arrhenius diagram of the segregation factor for impurity diffusion in Ag [53] 29

2.8 Orientation dependence of the diffusivity ($P = s\delta D_{GB}$) of gold in copper [001] tilt symmetric grain boundaries for two different purities of copper: Cu1 and Cu2 at two different diffusion lengths. [58]. . . . 30

2.9 Fractional fission product release from the AGR-1 lab-scale fuel irradiation at the advanced test reactor at Idaho National Laboratoy (INL) [3]. 31

3.1 Electron back scatter diffraction (EBSD) of the Rohm and Hass SiC used in this study. (a) Inverse pole figure in the growth direction (b and c) normal to the growth direction (d) grain size distribution [74] 52

3.2 EBSD inverse pole maps of the four different variants of SiC used in the AGR-1 TRISO Fuel irradiation campaign [75]. 53

3.3 Cu Kα XRD of the SiC substrates provided by Rohm and Haas Inc. All the peaks correspond to β-SiC. The inlay shows the broad plateau near the (111) peak that is characteristic of stacking faults in SiC [74] 54
3.4 Schematic illustration of the four steps in preparing the novel diffusion couple: (a) Preparation of the substrate to create a sharp interface with the PyC (b) Deposition of a layer of CVD PyC (c) Implantation of an FP into the PyC (d) Deposition of a SiC cap to retain the FP within the diffusion couple at high temperature. 55
3.5 A schematic showing orientation of sample in the graphite furnace with reactant flow and vacuum port. 56
3.6 A schematic of the gas flow in newly designed PyC deposition panel fitted for the graphite furnace. Two three way valves allow for reconfiguring the furnace to run thermal annealings as well. Mass flow controllers are used to control the argon-propylene mixture. A vent allows for a constant flow of gas through the system for thermal annealings . . . 57
3.7 RBS spectrum for a 308nm thick PyC layer on a SiC substrate. Green arrow marks the front surface energy for the PyC, while blue arrows mark the width of the carbon plateau from the PyC and the Si edge from the SiC 58
3.8 Implantation range and damage for 400 keV (a) cesium, (b) and (c) strontium into PyC to a fluence of 10^{16} cm^{-2} as simulated by SRIM using a damage energy of 20eV [79, 81]. 59
3.9 RBS spectrum of a diffusion couple for strontium prior to annealing. The front surface energies for the various elements are marked by arrows with dashed green lines. 60
3.10 Schematic of the irradiation chamber. A 4.5 MeV Si^{++} beam is used to irradiate the sample. A Faraday cup that can be inserted directly in front of the sample is used to measure dose. A set of variable slit apertures is used to control the irradiation area. A thermocouple on the stage and the 2D infrared thermal imager are used to monitor temperature. A CCD camera allows for monitoring of the entire setup. An ion gauge placed close to the stage monitors vacuum in the chamber. 61
3.11 A 3D CAD model of the high temperature irradiation stage with the primary parts labeled. 62
3.12 The 2D infrared pyrometer software used to measured the surface temperature of the sample. This is a calibration at 750°C. Note the 3 x 3 array of areas of interest on the sample. An additional area of interest on the graphite shim is used to ensure the beam spread is minimal. 63
3.13 SRIM calculation of 4.5 MeV Si^{++} into the diffusion couple [81]. The layers are differentiated by dashed black lines. Gray lines mark the 10 and 20 dpa dose points which correspond to the PyC/SiC interface and 650 nm into the SiC substrate, where all the radiation enhanced diffusion is limited to. 64

3.14 Weighted recoil spectra for 4.5 MeV Si++ ions and 1 MeV neutrons in SiC. 65
3.15 Temperature deviation within a diffusion couple as a function of depth for an 1,100°C 4.5 MeV silicon ion irradiation 66
3.16 (a) Optical image of a sputter crater from the ToF-SIMS analysis. (b) Optical profilometry scans corresponding to the lines marked 1-5 in (a). The scans have been adjusted to present the deviation from the crater base. Dashed blue lines indicate the analysis area 67
3.17 Flow chart for the diffusion analysis process 68
4.1 ToF-SIMS depth profile of a strontium diffusion couple in the as fabricated case. The silicon profile is used to navigate the layer structure which begins with the SiC cap at the surface, transitions to the PyC between 90s and 520s and finally to the SiC substrate after 520s. The strontium profile is completely contained within the PyC region, ensuring the integrity of the SiC substrate for diffusion analysis. 85
4.2 ToF-SIMS depth profile of the a 1,100°C 10 hour strontium diffusion couple. A calibrated depth scale is also included for just the SiC substrate. 86
4.3 Calibrated and fitted concentration profiles for strontium at 1,100°C for 10 hours exhibiting mixed diffusion kinetics. The steeper depth profile is due to bulk diffusion and the long diffusion tail is due to grain boundary diffusion. 87
4.4 (a) Diffraction contrast image of the PyC/SiC interface and SiC substrate in the 1,100°C:10hr-01 condition shown in Figure 4.2. (b) HAADF image of the same region as (a). (c) EDS map of strontium in SiC in the designated by the red box in (a) and (b). The map presents the normalized EDS intensity across the PyC/SiC interface and in the SiC substrate. An EDS map of the silicon concentration was used to identify the PyC/SiC Interface indicated by the dashed white line. (d) The corresponding 1D depth profile below the PyC/SiC interface in (c) plotted in blue. The equivalant SIMS profile from Figure 4.3 is shown in red for comparison. 88
4.5 Calibrated and fitted concentration profiles for strontium at 900°C for 40 hours exhibiting grain boundary dominant diffusion kinetics. 89
4.6 Calibrated and fitted concentration profiles for strontium at 1,066°C for 10 hours exhibiting mixed diffusion kinetics. The steeper depth profile is due to bulk diffusion and the long diffusion tail is due to grain boundary diffusion. 90
4.7 Calibrated and fitted concentration profiles for strontium at 1,100°C for 10 hours exhibiting mixed diffusion kinetics. The steeper depth profile is due to bulk diffusion and the long diffusion tail is due to grain boundary diffusion. 91

4.8 Calibrated and fitted concentration profiles for strontium at $1,100°C$ for 10 hours exhibiting mixed diffusion kinetics. The steeper depth profile is due to bulk diffusion and the long diffusion tail is due to grain boundary diffusion. 92
4.9 Calibrated and fitted concentration profiles for strontium at $1,100°C$ for 10 hours exhibiting mixed diffusion kinetics. The steeper depth profile is due to bulk diffusion and the long diffusion tail is due to grain boundary diffusion. 93
4.10 Calibrated and fitted concentration profiles for strontium at $1,200°C$ for 10 hours exhibiting mixed diffusion kinetics. The steeper depth profile is due to bulk diffusion and the long diffusion tail is due to grain boundary diffusion. 94
4.11 Calibrated and fitted concentration profiles for strontium at $1,200°C$ for 10 hours. Only the grain boundary diffusion coefficient could be extracted using the formalism for mixed diffusion kinetics 95
4.12 Calibrated and fitted concentration profiles for strontium at $1,300°C$ for 10 hours exhibiting mixed diffusion kinetics. The steeper depth profile is due to bulk diffusion and the long diffusion tail is due to grain boundary diffusion. 96
4.13 Calibrated and fitted concentration profiles for europium at $1,100°C$ for 10 hours exhibiting mixed diffusion kinetics. The steeper depth profile is due to bulk diffusion and the long diffusion tail is due to grain boundary diffusion. 97
4.14 Calibrated and fitted concentration profiles for europium at $1,200°C$ for 10 hours exhibiting mixed diffusion kinetics. The steeper depth profile is due to bulk diffusion and the long diffusion tail is due to grain boundary diffusion. 98
4.15 Calibrated and fitted concentration profiles for europium at $1,200°C$ for 10 hours exhibiting mixed diffusion kinetics. The steeper depth profile is due to bulk diffusion and the long diffusion tail is due to grain boundary diffusion. 99
4.16 Calibrated and fitted concentration profiles for europium at $1,300°C$ for 10 hours exhibiting mixed diffusion kinetics. The steeper depth profile is due to bulk diffusion and the long diffusion tail is due to grain boundary diffusion. 100
4.17 Calibrated and fitted concentration profiles for cesium at $900°C$ for 10 hours exhibiting mixed diffusion kinetics. The steeper depth profile is due to bulk diffusion and the long diffusion tail is due to grain boundary diffusion. 101
4.18 Calibrated and fitted concentration profiles for cesium at $1,100°C$ for 10 hours exhibiting mixed diffusion kinetics. The steeper depth profile is due to bulk diffusion and the long diffusion tail is due to grain boundary diffusion. 102

4.19 Calibrated and fitted concentration profiles for cesium at $1,200°C$ for 10 hours exhibiting mixed diffusion kinetics. The steeper depth profile is due to bulk diffusion and the long diffusion tail is due to grain boundary diffusion. 103
4.20 Calibrated and fitted concentration profiles for cesium at $1,300°C$ for 10 hours exhibiting mixed diffusion kinetics. The steeper depth profile is due to bulk diffusion and the long diffusion tail is due to grain boundary diffusion. 104
4.21 Calibrated and fitted concentration profiles for strontium at $900°C$ irradiated at $4.6 \times 10^{-4} dpa\ s^{-1}$ to 10 dpa over 6 hours. The steeper depth profile is due to bulk diffusion and the long diffusion tail is due to grain boundary diffusion. 105
4.22 Calibrated and fitted concentration profiles for strontium at $1,000°C$ irradiated at $4.6 \times 10^{-4} dpa\ s^{-1}$ to 10 dpa over 6 hours. The steeper depth profile is due to bulk diffusion and the long diffusion tail is due to grain boundary diffusion. 106
4.23 Calibrated and fitted concentration profiles for strontium at $1,100°C$ irradiated at $4.6 \times 10^{-4} dpa\ s^{-1}$ to 10 dpa over 6 hours. The steeper depth profile is due to bulk diffusion and the long diffusion tail is due to grain boundary diffusion. 107
4.24 Calibrated and fitted concentration profiles for europium at $900°C$ irradiated at $4.6 \times 10^{-4} dpa\ s^{-1}$ to 10 dpa over 6 hours. The steeper depth profile is due to bulk diffusion and the long diffusion tail is due to grain boundary diffusion. 108
4.25 Calibrated and fitted concentration profiles for europium at $1,000°C$ irradiated at $4.6 \times 10^{-4} dpa\ s^{-1}$ to 10 dpa over 6 hours. The steeper depth profile is due to bulk diffusion and the long diffusion tail is due to grain boundary diffusion. 109
4.26 Calibrated and fitted concentration profiles for europium at $1,100°C$ irradiated at $4.6 \times 10^{-4} dpa\ s^{-1}$ to 10 dpa over 6 hours. The steeper depth profile is due to bulk diffusion and the long diffusion tail is due to grain boundary diffusion. 110
4.27 Calibrated and fitted concentration profiles for cesium at $900°C$ irradiated at $4.6 \times 10^{-4} dpa\ s^{-1}$ to 10 dpa over 6 hours. The steeper depth profile is due to bulk diffusion and the long diffusion tail is due to grain boundary diffusion. 111
4.28 Calibrated and fitted concentration profiles for cesium at $1,000°C$ irradiated at $4.6 \times 10^{-4} dpa\ s^{-1}$ to 10 dpa over 6 hours. The steeper depth profile is due to bulk diffusion and the long diffusion tail is due to grain boundary diffusion. 112
4.29 Calibrated and fitted concentration profiles for cesium at $1,100°C$ irradiated at $4.6 \times 10^{-4} dpa\ s^{-1}$ to 10 dpa over 6 hours. The steeper depth profile is due to bulk diffusion and the long diffusion tail is due to grain boundary diffusion. 113

5.1 Arrhenius plot for cesium, europium and strontium thermal bulk diffusion. 146
5.2 Arrhenius plot for cesium, europium and strontium thermal grain boundary diffusion. 147
5.3 Cesium bulk thermal and radiation enhanced diffusion. 148
5.4 Europium bulk thermal and radiation enhanced diffusion. 149
5.5 Strontium bulk thermal and radiation enhanced diffusion. 150
5.6 Radiation enhancement for the bulk diffusion of cesium, strontium and europium 151
5.7 Cesium grain boundary thermal and radiation enhanced diffusion. . 152
5.8 Europium grain boundary thermal and radiation enhanced diffusion. 153
5.9 Strontium grain boundary thermal and radiation enhanced diffusion. 154
5.10 Radiation enhancement factor for the bulk and grain boundary diffusion of cesium, strontium and europium 155
5.11 Ball and stick model of the SiC unit cell with carbon in red and silicon in blue labeling (a) the nearest atom distance and (b) the nearest neighbor distance. 156
5.12 Point defect concentrations for SiC under ion irradiation conditions. 157
5.13 Point defect concentrations for SiC under neutron irradiation conditions. 158
5.14 Arrhenius plot for cesium diffusion measured using post-irradiation heating experiments [114–121]. The very low release cesium diffusion coefficients from Myers/Nabielek are circled in red 159
5.15 Same plot as 5.14 with (a) thermal bulk and grain boundary diffusion coefficients from this study plotted in red and blue open circles or (b) the ion irradiated bulk and grain boundary RED coefficients plotted in red and blue open circles and closed circles for the dose rate corrected RED coefficients calculated by assuming that the diffusion coefficient scales by the square-root of the dose rate for a ion irradiation dose rate of $4.6 \times 10^{-4} dpa\ s^{-1}$ and a neutron dose rate of $1.7 \times 10^{-7} dpa\ s^{-1}$ [2]. 160
5.16 Cesium release for 6 compacts that exhibit between 1 and 3 orders of magnitude over-prediction by PARFUME as compared with release measurements made by the deconsolidation-leach-burn-leach method [112]. 161

LIST OF TABLES

Table

2.1 Formation and migration energies for interstitial and vacancies in 3C-SiC 22

3.1 FP Implantation range, FWHM, and peak concentration for cesium, europium and strontium in PyC as calculated by SRIM 2013. RBS measured values are in parenthesis. 51

4.1 Bulk diffusion fits to FP concentration profiles from thermal annealing. χ^2_P is the indicator of goodness of fit. The corresponding p-values are the probability that the fit accurately models the data. The sample naming scheme is as follows: FP-Temperature:time-profile number. The 1100C:10h annealing condition for strontium is the only cause in which multiple diffusion couples were fabricated and annealed. Sr-1100:10h-01 and Sr-1100:10h-02 are from one diffusion couple while, Sr-1100:10h-03 and Sr-1100:10h-04 are from the second. 78

4.2 Grain boundary diffusion fits to FP concentration profiles from thermal annealing. χ^2_P is the indicator of goodness of fit. 79

4.3 Bulk and grain boundary diffusion coefficients for cesium, europium and strontium thermal diffusion. The relative error is the percent of the error in the grain boundary diffusion coefficient from fitting the grain boundary tail. ND indicates values that were not determined. 80

4.4 Bulk diffusion fits to FP concentration profiles from ion irradiation. χ^2_P is the indicator of goodness of fit. 81

4.5 Grain boundary diffusion fits to FP concentration profiles from ion irradiation. χ^2_P is the indicator of goodness of fit. 82

4.6 Radiation enhanced diffusion coefficients for cesium, strontium and europium at a dose rate of 4.6×10^{-3} dpa s^{-1} 83

4.7 The maximum FP concentration on the SiC side of the PyC/SiC interface for the thermal and radiation enhanced diffusion 84

5.1 Bulk and grain boundary diffusion coefficients for cesium, europium and strontium thermal diffusion. The relative error is the percent of the error in the grain boundary diffusion coefficient from fitting the grain boundary tail. ND indicates values that were not determined. The sample naming scheme is as follows: FP-Temperature:time-profile number. The 1100C:10h annealing condition for strontium is the only cause in which multiple diffusion couples were fabricated and annealed. Sr-1100:10h-01 and Sr-1100:10h-02 are from one diffusion couple while, Sr-1100:10h-03 and Sr-1100:10h-04 are from the second. 137
5.2 Activation energies and pre-factors for cesium, europium and strontium bulk and grain boundary diffusion 138
5.3 The segregation energy for FPs assuming that only the elastic strain energy is significant. 139
5.4 Radiation enhanced diffusion coefficients for cesium, strontium and europium at a dose rate of 4.6×10^{-3} dpa s^{-1} 140
5.5 Activation energies and pre-factors for bulk and grain boundary RED of cesium, europium and strontium. 141
5.6 Reaction rate coefficients for the point defect reaction model. 142
5.7 Diffusion coefficients for the point defect reaction model. 143
5.8 Quantities for the point defect reaction model. 144
5.9 Activation energies and pre-factors suggested by the IAEA TECDOC-978 compared with activation energies and pre-factors for bulk and grain boundary diffusion measured in this study. [1]. 145

ABSTRACT

Measurements to Elucidate the Mechanism of Thermal and Radiation Enhanced Diffusion of Cesium, Europium, and Strontium in Silicon Carbide

by

Shyam S. Dwaraknath

Chair: Gary S. Was

Containment of fission products (FP) within the TRISO fuel particle is critical to the success of the very high temperature reactor (VHTR). Over sixty years of experience developing and testing this fuel has yet to identify the mechanism by which several key fission products (cesium, europium, and strontium) escape through intact SiC at temperatures between 900°C and 1,300°C.

A novel diffusion couple was developed that was successful in making the first measurements of fission product diffusion in SiC. This design allows for the isolation of thermal diffusion and investigation of radiation enhanced diffusion using ion irradiation as a simulant for neutron radiation damage. The thermal and radiation enhanced diffusion of cesium, europium, and strontium were measured between 900°C and 1,300°C. The ion irradiation significantly enhanced the diffusion of all three fission products with enhancement factors ranging from 100× to 10^7× over thermal diffusion.

All three fission products exhibits mixed diffusion kinetics between 900°C and 1,300°C under purely thermal conditions, and between 900°C and 1,100°C under ion irradiation. This indicates that both bulk and grain boundary diffusion are active

mechanisms for fission product release. A defect reaction model indicates that fission product diffusion can occur on both the silicon or carbon sub-lattices. Comparison of cesium diffusion with the literature suggests that the best quality TRISO fuel should exhibit minimal cesium release and that cesium release is a good indicator of TRISO fuel failure.

CHAPTER I

Introduction

Current very high temperature reactor (VHTR) designs use TRISO fuel to permit operation at temperatures over 900°C. The TRISO fuel design consists of a kernel of nuclear fuel that is coated with a layer of pyrolytic carbon (PyC), silicon carbide (SiC) and a final layer of PyC. The SiC layer serves as the diffusion barrier that prevents fission product (FP) release. Past national fuel qualification programs have discovered that several fission products are able to escape the fuel particle through intact SiC and that the release behavior of some of these FPs does not correlate with any environmental variables. The FPs silver, palladium, and europium appear to penetrate the SiC layer most easily [1–5]. Experience operating and testing TRISO fuel has revealed significant in-pile silver release [2–7] with little to no out-of-pile release [7–10] suggesting that irradiation is a key factor. More recently, transmission electron microscopy (TEM) analyses of irradiated TRISO fuel have revealed a spatial correlation of silver and palladium [2, 3, 9] There is little consistent information on europium and strontium [2, 11], while palladium has not been measured until very recently. There is no consensus on the mechanism of FP diffusion or the key variables that affect it, even for the known releasers such as silver, palladium and europium [3, 6]. Cesium, europium and strontium are all known releasers with significant radiological health concern [12].

Several hurdles have impeded progress in understanding the FP diffusion process. First, the temperatures of interest, 900°C to 1,600°C, are well above the melting or boiling point of the FPs of interest, making traditional diffusion couples very difficult to construct. Secondly, while FPs are able to migrate through intact SiC, the expected solubilities in SiC are limited, making their detection difficult. These first hurdles have been addressed by ion implanting FPs into SiC and then heat treating the SiC to measure the diffusion of FPs. Unfortunately, this introduces the FP at well over the solubility and introduces trapping sites via radiation damage, which results in a heterogeneous microstructure of precipitates inlayed in the SiC with little to no mobility for the FP. The subsequent diffusion measurements are several orders of magnitude slower than what is expected from fuel release data. Third, the data from fuel test programs can be divided into either in-pile release data or out-of-pile accident test data. The in-pile data is valid for understanding the radiation enhanced diffusion process, but is more limited in time as there are no in-situ techniques to monitor FP release from fuel. The out-of-pile accident test data forces the fuel to higher temperatures to accelerate the diffusion process and is actively monitored in-situ, resulting in more detailed information, but is only valid for understanding the thermal diffusion process. To validate against both sets of data, the thermal diffusion process must first be isolated and measured, followed by the radiation enhanced diffusion process.

This thesis aims to identify the mechanism of transport for three key FPs: cesium, europium and strontium through SiC under thermal and radiation enhanced conditions using a novel diffusion couple developed to overcome the hurdles of direct ion implantation experiments and conventional diffusion couples. Chapter 2 introduces background on SiC and the relevant microstructure, then diffusion theory and how it is measured, before focusing on TRISO fuel, FP release data and attempts to isolate diffusion. Chapter 3 provides the experimental procedure involved in fabricating the novel

diffusion couples, the details of the high temperature annealing treatments, ion irradiations to investigate RED and the diffusion analysis using time-of-flight secondary ion mass spectrometry (ToF-SIMS). Chapter 4 presents the results of this extensive investigation. Chapter 5 discusses the results and contextualizes the diffusion data with respect to the FP release data. Chapter 6 presents conclusions and recommendations for future work.

CHAPTER II

Background

This chapter reviews the published literature relevant to the understanding fission product diffusion in SiC and provides the context for the experimental study and discussion. Section 1 reviews the properties of SiC relevant to this thesis. Section 2 reviews diffusion theory, the measurement methodologies and diffusion in similar systems. Section 3 reviews the current state of TRISO fuel, the fission product release data and attempts to isolate diffusion. The final section states the objective of this thesis and outlines the approach to understanding fission product diffusion.

2.1 Silicon Carbide

2.1.1 Structure and Defects

SiC is a wide bandgap high temperature ceramic with a variety of different structures or polytypes depending on the stacking sequence of the silicon-carbon planes as depicted in Figure 2.1. The bonding in SiC is primarily covalent in nature, but there is a small ionic component due to a difference in electro-negativity. The microstructure and corresponding properties of SiC are a strong function of the fabrication route. Only chemical vapor deposition (CVD) is able to produce highly crystalline, pure and stoichiometric SiC, which is critical for irradiation stability [13]. Many of the polytypes of SiC are hexagonal or rhombohedral in nature, but only one

is cubic: β-SiC or 3C-SiC, where 3 represents the number of stacks to repeat the structure and C indicates it is cubic. It has a zinc-blende lattice structure, which is two interpenetrating FCC lattices offset by a quarter of the body diagonal. All other structures are classified together as α-SiC. β-SiC is the preferred polytype for radiation environments due to its superior radiation damage tolerance [13].

Several different defects can form in SiC including vacancies, interstitials and anti-site defects on either sub-lattice with varying charges. No experimental measurements exist for either the formation or migration energy for defects in 3C-SiC. Since SiC is a semiconductor, the formation and migration energies are strong functions of the Fermi-level, which depends on the type and amount of impurities. Formation energies for vacancies and interstitials calculated using density functional theory (DFT) show large variations depending on the simulation parameters. For silicon, the vacancy formation energies range from 5 eV to 10.7 eV and interstitial formation energies range from 3 eV to 9 eV, with the neutral $< 110 >$ split dumbbell being the most stable interstitial configuration [14–22]. Vacancy migration barriers range from 2.4eV to 3.6eV while interstitial migration barriers range from 1 to 1.4 eV. For carbon, the vacancy formation energies range from 3.5 to 7 eV, and interstitial formation energies range from 4.5 to 9.5 eV, with the neutral $< 100 >$ split dumbbell being the most stable. Vacancy migration barriers range from 3.5 to 5.2 eV, while interstitial migration barriers range from 0.2 to 1.7 eV. DFT calculations of anti-site defect formation energies have shown very little variation, ranging from 3.5eV to 4eV, in comparison with vacancy and interstitial formation energies. Table 2.1 lists the defect formation and migration energies used here. The lowest formation energy neutral defects were chosen as the most appropriate for this study.

2.1.2 Radiation Damage Response

Displacement energies for a two component system such as SiC depend on the sub-lattice and the direction. The displacement energy varies from 18 to 71 eV for carbon and from 36 to 113 eV for silicon [23–40], while the most widely used direction-averaged values are 20 eV for carbon and 35 eV for silicon [41]. This difference in displacement energies for silicon and carbon in the SiC system creates an asymmetry in the displacement efficiencies with a ratio as high as five to one carbon to silicon displacements [24, 28, 29, 32, 34, 38, 41–43]. Nearly ten percent of all defects are anti-site defects, which are more stable than sub-lattice vacancies and interstitials [27, 28, 32, 37, 44, 45]. The peak cascade displacement count increases as a function of temperature which counteracts the increase in defect annihilation as a function of temperature and results in a nearly constant number of Frenkel pairs after the cascade has quenched as a function of temperature. SiC also exhibits a lack of cascade clustering in comparison to metallic systems [27, 28, 43].

Microstructural evolution in cubic SiC has three distinct regimes [13]. Figure 2.2 diagrams these various microstructural observations in these three regimes as a function of temperature and dose. Black dot damage and small loops are observed at low temperature and/or fluence. Larger loop populations and Frank loops are observed at intermediate temperatures over 800°C and at moderate fluences on the order of a dpa to a few 10's of dpa. At very high doses, large dislocation loop networks are observed as well as significant void density. SiC swells at all temperatures despite the lack of voids at low temperatures and doses. Below the critical amorphization temperature (150°C), the strain induced by amorphization causes SiC to swell, but saturates at approximately 10%. Above this temperature, the strain induced by immobile point defects causes SiC to swell and the saturation swelling decreases with increasing irradiation temperature. Above 900°C vacancies becomes mobile and begin to cluster into voids. Depending on the irradiation conditions, SiC has been observed

to exhibit breakaway swelling as low as $1,000°C$ due to void growth.

2.2 Diffusion

2.2.1 Fundamentals

Solid state diffusion is the movement of atoms due to a gradient in chemical potential. Fick's first and second laws govern diffusion and are stated as:

$$J = -M\nabla\mu \tag{2.1}$$

$$\frac{\partial C}{\partial t} = -\nabla \cdot M\mu \tag{2.2}$$

In an ideal system, the diffusion coefficient is independent of the concentration and the chemical potential is directly proportional to the concentration. The proportionality constant, the chemical activity, is absorbed into the diffusion coefficient:

$$\begin{aligned} \mu &\propto \gamma C \\ J &= -D\nabla C \\ \frac{\partial C}{\partial t} &= D\Delta C \end{aligned} \tag{2.3}$$

There are two environmental variables that could control diffusion: temperature and radiation. Diffusion could be a purely thermal process in which the magnitude increases with temperature. Radiation can affect diffusion by producing additional defects that will accelerate the diffusion of atoms. In either case, the diffusion coefficient follows an Arrhenius relationship:

$$D(T) = D_0 exp\left(-\frac{E_A}{kT}\right) \tag{2.4}$$

This expression requires both an activation energy (E_A) for migration and a pre-factor (D_0). These definitions are used when the diffusion mechanism is not known or can not be specified.

The diffusion coefficient for bulk diffusion is:

$$D_B(T) = D_0^B exp\left(-\frac{E_A^B}{kT}\right) \tag{2.5}$$

where D_0^B is the pre-factor for bulk diffusion and E_A^B is the activation energy for bulk diffusion. The diffusion coefficient for grain boundary diffusion is:

$$D_{GB}(T) = D_0^{GB} exp\left(-\frac{E_A^{GB}}{kT}\right) \tag{2.6}$$

where D_0^{GB} is the pre-factor for grain boundary diffusion and E_A^{GB} is the activation energy for grain boundary diffusion.

2.2.2 Bulk vs. Grain Boundary Diffusion

This thesis will focus on bulk and grain boundary diffusion as the two primary mechanisms of diffusion as these are the most likely mechanisms for over-sized solute diffusion.

The Fisher model has been used to describe the interplay between bulk and grain boundary diffusion [46]. In this model, shown schematically in Figure 2.3, the grain boundary is a high diffusivity, uniform, and isotropic slab embedded in a low-diffusivity isotropic bulk crystal. No assumptions in grain boundary structure such as orientation or crystallinity are made. The impurity atoms are introduced at the surface and diffuse into either the bulk or into the grain boundary. Impurity atoms are further allowed to diffuse from the crystal into the grain boundary or vice-versa.

Harrison subdivided this model into three classical regimes: Type A, where bulk diffusion dominates, Type C where grain boundary diffusion dominates and Type B

where both are comparable [47]. Figure 2.4 shows these three regimes schematically in a simple polycrystalline material where the grain boundaries are separated by the grain size (d), and the grain boundaries have a finite width (δ).

Type A diffusion is a limiting case regime of high temperature, long anneal times, or small grain sizes. In all three cases the bulk diffusion front is large enough to cross more than one grain. In this regime, the bulk diffusion distance is greater than the spacing between grains: $\sqrt{D_B t} >> d$. Tracer atoms are able to visit many grains during the anneal time. The result is a system that obeys a single effective diffusion coefficient:

$$\textbf{Type A: } D_{eff} = D_b \tag{2.7}$$

Type C diffusion is the other limiting case, in which the particles travel only via grain boundaries. Since there is no bulk diffusion, the effective diffusion coefficient is the grain boundary diffusion coefficient.

$$\textbf{Type C: } D_{eff} = D_{gb} \tag{2.8}$$

Type B diffusion is the most complex, and describes the case where grain boundary diffusion transports particles much further than bulk diffusion, but the overall mass transport through the two mechanisms is comparable. This is the mixed diffusion regime. Mathematically it is bound by the grain size and the grain boundary width: $s\delta << \sqrt{D_B t} << d$, where s is the segregation factor defined as the concentration in the grain boundary divided by the concentration in the bulk directly adjacent to the grain boundary and δ is the grain boundary width. As a result, particles are able to move directly through the grain boundary, directly through the bulk crystal, through the grain boundary and then the bulk , or through the bulk and then the grain boundary. In this regime, Fick's law is observed within the bulk and within the

grain boundary, but the overall diffusion length is proportional to $t^{1/4}$ rather than $t^{1/2}$. Concentration profiles in this regime contain enough information to extract the bulk diffusion coefficient (D_b) and the term $s\delta D_{GB}$, which is the product of the grain boundary segregation factor, the grain boundary width, and the grain boundary diffusion coefficient.

The grain boundary width and segregation factor are important characteristics in understanding the atomistics of diffusion near and along grain boundaries. The grain boundary width is relatively constant, and has been measured to be between 0.5 nm and 2 nm for both self-diffusion and solute diffusion [48]. The segregation factor is the ratio of solute atom concentration in the grain boundary to that in the bulk. It is a thermodynamic quantity that drives equalization of the chemical potential at the interface to that in the bulk. In the dilute limit it follows the Henry isotherm which follows an Arrhenius relationship with a segregation energy E_s that shows up as part of the grain boundary activation energy for mixed diffusion measurements.

2.2.3 Bulk vs. Grain Boundary Diffusion Measurements

There is a large body of literature investigating bulk and grain boundary diffusion in other systems. This work is a useful comparison to justify the model, bound diffusion in SiC, and understand the atomistics of bulk vs. grain boundary diffusion.

Several systems have been studied using single and polycrystalline substrates to isolate bulk and grain boundary diffusion. In general, these studies have proven the validity of the Fisher model and Harrison regimes as means of understanding this interplay [49–55]. There has also been some work looking at the interplay of conventional bulk diffusion and fast pipe diffusion [51,55–57]. While the Fisher model should apply here, the relative diffusivities in fast pipes, such as stacking faults and dislocations, vs. the matrix does not seem to vary widely enough to create the different regimes exhibited by bulk and grain boundary diffusion [55]. This effect has

been isolated to well controlled single crystal samples, and has been shown to be an enhancing factor for bulk diffusion in polycrystalline material [56].

Most of the work performed on bulk and grain boundary diffusion is limited to the bulk dominant or mixed diffusion regimes [53]. As temperature rises, the solubility of tracer atoms in the material increases, allowing for lower sensitivity analysis methods. The grain boundary diffusion dominant regime is the lowest temperature region, which results in very low solubility. Grain boundaries constitute a small fraction of the sampled volume. These two aspects make grain boundary diffusion measurements extremely difficult for all but model systems. It is still necessary to make measurements in this regime to fully characterize grain boundary diffusion and extract the grain boundary diffusion coefficient. It has only been a few years since reliable systematic Type C regime measurements have been made due to the production of carrier free radiotracers and proliferation of extremely sensitive detectors with large counting efficiency and low background [53].

Few measurements have been made in the grain boundary diffusion dominant regime due to their difficulty, and are limited to model systems such as silver in copper or nickel in silver [53]. The diffusion of impurities in silver has been heavily studied across all three diffusion regimes [49–52]. Figure 2.5-2.7 show the bulk diffusion coefficient, the grain boundary diffusion coefficient, and the segregation factor for self-diffusion as well as nickel, selenium, and tellurium diffusion in silver. The segregation factor is calculated from the grain boundary diffusion coefficient in the Type C and Type B regimes. Nickel and selenium are undersized solutes, while tellurium is an over-sized solute. Selenium is weakly segregating, while tellurium is strongly segregating to grain boundaries. While they both have high bulk diffusivities , the strong segregation behavior of tellurium retards its grain boundary diffusivity in comparison with selenium. The strong segregation behavior is an indication of a trapping effect that degrades grain boundary diffusion.

Diffusion measurements in polycrystalline samples probe the full spectrum of available grain boundaries, resulting in an average grain boundary diffusion measurement. Experiments with bi-crystals have been used to study grain boundary diffusion as a function of grain boundary character. Orientation dependence of the grain boundary diffusion coefficient can either be monotonic or have minima and maxima corresponding to special orientations. Initial work investigating silver self-diffusion pointed to monotonic dependence [51]. More recent work investigating gold diffusion in copper with very fine step size in the misorientation angle shows local minima at the perfect $\Sigma 5$ orientation [58]. Figure 2.8 shows the results of this study as a plot of the GB diffusivity ($P = s\delta D_{GB}$) of gold vs the tilt angle for [001] symmetric tilt bi-crystals in copper with two different purities at two different temperatures and annealing times. The grain boundary diffusivity exhibits a discontinuity at the perfect $\Sigma 5$ orientation and a minima at 36.5°.

There is a significant body of work investigating diffusion in bulk crystalline material. Diffusion models such as Kirkendall, Inverse-Kirkendall, and interstitial drag rely on the binding of solutes to defects to explain how impurity atoms are able to move about in the lattice. The atomistics of grain boundary diffusion are far more complex. Ignoring the complexities of grain boundary structure, the atomistics of grain boundary diffusion are still in their infancy [59, 60]. DFT and kinetic Monte Carlo models have revealed some key points. The formation and migration energies in grain boundaries are far lower than in the matrix and are highly site specific. At low temperatures, well below the melting temperature, a defect mediated model of diffusion in the grain boundary seems to still apply, but is complicated by the heterogeneity of nucleation of defects and the multiplicity of diffusion paths. The correlation factors are far more complicated due to the diversity of structure and the migration barriers associated with an evolving path as defects themselves play an important role in grain boundary structure. At high temperatures the presence of

large concentrations of defects makes understanding grain boundary structure, and the corresponding migration barriers very difficult. This is likely the case under irradiation as there is a large super-saturation of defects and a large flux of defects to sinks such as grain boundaries.

2.3 TRISO Fuel

2.3.1 Fission Product Release

While coated particle development began in the 1960's with the British program for their advanced gas reactors (AGR), significant experience fabricating and operating TRISO fuel did not accumulate until it was chosen as the reference fuel for the German high temperature gas reactor (HTGR) program due to the poor performance of BISO fuel in containing FPs [1]. BISO Fuel consists of a fuel kernel that is coated with a layer of low density carbon and a PyC layer. This design was successful in retaining gaseous fission products but did nothing to stop solid fission product release. TRISO was designed to retain solid fission products as well, but several FPs were observed to penetrate through presumably intact SiC. Of these, only silver was quantified due to its erratic release behavior. Using a 1D diffusion analysis Nabielek et al. [61] was able to show that both the fractional release of silver and diffusion times correlated well if the diffusion coefficient in the SiC was assumed to have the same activation energy as the uranium oxide fuel (218 $^{kJ}/_{mol}$), but a factor of 100 higher value of D_0. At the time, it was not possible to pinpoint a diffusion mechanism in SiC that would have this activation energy.

Bullock et al. [8, 62] measured diffusion coefficients in post irradiation annealing experiments with fuel from the HRB-15b irradiation capsule as part of the first US HTGR program in the 1980's. TRISO fuel with UO_2, UC_2, and UCO, all with 88% to 90% uranium loading, were irradiated in the High Flux Isotope Reactor (HFIR)

to a burn up of 20% fissions per initial metal atom (FIMA) at 900°C in several capsules. Irradiation Microsphere Gamma Analysis (IMGA) indicated that TRISO particles from capsule HRB-15b retained their full cesium and silver inventories during irradiation. Post-irradiation annealing experiments were then conducted between $1,200$°C and $1,500$°C up to 10,000 hours. Cesium was retained in all particles containing intact SiC, which provided a convenient method to separate diffusion of other fission products through intact and failed SiC. UO_2, UCO, and UC_2 particles released varying degrees of silver between $1,200$°C and $1,500$°C, with release fractions as high as 65%. Diffusion coefficients were calculated assuming diffusion in the SiC was rate limiting resulting in an activation energy of 410 $^{kJ}/_{mol}$. The release of silver varied greatly from particle-to-particle rather than by fuel type, which suggested that the kernel fuel type did not affect silver release and that the SiC layer was the only inhibiting layer. If the lack of cesium release was in fact an indicator of intact SiC, then most of the released silver had to diffuse through the SiC. No effort was made to analyze strontium or europium.

More recently, Van der Merwe [5,11] analyzed silver release data from the German HGTR program as well as analysis performed by ORNL on irradiated fuel from that program. He was able to determine that 98% of the silver release was in particles with intact SiC, while the remaining 2% could be accounted for by 2 factors: natural uranium and thorium contamination of the graphite and defective SiC coatings. By considering the error in chemical deconsolidation techniques as well as the IMGA data provided by ORNL, he was able to calculate a design limit in-pile silver diffusion coefficient and an activation energy. The calculated activation energy was a factor of 4 smaller than the value derived from post irradiation annealing treatments by Bullock et al. at 109 $^{kJ}/_{mol}$ and a factor of 2 smaller than the than accepted value of 218 $^{kJ}/_{mol}$ reported by the IAEA [1]. The large difference in calculated diffusion coefficients from various national fuel programs can have two sources: large differences

in the quality of the TRISO fuel itself, or large differences in an intrinsic property of the SiC. It has been theorized that differences in SiC coating parameters could create different grain boundary networks, in both the distribution of grain boundary character and location that could account for this large variation, which would affect the diffusion of all solid FPs including cesium, strontium, and europium.

As part of the Japanese HTGR program, Minato et al. [6] have looked closely at fission product profiles using energy disperse x-ray (EDS) analysis in TRISO fuel 5 years after irradiation in the Japan Materials Test Reactor (JMTR) between $1,200°C$ and $1,500°C$ with up to 5% burn up FIMA. Palladium had accumulated at the interface between the inner PyC and SiC and in some cases had corroded the SiC, which results in a mixture of palladium silicide and excess carbon : $SiC + 2Pd <-> Pd_2Si + C$ [63]. Other noble metals that are known to corrode SiC, such as ruthenium and rhodium, were not detected near the SiC but primarily in the kernel. Silver was not detected within any of the TRISO coatings. The lack of sensitivity of EDS does not preclude the possibility that silver was in the TRISO coatings at concentrations below what EDS could detect, but it does indicate that silver does not segregate into precipitates in any of the TRISO coatings above the detection limits of EDS.

In the late 1980's, Schenk et al. [62] measured fission product concentrations in cross section using electron micro-probe analysis (EPMA) on fuel irradiated in a variety of reactors, including the High Flux Reactor (HFR) at Petten, the AVR, the Dido reactor at Julich, and the HFR at Grenoble, only to find that silver was in the inner PyC and kernel at concentrations of approximately 0.01% but not in the SiC or the outer PyC. He then performed post-irradiation annealings up to 1,900°C with silver release fractions between 5% and 90% and examined the particles with EPMA afterwards. EPMA profiles showed significant penetration of palladium and ruthenium at higher temperatures. Cesium was detected in the SiC in particles

annealed at 1,900°C, but not at 1,700°C or lower. Small amounts of silver were detected in the inner PyC in particles annealed at 1,600°C, regardless of the silver release fraction. This suggests that silver solubility in SiC is extremely low. The high temperatures necessary for cesium to penetrate SiC suggest that cesium solubility and diffusion in SiC are also very small, but do not verify that a lack of cesium release is an indicator for intact SiC for in-pile measurements where radiation can greatly enhance both the solubility and diffusion.

More recently, the Next Generation Nuclear Plant (NGNP) program has had success in producing lab scale and industrial scale TRISO fuel and irradiating it in the Advanced Test Reactor (ATR) to 20% burn up FIMA between 1,000°C and 1,200°C [5]. Figure 2.9 presents the fractional release of fission products from the AGR-1 test campaign completed at Idaho National Laboratory (INL) broken into three sections, in-pile release, release to the test train, release during high temperature annealing [3]. Lab-scale TRISO fuel was produced at INL and Oak Ridge National Laboratory (ORNL). The test-fuel was then irradiated at the Advanced Test Reactor for 2 years, before being analyzed for fission product release. The first section shows the range of fission product release during irradiation. A dashed line signifies the amount of fission product that would be released if a single particle was to fail and release its full fission product inventory. Some of the fuel was subjected to thermal annealing at elevated temperatures to simulate accident conditions. The fission product release from these annealings is shown in the third section of Figure 2.9.

Preliminary isotopic assay of the graphite holders showed significant amounts of silver release with large variations from compact to compact. Significant amounts of palladium and lesser amounts of europium were also released from the TRISO particles into the graphite holders. Gamma assay of the TRISO particles themselves showed silver release fractions ranging from 0% to 60%. It was acknowledged that there were significant temperature gradients in the test trains and that the fuel could

have seen up to 300°C differences in temperature depending on their radial and axial location. Post-irradiation annealing of the compacts showed a large release of silver upon ramp up to 1,250°C, followed by no release at high temperature [2]. The amount of silver released in the annealing corresponded well with the amount of silver that should have been in the graphite matrix in the compact due to release from the TRISO particles during irradiation. Significant amounts of europium, palladium, and strontium were also released from the TRISO particles during post-irradiation annealing, greater than what would have been in the graphite. There was a correlation in the europium and strontium release fractions, suggesting that the transport mechanism for these fission products was the same. Electron microscopy revealed a large number of palladium, uranium and silicon rich precipitates at the interface between the inner PyC and the SiC with smaller palladium precipitates extending as far as a few μm into the SiC [9]. Silver was identified in one precipitate at a triple junction suggesting that palladium played a role in silver transport. Cesium and rhenium were also identified in these precipitates. The post-irradiation and in-pile release data from this program provides the most complete picture of what could be occurring for several FPs (cesium, europium, and strontium) that have had little focus in the past.

2.3.2 Experiments and Simulations to Isolate Fission Product Diffusion

Nabielek et al. [61] attempted to isolate silver diffusion through SiC by ion implanting silver into SiC plates produced in the same furnace used to coat SiC onto the fuel particles, and annealed them at 1,180°C for 30 minutes. Rutherford backscattering spectroscopy (RBS) analysis of the silver concentration profiles before and after annealing showed no change in the silver concentration profile, indicating that silver was immobile. The diffusion coefficient for the ion implantation experiment was bounded by a maximum value of $10^{-19} m^2 s^{-1}$, which is two orders of magnitude lower than what was expected if the previous 1D analysis of silver release from TRISO fuel

was valid.

Using a mesoscale kinetic monte carlo (KMC) model Meric de Bellefon [64] showed that a network of fast and slow diffusion paths could account for the variability in the diffusion coefficient of silver. Shrader et al. [14] showed that bulk diffusion of silver through SiC can be ruled out due to the extremely large barrier for silver to enter solution in SiC. His calculations also showed that the formation energies for defect silver complexes, including the formation energy of the defect itself, were relatively large (up to 9 eV), but their migration barriers were small. This suggested that if an auxiliary process such as radiation damage could form these complexes, then the resulting bulk diffusion would be very fast.

MacLean et al. [65] suggested that nano-cracks could be the fast transport paths. She annealed silver ion implanted SiC samples at temperatures up to $1,500°C$ for up to 500 hours and observed no change in the silver concentration profiles. From this, she concluded that silver did not diffuse in SiC. Rather, using a subset of the silver release data from the German HTR program, she showed that above a critical temperature of $962°C$ (the melting temperature of silver), there was a marked increase in the in-pile silver release fraction for previous TRISO campaigns. This suggested a gas phase transport mechanism, and since the release was through intact SiC, the network of mechanical pathways (nano-cracks) was too small to resolve. No direct evidence of gas-phase transport or the presence of nano-cracks was presented.

Recently, Honorato-Lopez et al. [66, 67] showed that silver could diffuse along the grain boundaries in SiC at higher temperatures. They trapped a thin layer of silver between two layers of SiC in a spherical diffusion couple. The outer layer of SiC was deposited using a low temperature polymer pyrolysis technique, so it was not considered in further analysis. Silver was observed in the form of nodules along grain boundaries at temperatures as low as $1,200°C$ in the inner SiC. Unfortunately, they did not take into account the ability of pure silver to dissolve silicon from SiC [68],

which in turn acts as a mechanism for the injection of vacancies that could enhance transport in SiC.

Another proposed process relies on the corrosive nature of palladium, which is produced in much higher yield than silver, to provide for a transport process into and through SiC [6, 69, 70]. Palladium was co-deposited onto SiC substrates via physical vapor deposition (PVD) and then annealed at 900°C to 1,000°C. Both palladium and silver were observed to penetrate along grain boundaries past the reaction front for palladium-SiC corrosion. Correlation of palladium nodules ahead of silver nodules along grain boundaries was used as evidence for a chemically enhanced transport process. Still, these experiments have not considered the dependence of transport on concentration and none have been in the 1,100°C to 1,300°C temperature range of interest to an operating VHTR, or up to 1,600°C, which would mimic more closely the out-of-pile release experiments [71].

The only conclusive result seen in the literature is that silver transport in direct ion implanted SiC is several orders of magnitude slower than what is seen in either post-irradiation annealing or in-pile release of TRISO fuel [10, 61, 65, 72]. While diffusion couples have had limited success in providing clues to the underlying transport mechanisms, they have only focused on silver. No consensus exists on a process of silver transport in TRISO fuel, with or without irradiation. No mechanistic understanding of cesium, europium, or strontium transport through SiC exists in the published literature.

2.4 Objective and Approach

The objective of this thesis is to determine the mechanism of transport for cesium, europium, and strontium through SiC under prototypical very high temperature reactor (VHTR) conditions.

This work will focus on cesium, strontium and europium diffusion beacuse of their

importance for licensing from a radiological health perspective [73], their significant release as observed by the NGNP program [2] and the similarities and differences in their chemical behavior. There are two environmental variables that could control FP transport through SiC: temperature and radiation. While palladium could enhance FP transport by altering the local microstructure and chemistry, the evidence from TRISO irradiations suggests that this may only occur with silver, not cesium, strontium or europium. Further, FP release measurements by the NGNP program reveal that in-pile strontium and europium release are comparable with release from out-pile accident tests at temperatures of 300°C to 500°C higher than irradiation conditions [2]. This suggests that the effect of radiation is dominant and will be the primary focus of this thesis.

There are many pathways through which FPs could potentially be transported through SiC. Three of the most likely pathways/mechanisms are bulk diffusion, grain boundary diffusion, and vapor transport along nano-cracks. The majority of the SiC volume is made up of grains, each of which constitutes a single crystal. FP diffusion through the bulk of the SiC crystal is therefore an obvious potential pathway for escape. While grain boundaries represent a substantially smaller fraction of the SiC volume, their more open structure along with the disruption in bonding can raise both the mobility and local thermodynamic solubility of FP (through segregation). If nano- or micro-cracks are present, they would constitute very fast short-circuit diffusion pathways for FP. Transport along interconnected crack networks can occur either through surface diffusion, or in gaseous form.

While nano-cracks are a convenient mechanism to explain the variability in silver release, their existence is still speculative. Our own research has shown no evidence of interconnected nano/micro-cracks in representative SiC substrates as observed by both HRTEM and helium porisimetery, which can resolve surface porosity down to tens of nanometers. Furthermore, a network of nano-cracks would be mechanically

similar to a large crack in the SiC. This would facilitate the release of all FPs, which is not necessary for significant europium, palladium, silver, or strontium release.

A systematic study to determine the mechanism for FP diffusion first has to determine the pre-factors, and activation energies for both bulk and grain boundary diffusion. Then the diffusion coefficients can be calculated as a function of temperature under purely thermal and irradiation conditions. Comparison of the diffusion coefficients for bulk and grain boundary diffusion will then yield which mechanism is dominant under various conditions.

Lattice	E_f^v (eV)	E_m^v (eV)	E_f^i (eV)	E_m^i (eV)
Silicon	5.9 [22]	2.65	6.0 [16]	0.74 [37]
Carbon	6.8 [22]	2.82	6.3 [16]	1.53 [37]

Table 2.1: Formation and migration energies for interstitial and vacancies in 3C-SiC

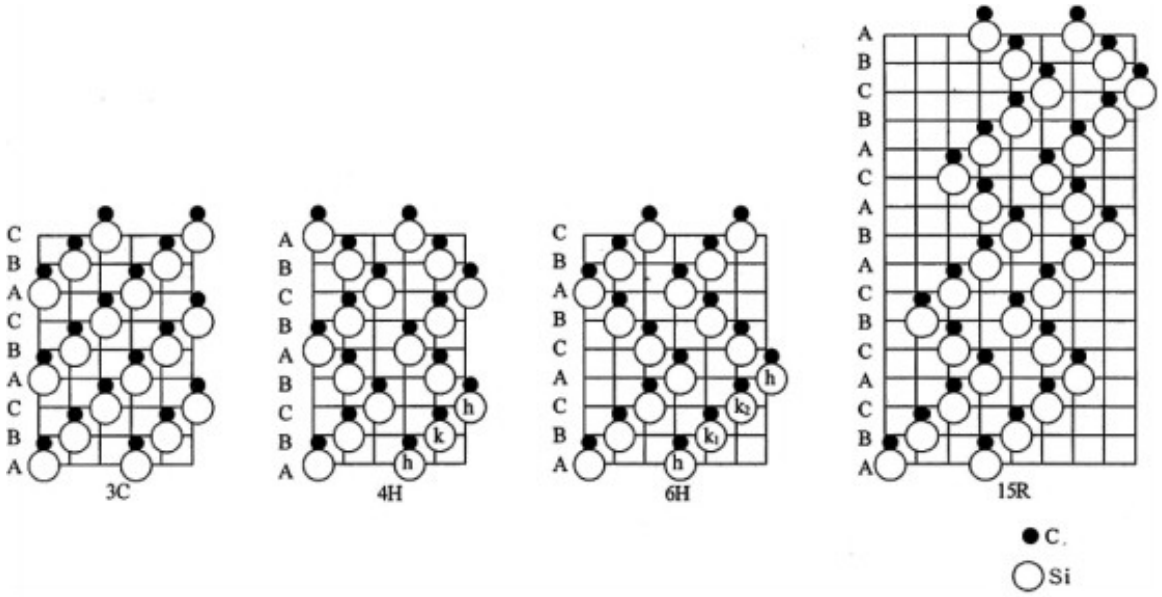

Figure 2.1: The stacking sequence for 4 different SiC polytypes. The first is 3C-SiC which is the only cubic structure. The second and third are two hexagonal structures with a 4 place and 6 plane repeat sequence. The final is a rhombohedral structure with a 15 plane repeat sequence [13]

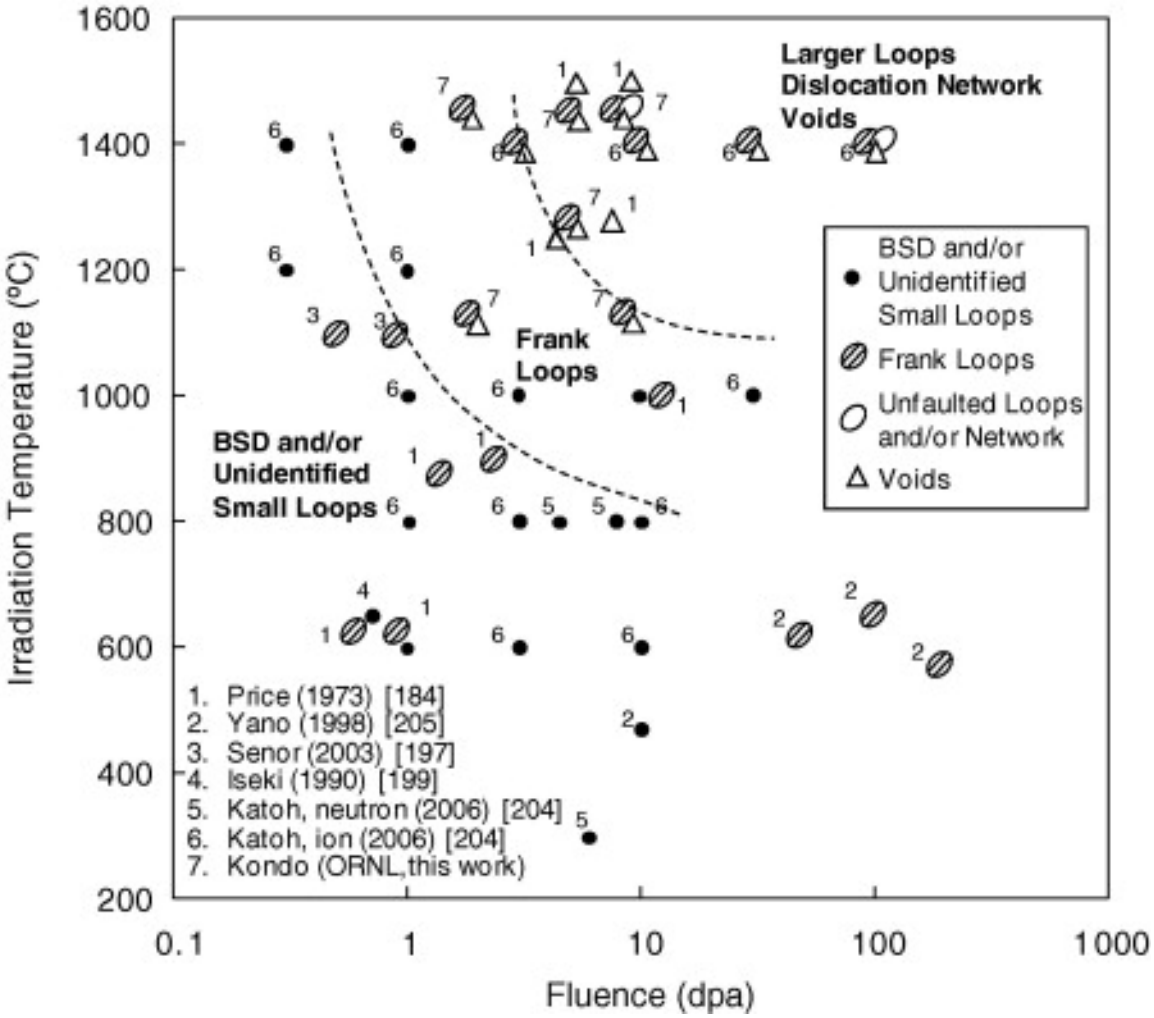

Figure 2.2: Microstructural evolution in 3C-SiC under neutron and ion irradiation [13]

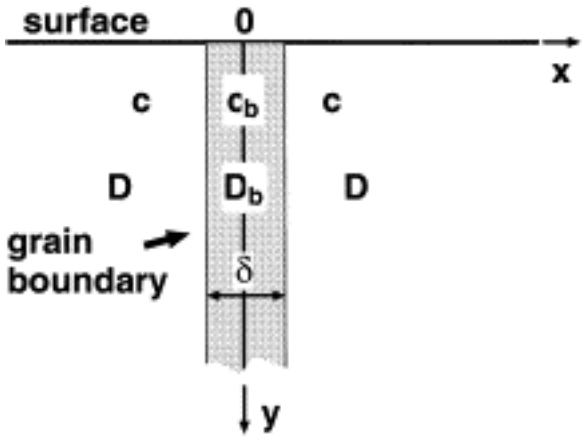

Figure 2.3: The Fisher model of bulk and grain boundary diffusion where the grain boundary is a thin infinite slab of material embedded in the matrix. This model serves as the basis for all grain boundary diffusion coefficient calculations used today [46,53].

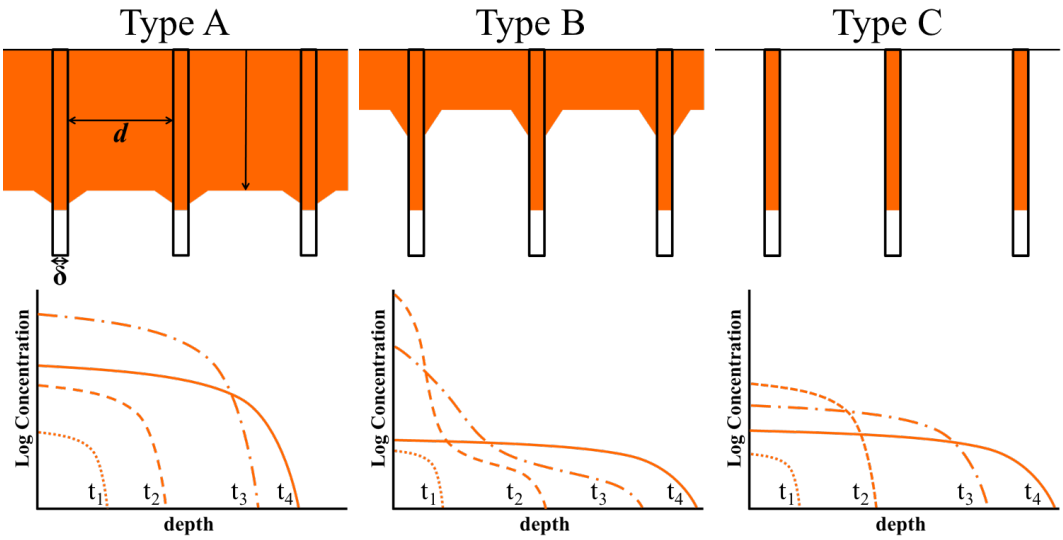

Figure 2.4: Schematic showing the concentration profile evolutions for the three regimes in Harrison diffusion model: (a) Bulk dominant diffusion (b) Combination of grain boundary and bulk diffusion at intermediate temperature (c) Grain boundary dominant diffusion at low temperature.

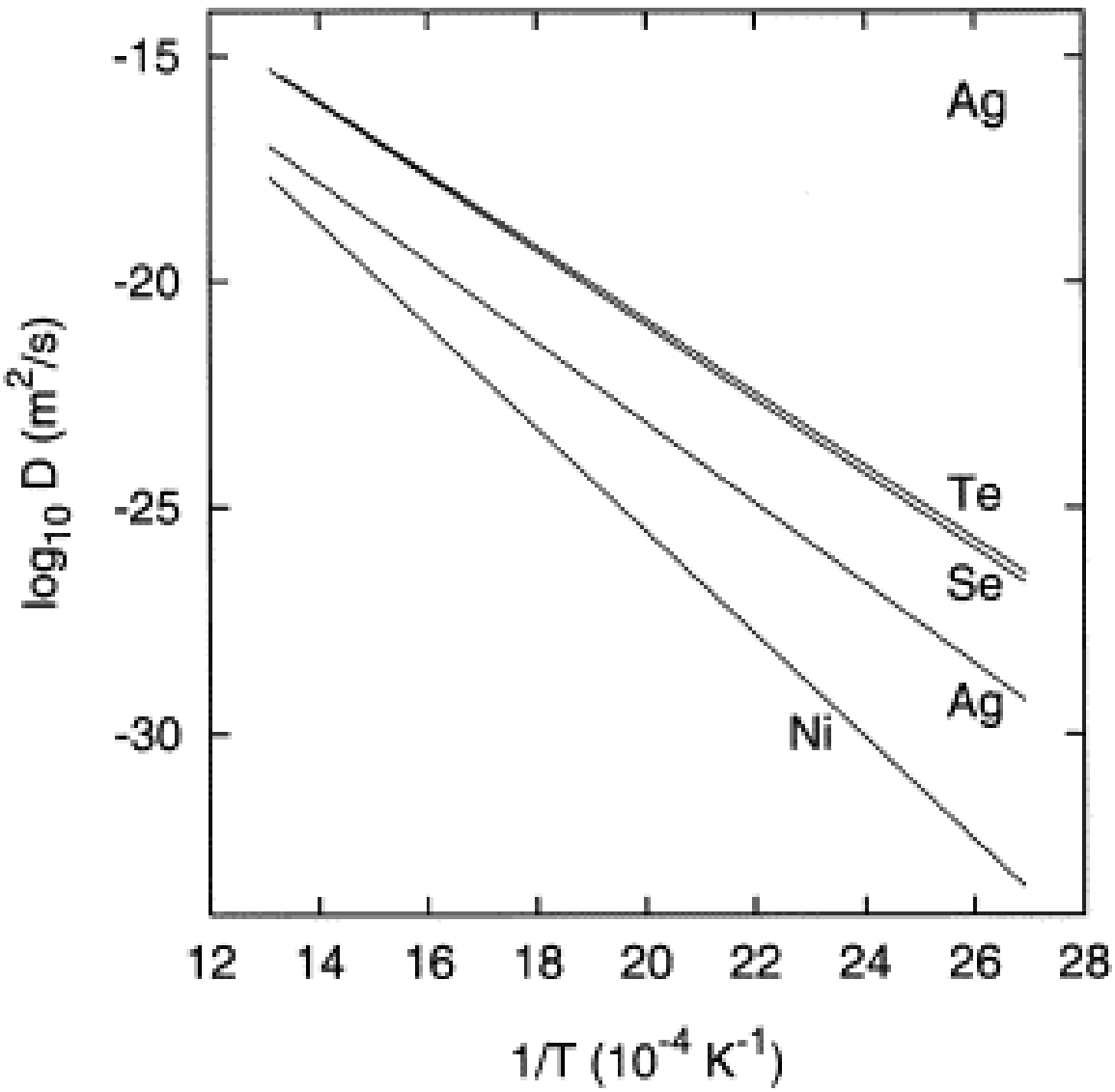

Figure 2.5: Arrhenius diagram of bulk diffusion and impurity diffusion in Ag [53]

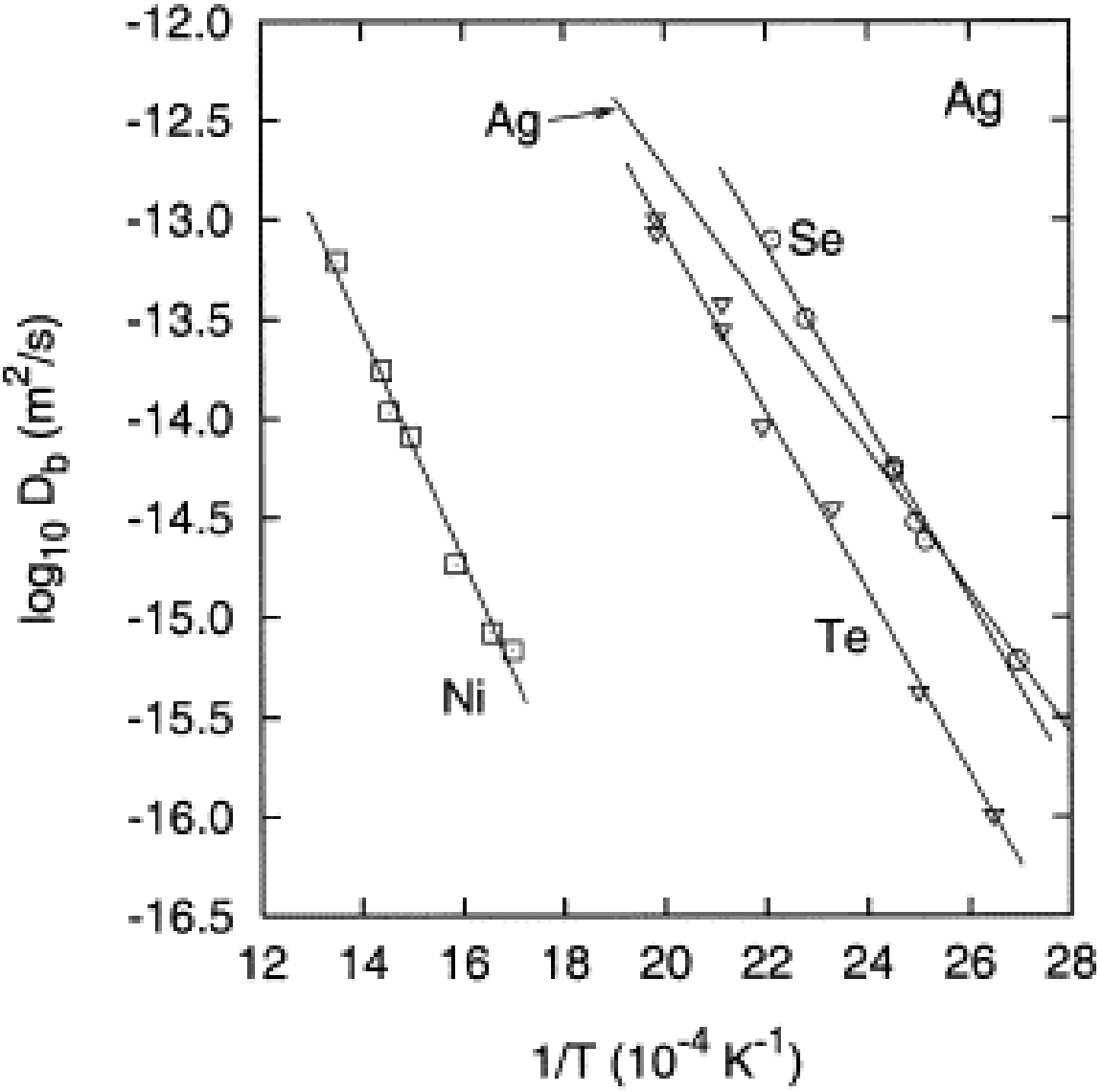

Figure 2.6: Arrhenius diagram of grain boundary diffusion and impurity diffusion in Ag [53]

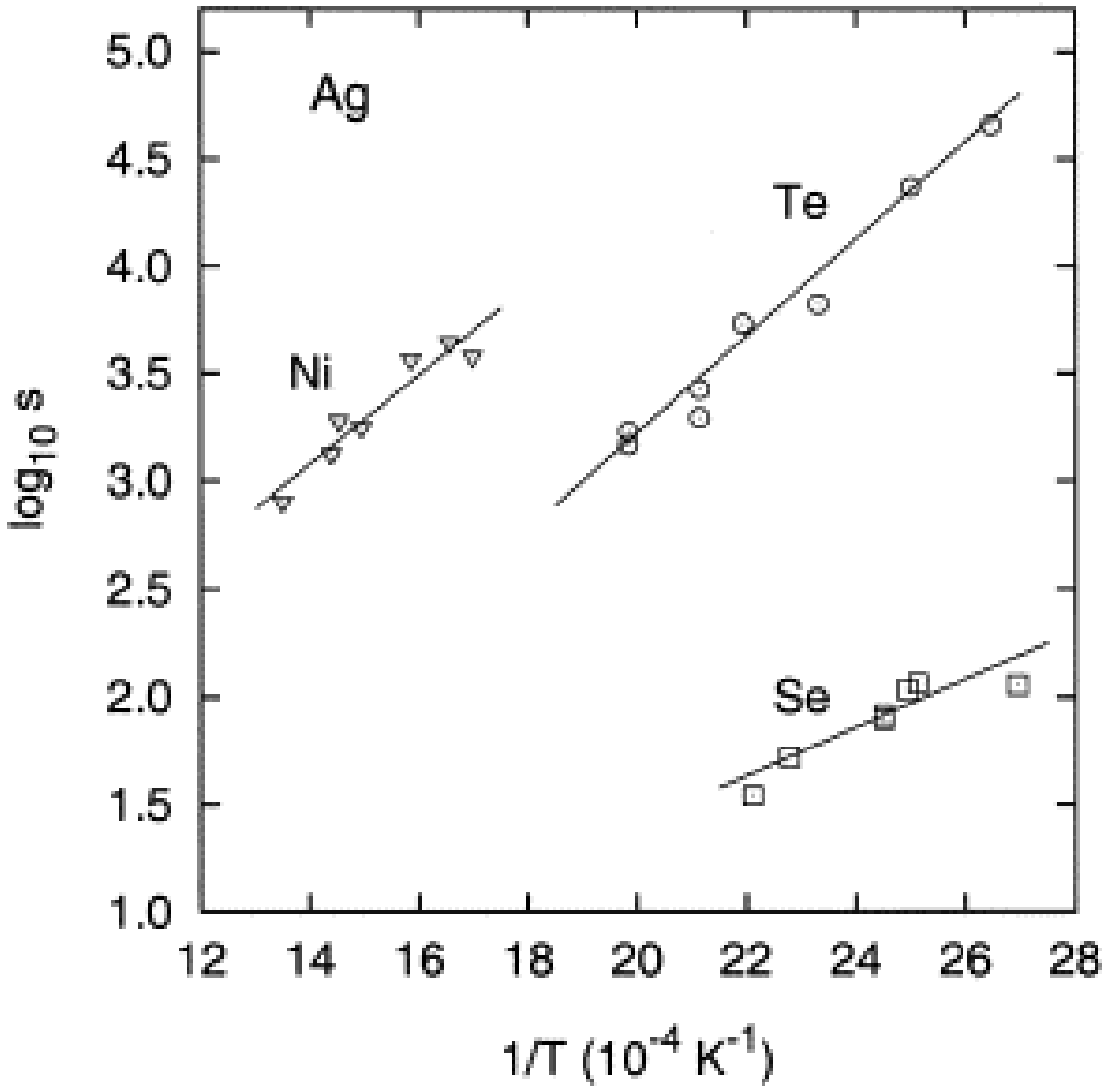

Figure 2.7: Arrhenius diagram of the segregation factor for impurity diffusion in Ag [53]

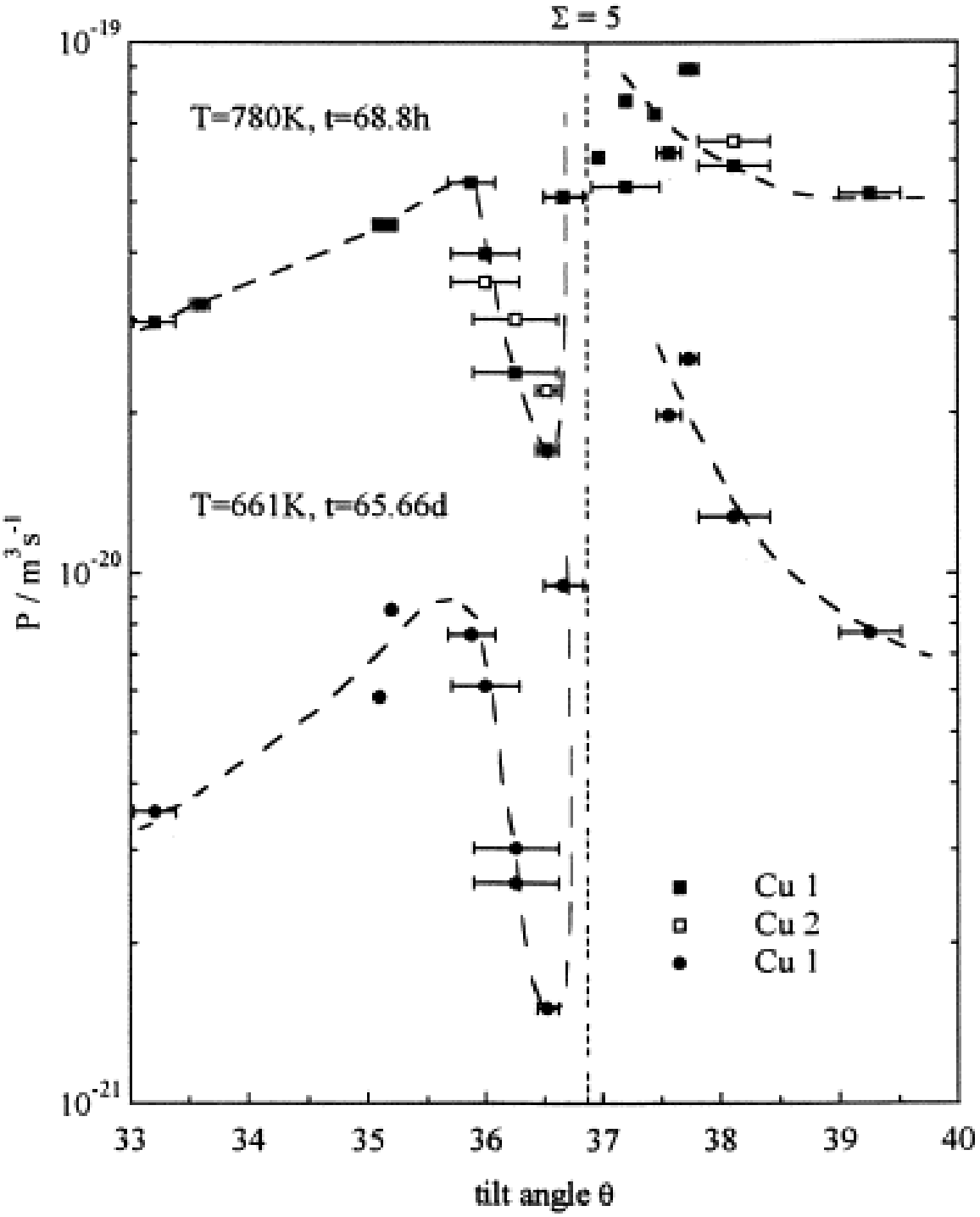

Figure 2.8: Orientation dependence of the diffusivity ($P = s\delta D_{GB}$) of gold in copper [001] tilt symmetric grain boundaries for two different purities of copper: Cu1 and Cu2 at two different diffusion lengths. [58].

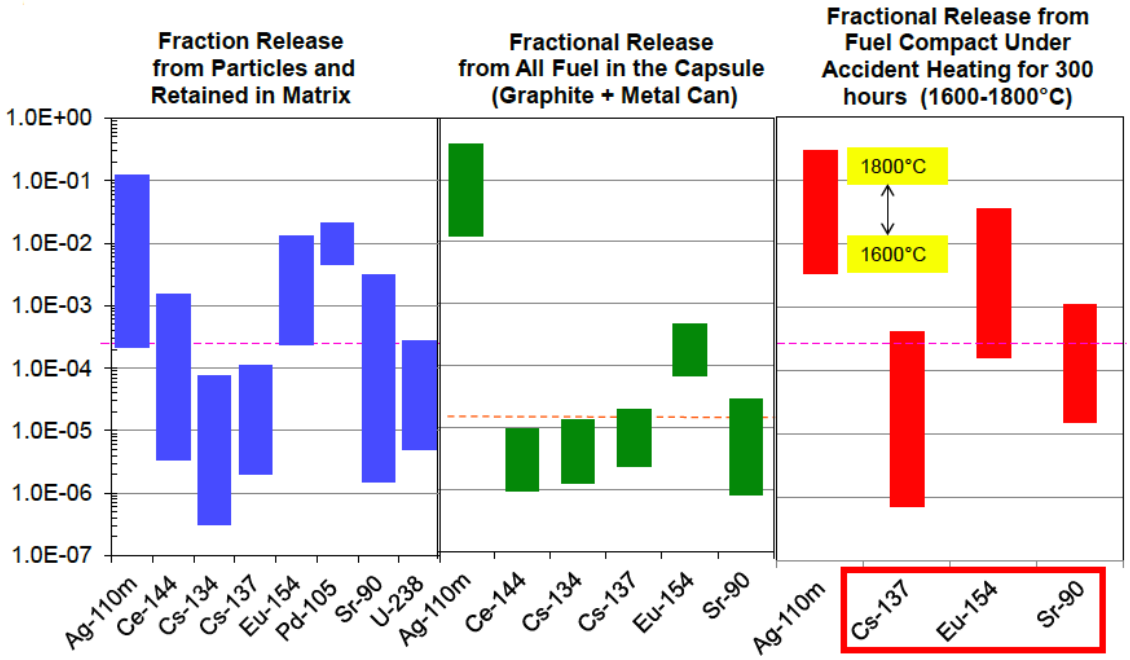

Figure 2.9: Fractional fission product release from the AGR-1 lab-scale fuel irradiation at the advanced test reactor at Idaho National Laboratoy (INL) [3].

CHAPTER III

Experimental Method

3.1 Materials

Polycrystalline SiC was chosen as the substrate material to be as representative of TRISO SiC as possible. The SiC substrates were supplied by Rohm and Haas Chemicals LLC in the form of 1 cm $\times$ 1 cm $\times$ 0.6 mm plates made by grinding and cutting a larger plate grown by CVD with the growth direction normal to the surface. X-ray diffraction (XRD) analysis was conducted using a Rigaku X-ray diffractometer with Cu Kα radiation from 30° to 110° with a step size of 0.01° to identify if any phases other than β-SiC were present. The XRD spectrum, shown in Figure 3.3 contains peaks that match only with β-SiC. There is also a broad plateau near the (111) peak that is characteristic of stacking faults in SiC which was verified in TEM [74].

Previous electron back scatter diffraction (EBSD) analysis presented in Figure 3.1 showed large and small columnar grains in the growth direction with an average grain size of 1.5μm with grains as large as 14μ [74]. The microstructure of TRISO SiC depends on the deposition conditions which have been varied over the past 60 years to reduce the dominant fuel failure mode of that test campaign. Figure 3.2 presents inverse pole maps of the four different variants of SiC used in the AGR-1 TRISO fuel irradiation campaign [75]. In all four variants, large grains tend to be columnar in the growth direction, while small grains are equiaxed. The grain size ranges from

$2\mu m$ for variant 1, to 600 nm for variant 4. Variant 1 is the most similar variant to the SiC used here with grains ranging in size from 500 nm to $8\mu m$, with an average grain size of 2 μm. Grain boundary character determination (GBCD) of TRISO SiC showed a microstructure dominated by random high angle boundaries and a lack of low-Σ grain boundaries as is the case in the material used here [76].

3.2 Diffusion Couple Fabrication

The fabrication of the diffusion couple is divided into 4 steps, as shown schematically in Figure 3.4 : substrate preparation, PyC deposition, FP implantation, and SiC cap deposition. Proper substrate preparation resulted in a sharp substrate/host layer interface to accurately measure the diffusion depth of FPs into the SiC. The PyC host layer was deposited via CVD in order to be chemically similar to TRISO PyC. FP implantation into the PyC introduced the FP and provided the capability to investigate a wide range of elements. A final SiC diffusion barrier layer was deposited using plasma enhanced CVD (PECVD) to prevent premature loss of the FPs during annealing.

3.2.1 Substrate Preparation

The substrates were ground flat using 9μm diamond solution and polished using 3 μm, 1μm and 0.25 μm diamond solutions for 5 minutes per step prior to a vibratory polish using 0.02 μm colloidal silica for 4 hours. Surface roughness, measured using an atomic force microscope (AFM) sampling 8,000μm^2 was 22 nm R_a. While the chemo-mechanical polishing (CMP) mechanism of the vibratory polish removes the damage layer introduced by conventional mechanical polishing, it also introduces a surface contamination layer [77]. A final plasma cleaning, using a 500 W argon plasma at 130 mTorr for 5 minutes, removed this layer and improved the surface finish by reducing the surface roughness to 6 nm R_a.

3.2.2 PyC Deposition

Figures 3.8a-3.8c shows simulations of the implanted concentration profile and displacement damage introduced into PyC at 400 keV to a fluence of 10^{16} cm^{-2}. The PyC thickness was standardized to 300 nm for all the elements investigated to ensure that similar concentrations were achieved. PyC depositions were performed in a vertical flow hot-walled graphite reactor at $1,300$°C and 15 Torr. A schematic of the furnace is shown in Figure 3.5. The reactant enters the hot-zone from the top allowing for a large uniform deposition area within the furnace. A sight glass is used to ensure the temperature is accurate using a pyrometer calibrated to the emissivity of the graphite insulation on which the samples sit on. A vacuum connection on the bottom allows for evacuation prior to heat up and ensures that the reactant is flowing vertically within the reaction zone to ensure uniform coatings. A schematic of the gas mixing system is shown in Figure 3.6, which allows for variable mixtures of ultra-high purity (UHP) argon and propylene using two mass flow controllers. The system can divert the flow to either the top port for PyC depositions or to the sight glass for thermal annealing treatments using two 3-way ball valves. A vent port equipped with a wide range diaphragm manometer allows for pressure monitoring from 1,500 Torr down to 1 mTorr.

Prior to deposition of PyC, the samples were cleaned in baths of acetone, methanol, and finally ethanol in a sonicator for 5 minutes each. They were then dried using a 99.99% nitrogen line before being loaded into the furnace equidistant from each other and the edges of the graphite insulation. The furnace was then sealed and evacuated to 50 mTorr using a two-stage oil-sealed rotary vane pump. The furnace pressure is then raised to 15 Torr by flowing 50 sccm of UHP argon. A throttle valve was used to control pumping speed to stabilize this pressure. The furnace was then heated to $1,300$°C over a 1-hour period. The temperature was verified using a spot pyrometer measured on the graphite support on which the samples rest. After allowing the

temperature to settle to within 5°C of the 1,300°C set point, 21.6 sccm of 99.5% purity propylene was introduced via another mass flow controller and the deposition proceeded for a total of 35 minutes. When the deposition was complete, the propylene flow was cut off, and the reactor was cooled down over 4 hours to prevent thermally shocking the deposited PyC.

Coating thicknesses were measured using Rutherford backscattering spectrometry (RBS) performed at the Michigan Ion Beam Laboratory (MIBL). A 1 mm diameter 2 MeV He^{++} beam was placed on the sample at normal incidence to the sample surface with a detector at a backscatter angle of 160°. Figure 3.7 shows a RBS spectrum for a 308 nm PyC deposition on a SiC substrate. The green arrow marks the front surface energy for the PyC, while blue arrows mark the width of the carbon plateau from the PyC and the silicon edge from the SiC. The PyC thickness was calculated by simultaneously fitting the width of the carbon plateau and the shift down in energy of the silicon edge due to the PyC, assuming the PyC was at the theoretical density of 2.21 g/cm^3. This yielded a thickness of 306 ± 10 nm as measured over 5 batches of 10 samples. The sample roughness, as measured over 8,000μm^2 using AFM, increased to 11 nm R_a after PyC deposition.

3.2.3 Fission Product Implantation

FP implantation was performed at the Michigan Ion Beam Laboratory (MIBL) using a National Electrostatics Ion Implanter. All of the investigated FPs: cesium, europium and strontium were implanted at 400 keV to a fluence of $10^{16} cm^{-2}$. The implantation energy was chosen to maximize the implanter efficiency, while the fluence was chosen to be in the order of magnitude of the FP yield per unit IPyC/SiC interface area for a TRISO particle at 20% burn up [78]. The implantation flux was limited to $1.5 \times 10^{11} cm^{-2} s^{-1}$ to maintain the sample at room temperature as measured by a thermocouple located behind a sample. The resulting FP concentration profile, was

measured using RBS and was found to be Gaussian in shape and contained within the PyC. Implantation peak depths ranged from 60 nm for europium to 160 nm for strontium. Peak concentrations ranged from 1.9% to 0.95%. Full width half-maxima (FWHM) ranged from 53 nm to 88 nm. Figure 3.8 shows the implantation and damage profiles, as calculated by SRIM in the quick Kinchin-Pease mode, using a carbon displacement energy of 24 eV [79] for 400 keV cesium, europium and strontium into PyC to a fluence of $10^{16} cm^{-2}$. Table 3.1 lists the FP implant energy, range, full width half maximum (FWHM) and peak concentration. The high fluence induces a large amount of radiation damage in the PyC. Most of the implanted FP is within the expected amorphous region, which occurs over 1 dpa [80], while a small portion of the PyC near the substrate is left undamaged.

3.2.4 SiC Cap Deposition

It was found early on that FPs easily migrate through the front surface and out the sides of the PyC layer at annealing temperatures of $1,100°C$ to $1,600°C$, well over their respective melting points. Several coatings were tested for their efficacy in retaining fission products within the diffusion couple. Physical vapor depositions of molybdenum and tungsten delaminated from the PyC at 900°C. Sputter depositions of SiC proved to be ineffective, allowing all of the implanted FP to be released from the diffusion couple after annealing at $1,100°C$ for 10 hours. It was postulated that the FP was diffusing out the edges of the PyC coating. SiC coatings created by pyrolyzing spin-coated polycarbosilane (PCS), which covered the edges of the diffusion couple as well as the front surface, showed promise in retaining both silver and cesium at $1,100°C$. The coatings were difficult to reproduce, exhibited a high degree of non-uniformity and greatly enhanced the roughness of the diffusion couple.

PECVD SiC was found to create a reproducible, high density, low roughness coating and so it was chosen as the diffusion barrier to retain FPs within the PyC and

thus, allow for diffusion into the SiC substrate. This process creates a reproducible, high density, low roughness coating. The thickness of this cap was limited to a maximum of 100 nm in order to retain the ability to accurately measure FP concentration profiles in the PyC via RBS. Initial tests showed that a 50 nm thick layer was sufficient to retain FPs within the diffusion couple. The PECVD SiC was deposited using a Plasmatherm 790 PECVD tool. The chamber was evacuated using a two-stage turbo-drag pump backed by a semiconductor pump to a pressure of 10^{-8} torr before being heated to 250°C. Then, 1,000 sccm of argon was flown into the chamber for 2 minutes to allow the throttle valve to stabilize the chamber pressure at 1 Torr before flowing 50 sccm of methane and 5 sccm of silane. The plasma was powered by a 13.56 MHz RF generator, which provides 0.05 W cm^{-2} for 5 minutes. The chamber was then re-evacuated to 10^{-8} torr and cooled before removing the diffusion couples.

Figure 3.9 shows the RBS spectrum for a strontium diffusion couple after being coated with the PECVD SiC. Green arrows mark front surface energies. The peak closest to the strontium surface energy is from the strontium implantation into the PyC. The PECVD cap primarily shows up as the silicon peak at the 1143 keV. There is also an oxygen peak and nitrogen peak that are contaminants in the PECVD SiC due to contaminants in the argon. The silicon to carbon ratio was measured from the ratio of the silicon peak to the height of the step in the carbon edge that marks the transition from PECVD SiC to PyC. The silicon:carbon ratio ranged between 1.0 and 1.2. The sample roughness did not change from 22 nm R_a measured post-implantation as a result of the PECVD deposition. A cross-section sample of the PECVD SiC cap on PyC was prepared for transmission electron microscopy (TEM) using the focus ion beam (FIB) technique. A diffraction analysis of the SiC cap revealed that it was amorphous, as expected of the low temperature process. The density, calculated from the areal density measured by RBS and the thickness measured in TEM, yielded a value of 2.64 g/cm^{-3} or 83% of the theoretical density of SiC.

Leakage of FPs through the cap was observed in all samples with diffusion couples retaining larger total quantities of the implanted FP at lower temperatures. Total cesium leakage ranged from 0% at 900°C to 15% at 1,300°C, while total strontium and europium leakage ranged from 8% at 900°C to 92% at 1,300°C. Ion irradiated diffusion couples exhibited the same amount of leakage as their thermally annealed counterpart. Higher temperature anneals increased the likelihood of SiC cap loss and in combination with the FP leakage through the cap limited this study to 1,300°C. ‘

3.3 High Temperature Annealing

All thermal annealing treatments were performed in a high temperature graphite furnace with a custom gas delivery system that allows for PyC deposition or ultra clean annealing. Ultra high purity (UHP) (99.995%) argon was passed through an inert gas purifier to prevent oxygen contamination and is admitted to the furnace via a mass flow controller with an upstream solenoid to allow for vacuum operation. An oil-based rotary vane rough pump is used to create a temporary vacuum and to allow for flushing and backfilling at the beginning of operation. Vacuum is measured using a wide range diaphragm manometer that is sensitive down to 1 mTorr. Argon is introduced through the top port during the furnace flushing operation or a side quartz window port during high temperature annealing. A calibrated boron-graphite thermocouple provides feedback for power control. The calibration is performed at 900°C, 1,100°C, 1,300°C, and 1,500°C using a Type C thermocouple that can be inserted through a top feed-through. A graphite crucible with a cavity positioned at the sight-line of the quartz window is also calibrated for emissivity for use with a pyrometer. During operation the temperature control is from the boron graphite thermocouple, but is validated using the pyrometer. A calibration is performed after every 4 annealing treatments or 2 weeks to ensure the accuracy of the furnace temperature remained at 1% of the measured temperature.

Diffusion couples were cleaned in a sonic cleaner filled with ethanol to remove any surface contaminants and then loaded into a graphite crucible in the furnace. The furnace was then evacuated to 100 mTorr and back-filled with argon once to flush the argon lines and inert gas purifier, followed by a second evacuation to 100 mTorr. Power was slowly applied and the furnace was heated to 400°C in 30 minutes and then held at this temperature in order to remove water and nitrogen contaminants in the graphite felt insulation. Once the vacuum returned to 100 mTorr, ultra high purity argon was admitted to establish a pressure of 10 Torr within the furnace and held for 15 minutes to continue to flush contaminants. The vacuum pump is then isolated and the furnace is pressurized to 800 Torr to ensure that air could not leak into the furnace. The furnace is then ramped to operating temperature at ramp rates of 200°C/hr up to 900°C, and then 100°C/hr up to 1,300°C. The furnace temperature is verified at the beginning of the dwell and at the end via the calibrated pyrometer and cavity. Ramp down rates are 100°C/hr above 900°C and 200°C/hr below 900°C. Five annealing conditions were used in this study: 900°C 40 hours, 1,066°C 10 hours, 1,100°C 10 hours, 1,200°C 10 hours, and 1,300°C 10 hours. The 1,100°C 10 hour condition was repeated for strontium to test the repeatability of the results.

3.4 Ion Irradiation

High temperature irradiations were performed using a 3 MV Pelletron accelerator at the University of Michigan Ion Beam Laboratory. Figure 3.10 is a schematic of the irradiation chamber that was designed to allow for accurate dose and temperature monitoring. A 4.5 MeV Si^{++} beam is raster scanned at 1,019 Hz horizontally and 117 Hz vertically over a set of tantalum slits that define the irradiation area. Dose is monitored using a Faraday cup inserted periodically in front of the stage to measure the beam current on the stage. Vacuum at the start of an irradiation was in the 10^{-8} Torr range, but jumped into the mid 10^{-7} range when beam is first applied and

slowly dropped during the course of the irradiation.

The calculated dose-rate was $4.6 \times 10^{-3} dpa\ s^{-1}$ at the PyC/SiC substrate interface in the SiC using SRIM in quick Kinchin-Pease mode [81, 82] with a silicon atom displacement energy of 35 eV and a carbon atom displacement energy of 20 eV [13]. This damage rate was necessary to achieve the peak irradiation temperature of $1,100°$C. The irradiations were all conducted for 6 hours to a final dose of 10 dpa. Figure 3.13 shows the total damage and implanted ion concentration as a function of depth. Between the PyC/SiC substrate interface (at a depth of 350nm) and a depth of 1,000 nm the implanted silicon concentration was minimal and the change in dose only varies by a factor of two. While this could affect the diffusion kinetics, the majority of the effect should be within the first 300 nm as witnessed in the thermal diffusion study, where the dose only varies by a factor of 50%.

Ion irradiation is used as a simulant for neutron radiation damage in this study. These two methods of creating radiation damage can differ in the dose-rate as well as the damage morphology. The dose-rate can be experimentally controlled, but the damage morphology is feature of the irradiation type. The spectrum of primary knock-on atom (PKA) energies is determined by the interaction of the irradiating particle and the material. Once the PKA is created, the damage process is independent of the irradiation type. Thus comparing PKA energy spectra is a useful method to compare the damage morphology between neutron irradiation and ion irradiation. The weighted average recoil spectrum is the PKA energy spectrum weighting for the total number of displacements made by that energy PKA [83]. It is defined as:

$$W(E_i, T) = \frac{1}{E_D(E_i)} \int_{E_d}^{T} \sigma(E_i, T') E_D(T') dT' \tag{3.1}$$

$$E_D(E_i) = \int_{E_d}^{\hat{T}} \sigma(E_i, T') E_D(T') dT' \tag{3.2}$$

T is the PKA energy. $\sigma(E_i, T')$ is the energy transfer cross section for an incoming particle of energy E_i to a PKA of recoil energy T'. $E_D(T')$ is the damage energy, which is the energy loss by the incoming particle to PKAs. E_d is the displacement energy, which is 20 eV for carbon and 35 eV for silicon [41]. $\hat{T}$ is the maximum energy transfer to a PKA:

$$\hat{T} = \frac{4M_1M_2}{(M_1 + M_2)^2} E_i \tag{3.3}$$

M_1 is the incoming particle mass and M_2 is the PKA mass, which will depend on whether the incoming particle interacts with the silicon or carbon sub-lattice. There is an analytic solution for the weighted average recoil spectrum for neutron irradiation [83]:

$$W_n(E_i, T) = \frac{T^2 - E_d^2}{\hat{T}^2} \tag{3.4}$$

For the silicon ion irradiation, there is no analytic solution. The Lindhard model [84] was used for both the energy transfer cross-section and the damage energy, as detailed in ref [83], to calculate the weighted recoil spectrum for the ion irradiation.

Figure 3.14 presents the weighted recoil spectra for 4.5 MeV Si^{++} ions using the Lindhard model and 1 MeV neutrons using the analytic solution from Eq. 3.4. The average energy for carbon primary knock on atoms (PKA) in the silicon ion irradiation is 92 keV for the carbon lattice vs. 238 keV for the neutron irradiation. The average energy for silicon PKAs in the silicon ion irradiation is 64 keV vs. 98 keV in the neutron irradiation. This indicates that the damage morphology will be more comparable between the neutron and silicon ion irradiations on the silicon sub-lattice vs. carbon sub-lattice. For both irradiation types the majority of damage is created by PKAs exhibiting the average PKA energy. The tails of the ion irradiation PKA energy spectrum are much more pronounced indicating that cascade morphology will vary more for the ion irradiation than the neutron irradiation which exhibits a narrow range of PKA energies.

3.4.1 Stage Design

The irradiation stage was designed to be able to conduct ion irradiations at high temperatures and is shown in Figure 3.11. This was accomplished by using a high power density pyrolytic boron-nitride(PBN)/graphite heater designed to operate up to $1,500°C$ and insulating the stage from the vacuum flange with a vacuum break. The stage consists of two 1/16" molybdenum plates supported by four stainless steel posts connected to the vacuum flange and separated by a 4-40 stainless steel nut to provide the vacuum break. The PBN heater is mounted on the molybdenum plates by molybdenum threaded rods and nuts. A set of alumina screws is mounted in the top molybdenum plate above and below the heater. These allow the graphite shim to be repeatedly placed on the same position on the heater and to provide the clamping force to hold the sample to the heater. One feed-through provides the power for the PBN heater while the other provides thermocouple connections.

The stage is assembled by first mounting both molybdenum plates in place followed by the heater. The connections to the heater are installed and tested to ensure that the total resistance across the power pins is 8Ω. The guide screws for the graphite shim are then installed in place and the stage is ready for sample mounting. The sample is cleaned in a sonicator with ethanol to remove any surface contaminants. The sample is then placed on the PBN heater and the graphite shim is lined up on the guide posts. The thermocouple is placed on the edge of the sample and held in place while the graphite shim is slid into place. Alumina nuts are then used to tighten down the graphite shim. Light hand tightening, followed by 1/2 turn per nut with a pair of tweezers is sufficient to ensure even contact between the graphite shim and the sample. The stage is then connected to a power source for the heater and the thermocouple is tested to ensure it is reading and responding to temperature changes.

3.4.2 Temperature Monitoring

The sample temperature was monitored using a thermocouple and a 2D infrared pyrometer. After initial heating to 250°C, the 2D infrared pyrometer was calibrated to the surface emissivity using the thermocouple. A total of 9 areas of interest were placed in a 3×3 pattern on the front surface of the sample as shown in Figure 3.12. The emissivity of each area of interest is then adjusted until the temperature is in line with the thermocouple reading. This is performed every 200°C, up to the peak sample temperature of 900°C when the beam is not applied. The ion beam adds an additional 200°C of temperature increase due to beam-heating as verified using the pyrometer. The thermocouple is protected from the beam and does not see this temperature increase. The surface temperature varied by 15°C across the irradiated area.

A COMSOL thermal analysis was performed to ensure that the surface temperature was indicative of the SiC substrate and that the temperature profile in the SiC substrate could be considered constant. A thermal conductivity of 0.1 W/(m°K) [85] was used for the SiC cap and 4 W/(m°K) [86] for the PyC. A temperature dependent thermal conductivity was used for the SiC substrate [13]:

$$K_P = \left[-0.0003 + 1.05 \times 10^{-5} T\right] \tag{3.5}$$

The back temperature of the sample was calculated at $1,280$°C for a front surface temperature of 900°C considering only the heat generation from the heater. This served as the back surface boundary condition for the ion irradiation condition where the ionization energy deposited by the 4.5 MeV silicon ion was used as the heat generation term. Figure 3.15 shows the resultant temperature distribution considering radiative heat transport from the front surface and conduction throughout the layer with perfect contact at the interfaces for an $1,100$°C silicon ion irradiation. The

temperature drop from the front surface within the first $2\mu m$ is less then 0.01°C, which is significantly less than any other source of error in the temperature measurement. This validates the use of the surface temperature as the diffusion temperature in all RED analyses.

3.5 Diffusion Profiling and Calculation

3.5.1 ToF-SIMS

Time of flight secondary ion mass spectrometry (ToF-SIMS) was used to profile the diffusion of FPs into the SiC. Two separate Ion-TOF SIMS 5 instruments were used at Pacific Northwest National Labs (PNNL) and Georgia Institute for Electronics Tech and Nanotechnology (IEN). All ToF-SIMS spectra were acquired analyzing for positive ions using 25 keV Bi^+ to sputter material for analysis and 5 keV O^+ to sputter material for depth profiling. The sputtered craters were $100\mu m \times 100\mu m$ while only the center $50\mu m \times 50\mu m$ was analyzed to prevent edge effects that would reduce the depth resolution of the analysis.

Figure 3.16 shows an optical image of one sputter crater and optical profilometry line scans across the crater bottom. The line scans have been adjusted to show the deviation from the crater bottom. The deviation is within 10 nm for most of the central 50 μm area, which is the area analyzed in the ToF-SIMS measurement. Surface roughness in the analysis area is 7 nm R_a, which is comparable to the surface rougness of the diffusion couple, indicating that the sputtering process has not introduced an added source of error in to the SIMS profiles.

SiC substrates, ion implanted with cesium, strontium, or europium at 400 keV to a fluence of 10^{16}cm^{-2}, were used as calibration standards for the depth profiles. Depth profiles of these samples with the same instrument parameters as the profiles were used to calculate sputter rates and reduced sensitivity factors (RSF). These

calibrations were measured at the beginning of each SIMS session. The sputter rate was calculated from the crater depth assuming a constant sputter rate through the calibration profile at 0.66 nm/s at PNNL and 0.53 nm/s at the IEN. The RSFs are calculated by:

$$RSF = \frac{DnI_{matrix}t}{zI} \tag{3.6}$$

where D is the implanted dose in cm^{-2}, n is the number of data points,I_{matrix} is the average matrix counts, t is the time between data points, z is the depth of the crater in cm, and I is the sum of the counts from the element of interest along the full depth range of the implant. The RSFs were 5,400 for cesium, 7,100 ppm for strontium, and 8,900 ppm for europium. The RSFs varied by no more then 4% between instruments. The concentration (C) and depth (x) are then calculated by:

$$\begin{aligned} x &= \dot{Y} \times t_{sputter} \\ C &= RSF \times \frac{I_{FP}}{I_{matrix}} \end{aligned} \tag{3.7}$$

where $\dot{Y}$ is the sputter rate, I_{FP} is the count rate for the calibrated element and I_{matrix} is the count rate for the matrix element.

3.5.2 Diffusion Calculation

FP diffusion in the SiC should proceed via two different mechanisms: bulk or grain boundary diffusion. The Fisher model was used to analyze the various diffusion regimes and is illustrated in Figure 2.4 [46, 47]. The first regime, Type A, occurs at very high temperature or long diffusion times and bulk diffusion dominates the overall FP flux. This results in a Fickian concentration profile that can be analyzed

with the simple 1D steady state constant source solution:

$$C_B(x) = C_0 erfc\left(\frac{(x - x_0)}{\sqrt{4D_B t}}\right) \tag{3.8}$$

or the thin film solution:

$$C_B(x) = C_0 exp\left(\frac{(x - x_0)^2}{4D_B t}\right) \tag{3.9}$$

depending on the surface concentration conditions.

The Type C regime occurs at very low temperature or short diffusion times where only grain boundary diffusion is relevant, as bulk diffusion is too low to measure. The grain boundary concentration profile follows a standard Fickian diffusion profile and is fit using the same formalism as bulk diffusion in the bulk diffusion dominant regime.

The Type B diffusion regime occurs at intermediate temperatures and diffusion times where both bulk and grain boundary diffusion are significant for the overall FP flux. In this mixed diffusion regime, the bulk diffusion concentration profile still follows the same Fickian analysis since the source is still dominated by the interface concentration C_0. There is also a grain boundary diffusion tail tail which has a source term composed of the interface concentration and the whole bulk diffusion front and requires a complicated analysis to calculate a diffusion coefficient. Traditionally this is done by plotting the $ln(C)$ vs $x^{6/5}$ and fitting a line through the tail region [87,88]. For this analysis, the tail region was directly fit to an exponential:

$$C_{GB}(x) = C_0^{GB} exp(-m * x^{6/5}) \tag{3.10}$$

where m is defined as:

$$m = \frac{\partial ln(C)}{\partial x^{6/5}} \tag{3.11}$$

The grain boundary diffusion coefficient was then calculated from [48]:

$$s\delta D_{GB} = 2\sqrt{\frac{D_B}{t}}\left(0.77 + \frac{\delta}{\sqrt{8D_B t}}\right)^{5/3} m^{-5/3} \tag{3.12}$$

where s and δ are two parameters that are difficult to determine unless the grain boundary dominant region can be accessed. For self-diffusion $s = 1$, but for over-sized solute diffusion s can vary greatly [48]. The grain boundary width (δ) on the other hand has been found to range between $0.5nm$ and $2nm$ for both self-diffusion and solute diffusion [48].

These formalisms are only valid in the regions of the diffusion profile where bulk diffusion is strongly dominant or where grain boundary diffusion is strongly dominant. Between these two regions the concentration profiles are dictated by the whole Whipple solution and not just the super-position of these two analytic simplifications due to the interaction of the bulk diffusion and grain boundary diffusion mechanisms [48].

3.5.3 Error Analysis

A scientific computing and analysis package, SciPy [89], was used to fit exponentials for both bulk and grain boundary diffusion rather than apply linear fits in a transformed space. Directly fitting the error function and exponential allows the fit code to calculate the covariance of the fitting variables, which for the bulk diffusion coefficient is the error. The analysis package uses least-squares non-linear regression which minimizes the sum of the squares of the residuals to find the best fit:

$$\chi^2 = \sum_{i=1}^{N} \frac{1}{\sigma_i^2}\left(y_i - y(x_i, \beta)\right)^2 \tag{3.13}$$

where N is the number of data points, y_i is the data point, σ_i is the error in that data point, and β_m is the m-th iteration of the coefficient matrix for the model

equation defined by $y(x, \beta)$. SciPy performs this minimization and returns the best fit parameters and a covariance matrix: $\mathbf{C}$. The diagonal elements of this covariance matrix are the variances of the fitted parameters. For the case of fitting bulk or grain boundary diffusion using Eq. 3.9, this is the error in the diffusion coefficient:

$$[\sigma_{C_0}, \sigma_{D_B}] = diag(\mathbf{C}) \tag{3.14}$$

One estimate of goodness of fit for non-linear regression is the Pearson χ^2:

$$\chi^2_P = \sum_{i=1}^{N} \frac{(y_i - y(x_i, \beta_m))^2}{y(x_i, \beta_m)} \tag{3.15}$$

The cumulative χ^2 is then used to look up the p-value, which is the probability that the fit accurately models the data given the number of degrees of freedom available to the fitting equation. A χ^2_P of 0 would indicate that the fit perfectly represents the data, while a χ^2_P of ∞ indicates that the model and data share no relation.

If two mechanisms are active, the grain boundary diffusion coefficient is fit from a diffusion tail using Eq. 3.10 and calculated using Eq. 3.12. In this case the error in the grain boundary diffusion coefficient is calculated using the variance formula:

$$\sigma_{D_{GB}} = \sqrt{\left(\frac{\partial D_{GB}}{\partial D_B}\right)^2 \sigma^2_{D_B} + \left(\frac{\partial D_{GB}}{\partial m}\right)^2 \sigma^2_m} \tag{3.16}$$

$$\begin{aligned}\frac{\partial D_{GB}}{\partial D_B} =& \frac{1}{s\delta}\left[\sqrt{\frac{1}{D_B t}}\left(0.77 + \frac{\delta}{\sqrt{8D_b t}}\right)^{5/3} m^{-5/3}\right. \\ &\left. + \frac{-5}{6}\left(0.77 + \frac{\delta}{\sqrt{8D_B t}}\right)\left(\frac{\delta}{\sqrt{8t}} D_B^{-3/2}\right)\right]\end{aligned} \tag{3.17}$$

$$\frac{\partial D_{GB}}{\partial m} = \frac{2}{s\delta}\sqrt{\frac{D_B}{t}}\left(0.77 + \frac{\delta}{\sqrt{8D_b t}}\right)^{5/3} \frac{-5}{3} m^{-8/3} \tag{3.18}$$

This yields the true error in the grain boundary diffusion coefficient due to errors

in both the fit and the bulk diffusion coefficient. The relative error, defined as the percent of the total error from the fit, gives an indication of how well the grain boundary tail is fit in comparison with the bulk fit. A low relative error indicates that the grain boundary diffusion coefficient error is systemic of the experiment itself, rather than from the ability to discern and fit the tail.

The process of fitting the two regimes can be somewhat subjective. A metric based methodology reduces this subjectivity and makes the process repeatable. Figures 3.17 shows a flow chart for this process. The concentration profile is visually examined to determine if there is one active mechanism or two. Figures 2.4a and 2.4c both diagram the concentration vs depth profile for a single active mechanism, while Figure 2.4b diagrams the concentration vs depth profile for two active mechanisms. Two active mechanisms indicated that the diffusion kinetics are in the mixed diffusion regime. In this case bulk diffusion was fit first. The fitting program successively increased the fit area starting from the interface using Eq. 3.9. Once all possible fits from the interface were found, the bulk diffusion coefficient was calculated from the fit that minimized the relative fitting error, defined as the standard deviation of the fit over the fit value. The process was repeated for the grain boundary concentration tail using Eq. 3.11 starting at the end of the tail and successively increasing the fit area back towards the bulk diffusion portion. The grain boundary diffusion coefficient was then calculated using Eq. 3.12. If the concentration profile did not exhibit mixed kinetics the single mechanism was fit using Eq. 3.9 to obtain a diffusion coefficient. Comparing the temperature of the annealing or ion irradiation with the temperature range for mixed kinetics indicated if the concentration profile was due to bulk or grain boundary diffusion.

3.6 Transmission electron microscopy

Transmission electron microscopy (TEM) samples were prepared via the focused ion beam (FIB) lift out method using a FEI Helios with a final thinning performed using 5 kV Ga^+ ions at the Michigan Center for Materials Characterization. Scanning transmission electron microscopy (STEM) analysis was performed at Sandia National Labs on the sample containing strontium and thermally treated at $1,100°C$ for 10 hours using a FEI Titan G2 80-200 with ChemiSTEM technology operated at 200kV. Bright field diffraction contrast images were used to identify grain boundaries in the SiC substrate. High angle annular dark field images were used to identify areas of build up of strontium along the PyC/SiC interface. Bulk and grain boundary diffusion were profiled using energy dispersive spectrometry (EDS) with a collection solid angle of 0.7 sr. X-ray images were acquired in STEM mode using a sub-nm probe at a current of 2 nA.

Fission Product	Energy (keV)	Range (nm)	FWHM (nm)	Peak Concentration (%)
Cesium	400	144 (140)	63 (65)	1.38 (1.37)
Europium	400	118 (115)	45 (48)	1.84 (1.82)
Strontium	400	184 (178)	88 (90)	0.96 (0.95)

Table 3.1: FP Implantation range, FWHM, and peak concentration for cesium, europium and strontium in PyC as calculated by SRIM 2013. RBS measured values are in parenthesis.

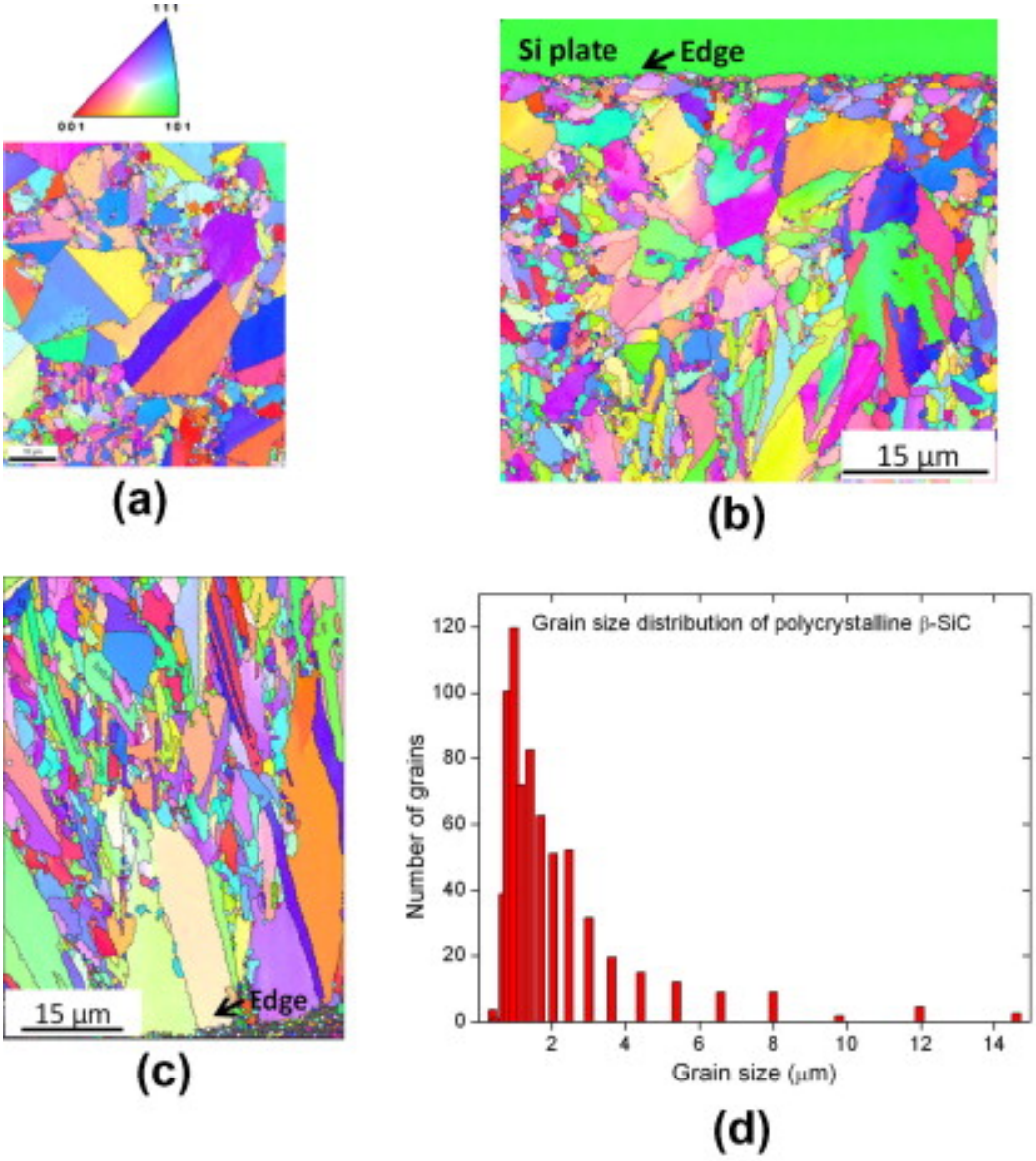

Figure 3.1: Electron back scatter diffraction (EBSD) of the Rohm and Hass SiC used in this study. (a) Inverse pole figure in the growth direction (b and c) normal to the growth direction (d) grain size distribution [74]

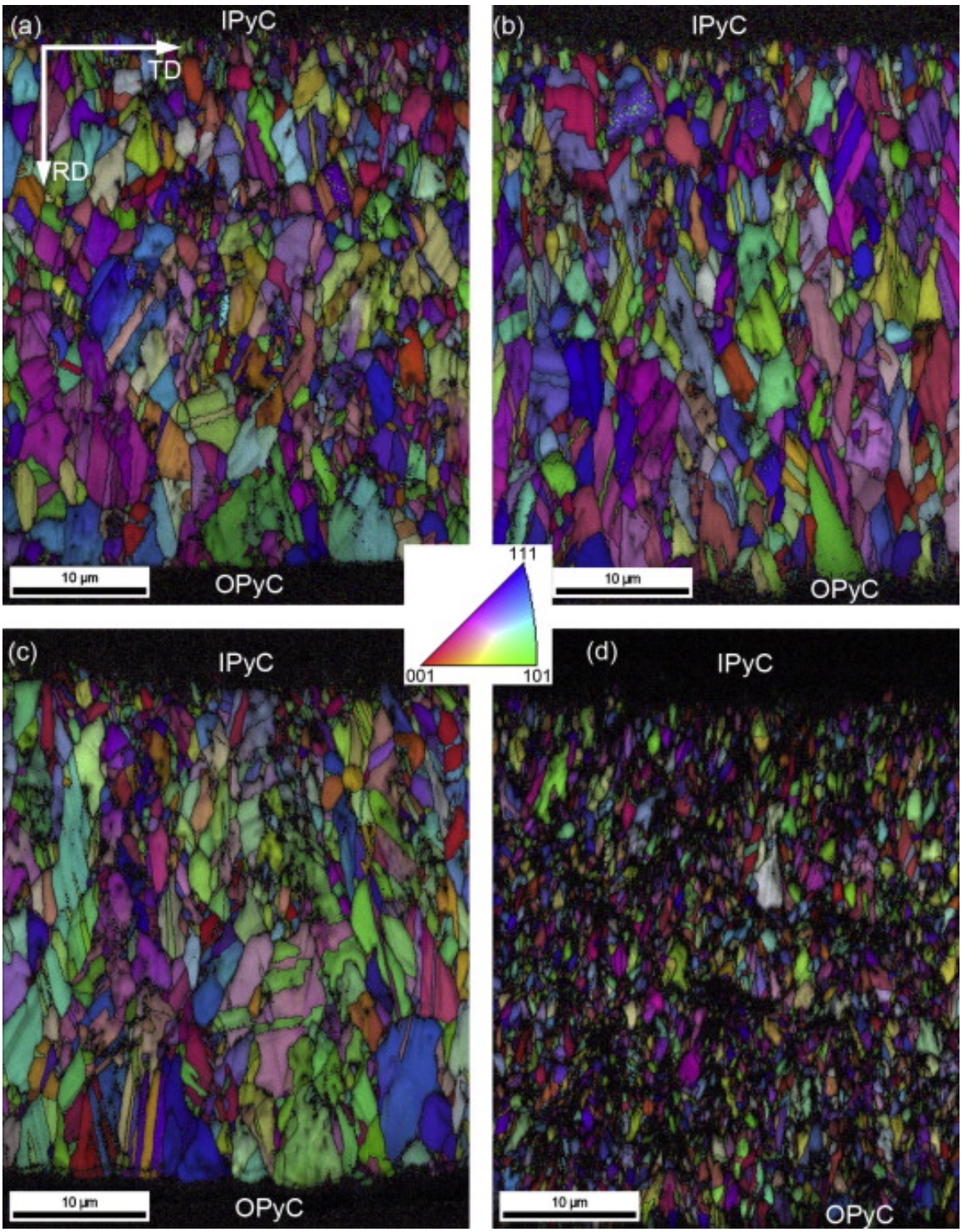

Figure 3.2: EBSD inverse pole maps of the four different variants of SiC used in the AGR-1 TRISO Fuel irradiation campaign [75].

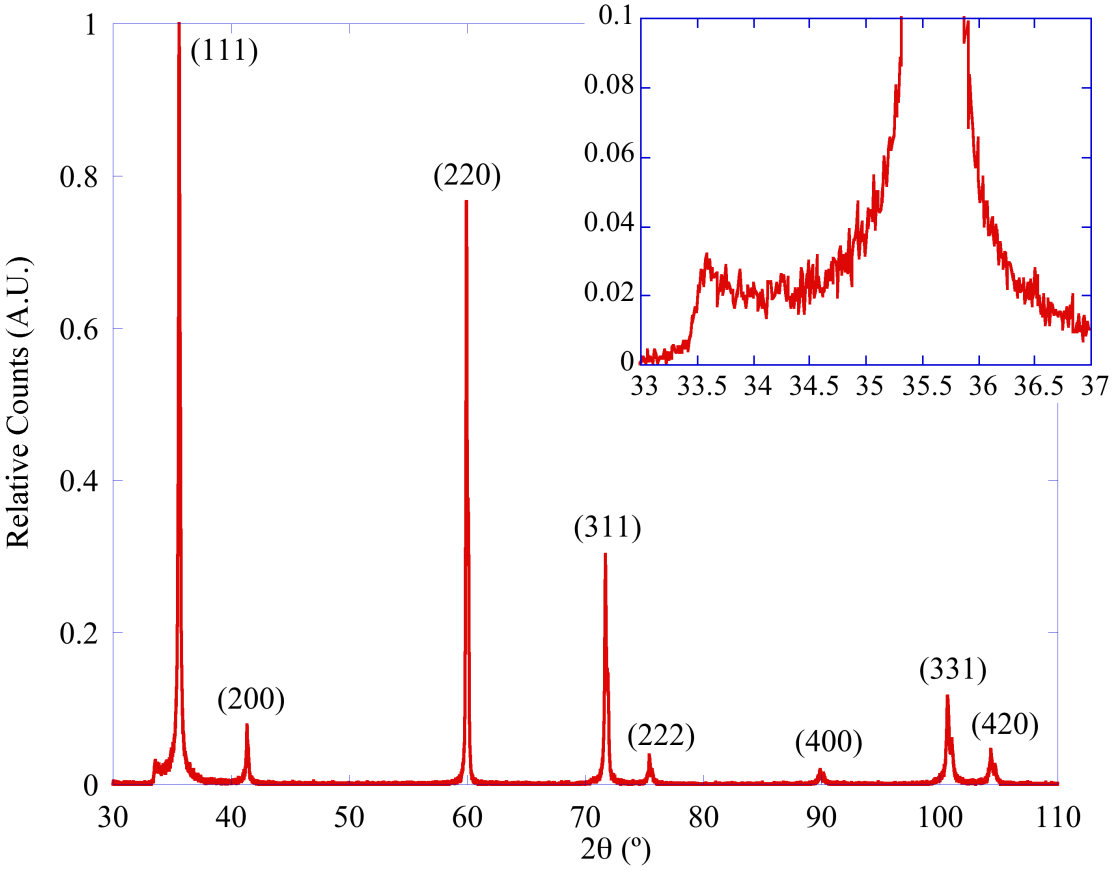

Figure 3.3: Cu Kα XRD of the SiC substrates provided by Rohm and Haas Inc. All the peaks correspond to β-SiC. The inlay shows the broad plateau near the (111) peak that is characteristic of stacking faults in SiC [74]

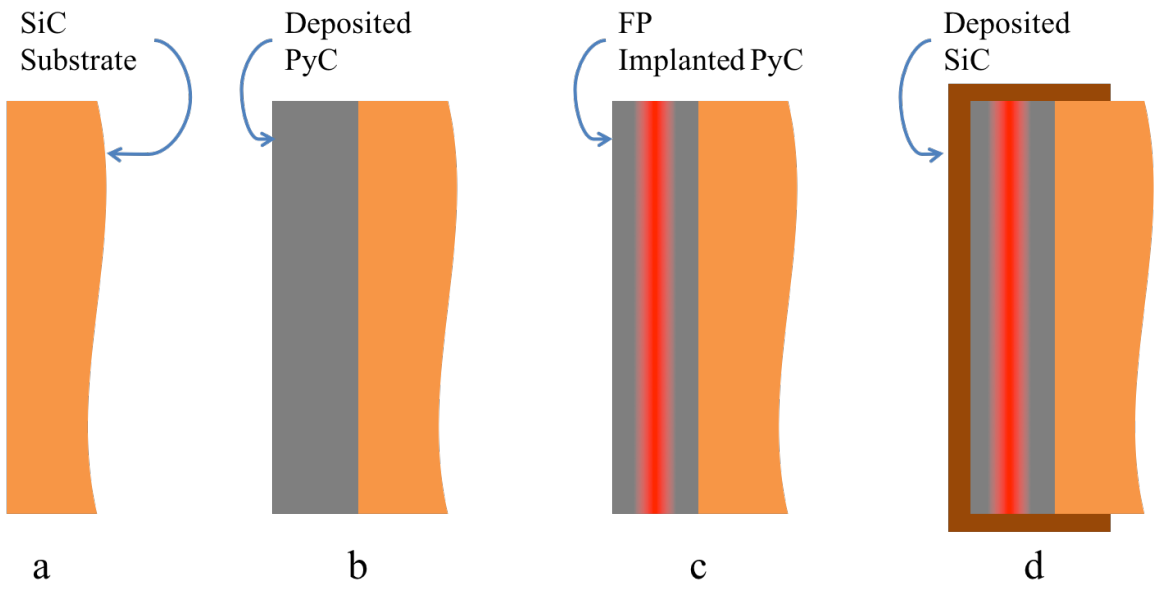

Figure 3.4: Schematic illustration of the four steps in preparing the novel diffusion couple: (a) Preparation of the substrate to create a sharp interface with the PyC (b) Deposition of a layer of CVD PyC (c) Implantation of an FP into the PyC (d) Deposition of a SiC cap to retain the FP within the diffusion couple at high temperature.

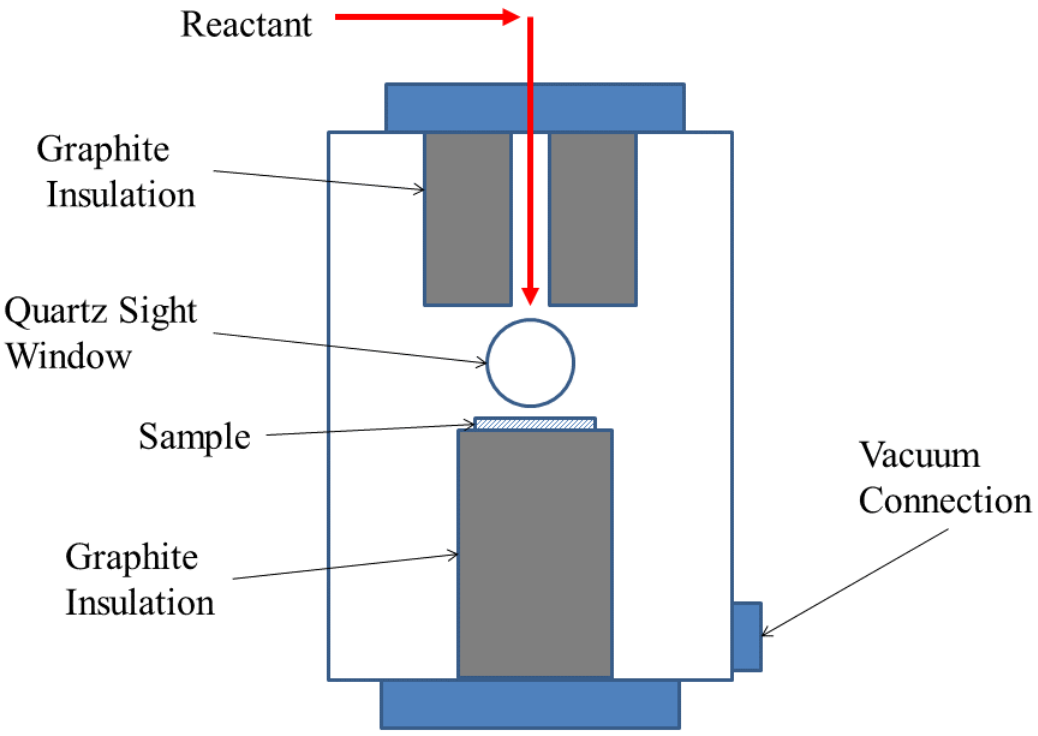

Figure 3.5: A schematic showing orientation of sample in the graphite furnace with reactant flow and vacuum port.

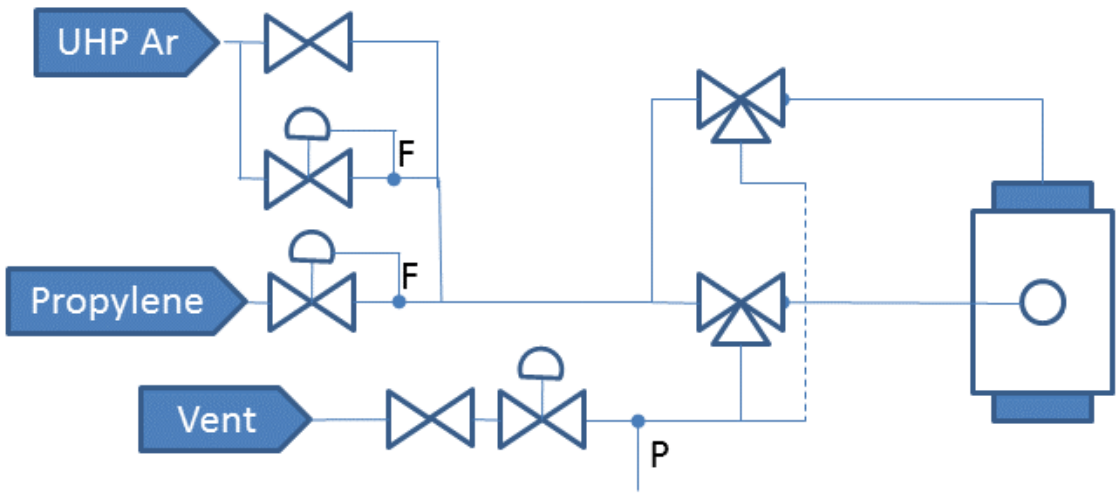

Figure 3.6: A schematic of the gas flow in newly designed PyC deposition panel fitted for the graphite furnace. Two three way valves allow for reconfiguring the furnace to run thermal annealings as well. Mass flow controllers are used to control the argon-propylene mixture. A vent allows for a constant flow of gas through the system for thermal annealings

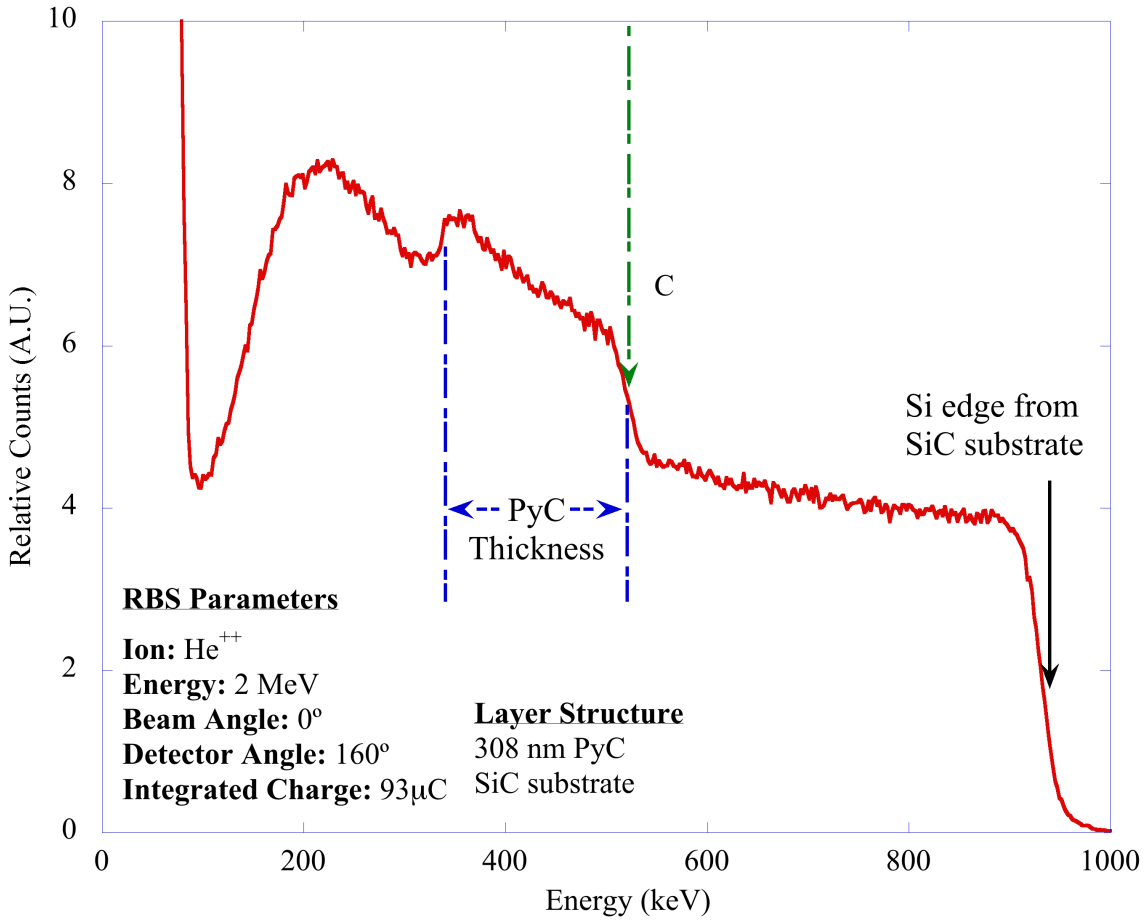

Figure 3.7: RBS spectrum for a 308nm thick PyC layer on a SiC substrate. Green arrow marks the front surface energy for the PyC, while blue arrows mark the width of the carbon plateau from the PyC and the Si edge from the SiC

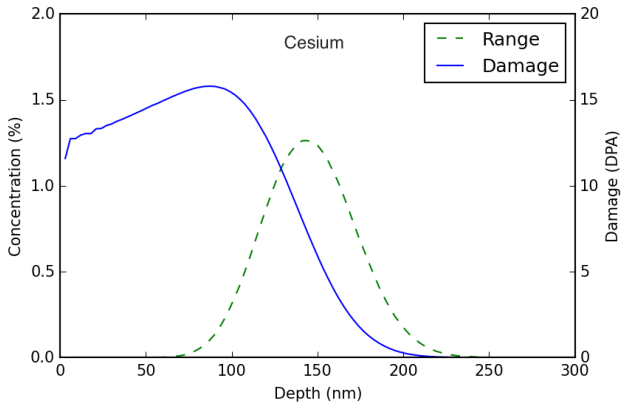

(a)

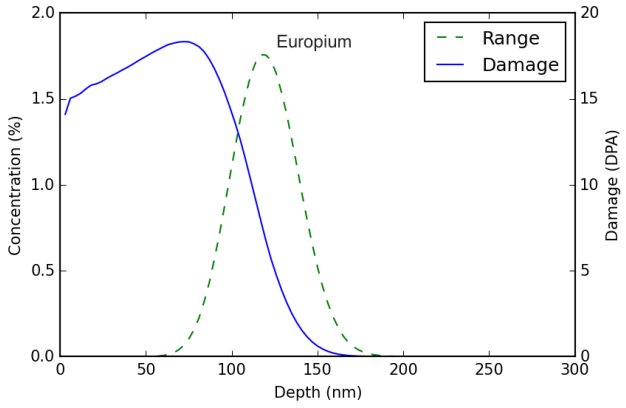

(b)

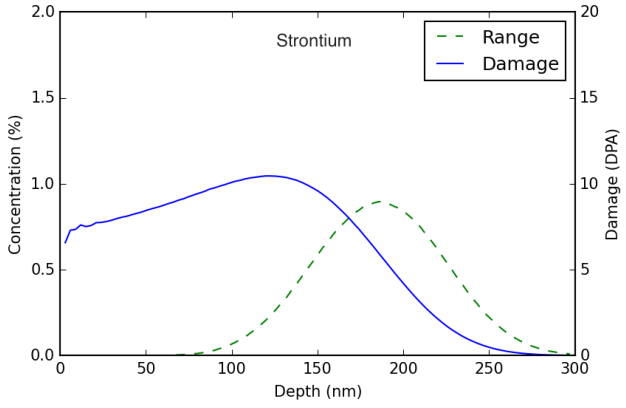

(c)

Figure 3.8: Implantation range and damage for 400 keV (a) cesium, (b) and (c) strontium into PyC to a fluence of 10^{16} cm^{-2} as simulated by SRIM using a damage energy of 20eV [79, 81].

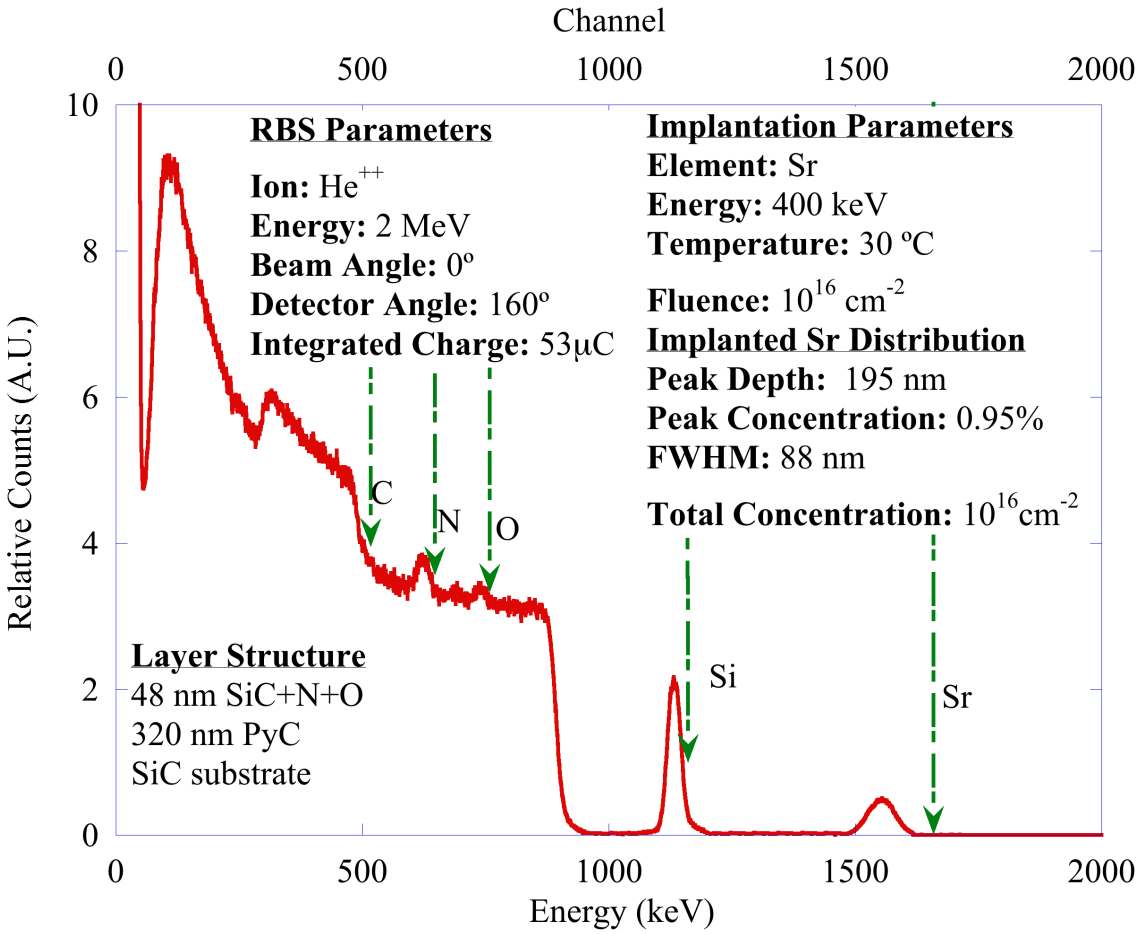

Figure 3.9: RBS spectrum of a diffusion couple for strontium prior to annealing. The front surface energies for the various elements are marked by arrows with dashed green lines.

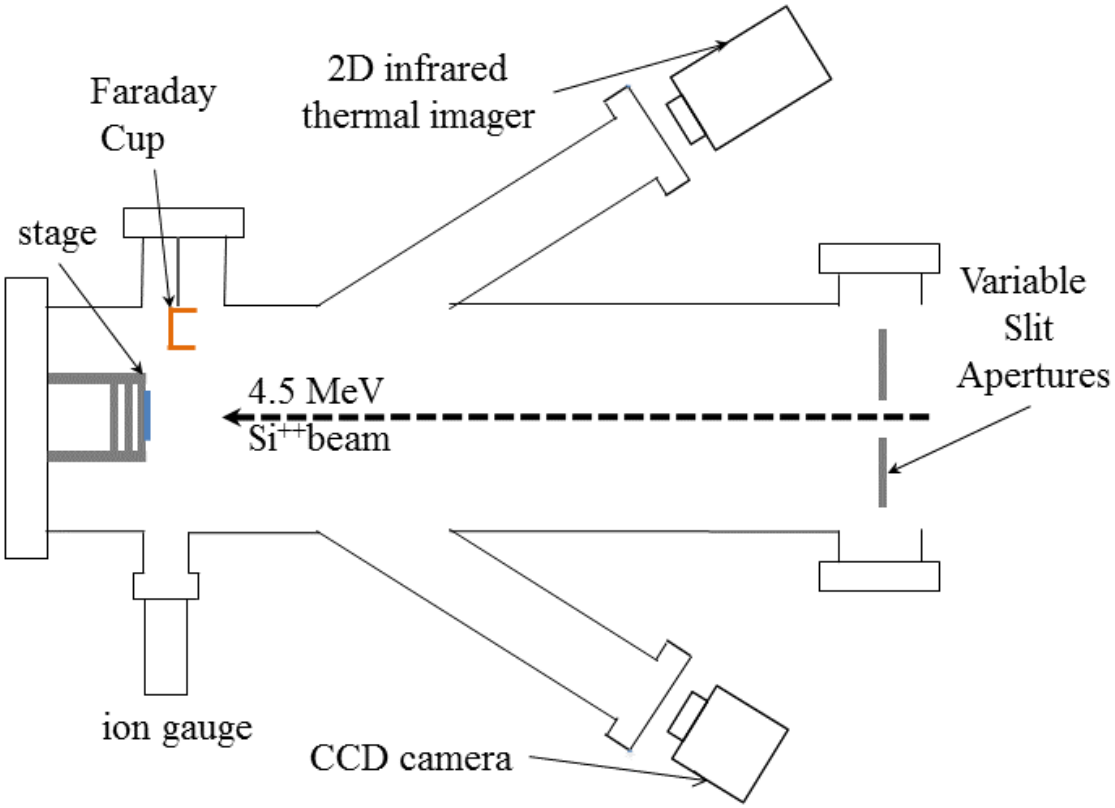

Figure 3.10: Schematic of the irradiation chamber. A 4.5 MeV Si^{++} beam is used to irradiate the sample. A Faraday cup that can be inserted directly in front of the sample is used to measure dose. A set of variable slit apertures is used to control the irradiation area. A thermocouple on the stage and the 2D infrared thermal imager are used to monitor temperature. A CCD camera allows for monitoring of the entire setup. An ion gauge placed close to the stage monitors vacuum in the chamber.

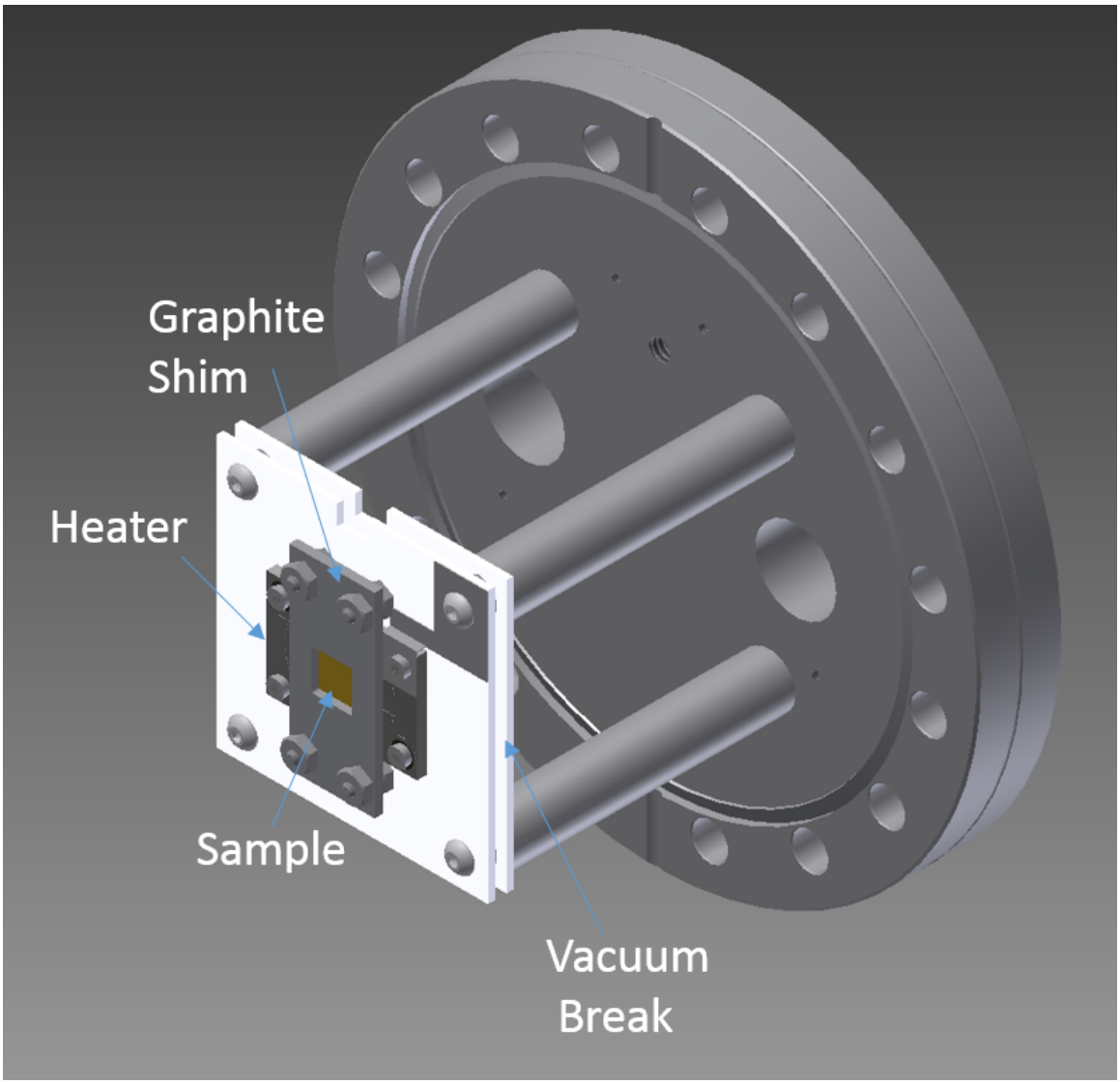

Figure 3.11: A 3D CAD model of the high temperature irradiation stage with the primary parts labeled.

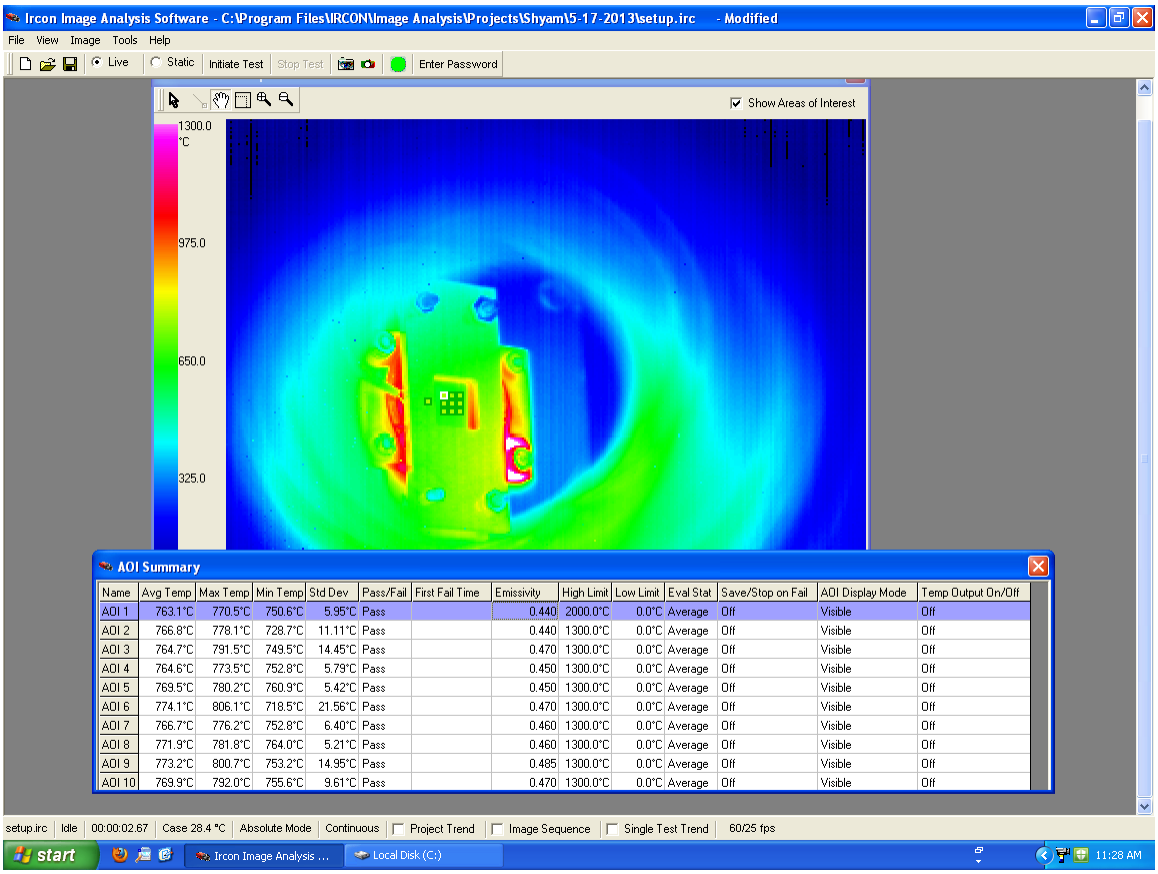

Figure 3.12: The 2D infrared pyrometer software used to measured the surface temperature of the sample. This is a calibration at 750°C. Note the 3 x 3 array of areas of interest on the sample. An additional area of interest on the graphite shim is used to ensure the beam spread is minimal.

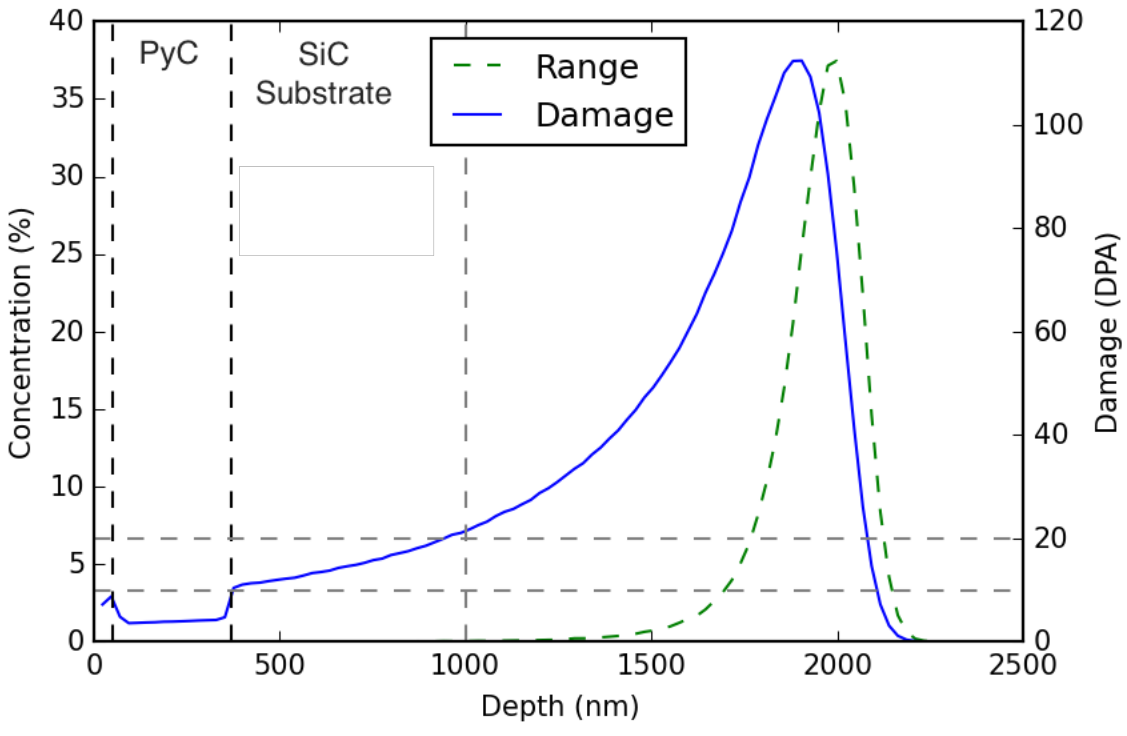

Figure 3.13: SRIM calculation of 4.5 MeV Si^{++} into the diffusion couple [81]. The layers are differentiated by dashed black lines. Gray lines mark the 10 and 20 dpa dose points which correspond to the PyC/SiC interface and 650 nm into the SiC substrate, where all the radiation enhanced diffusion is limited to.

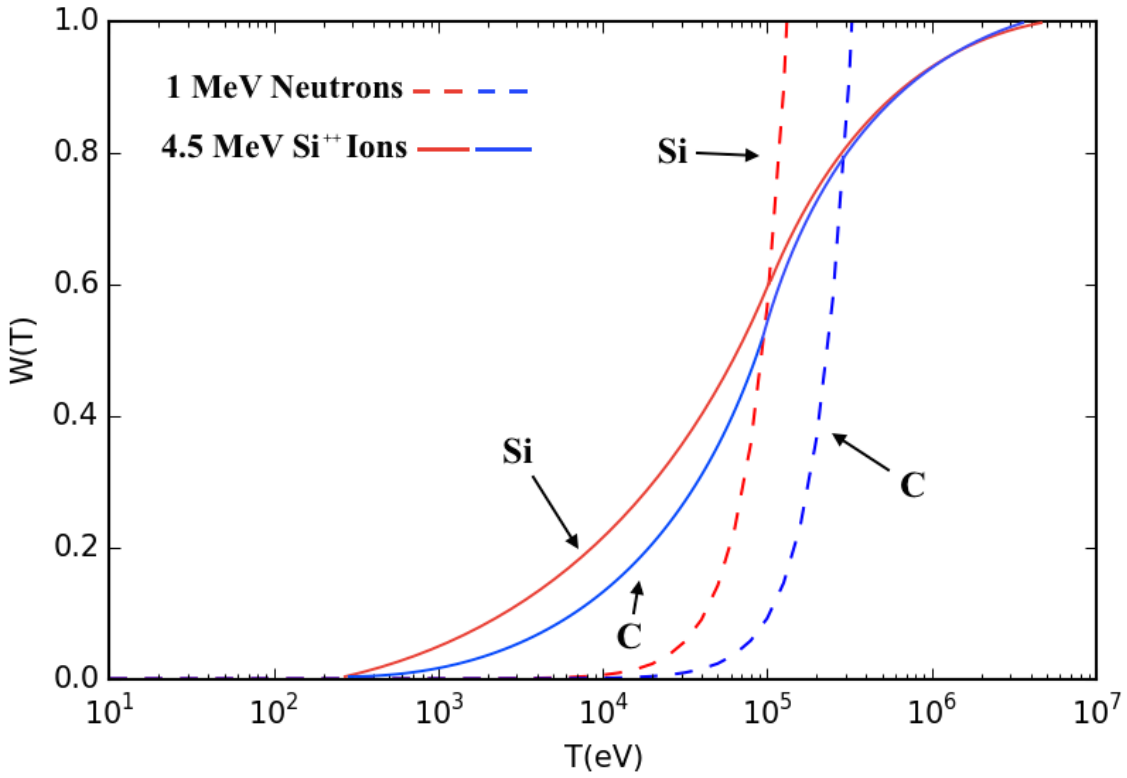

Figure 3.14: Weighted recoil spectra for 4.5 MeV Si++ ions and 1 MeV neutrons in SiC.

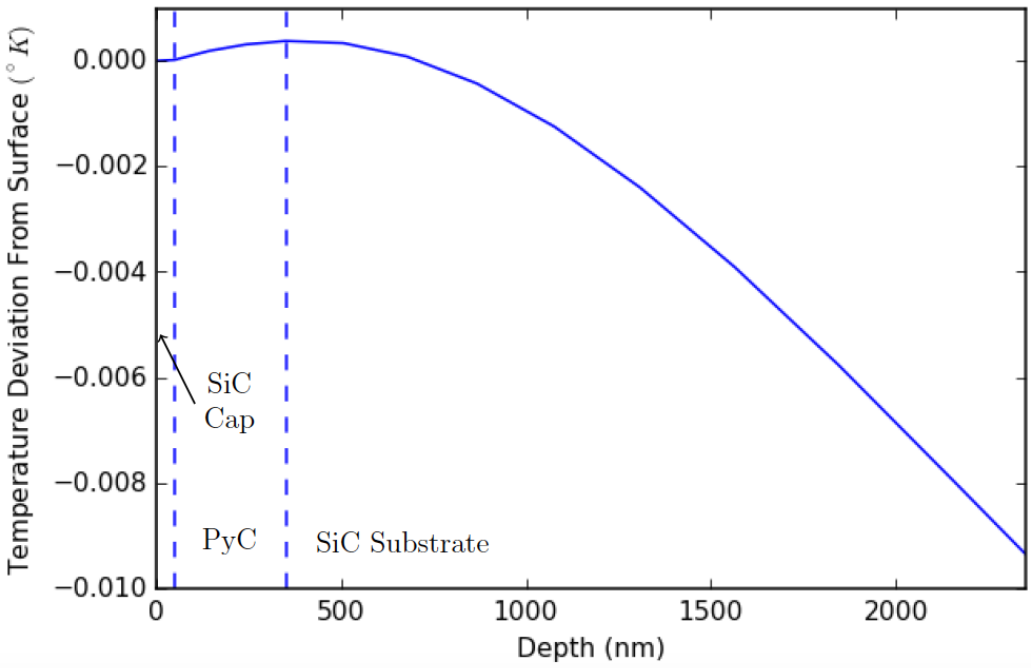

Figure 3.15: Temperature deviation within a diffusion couple as a function of depth for an $1,100$°C 4.5 MeV silicon ion irradiation

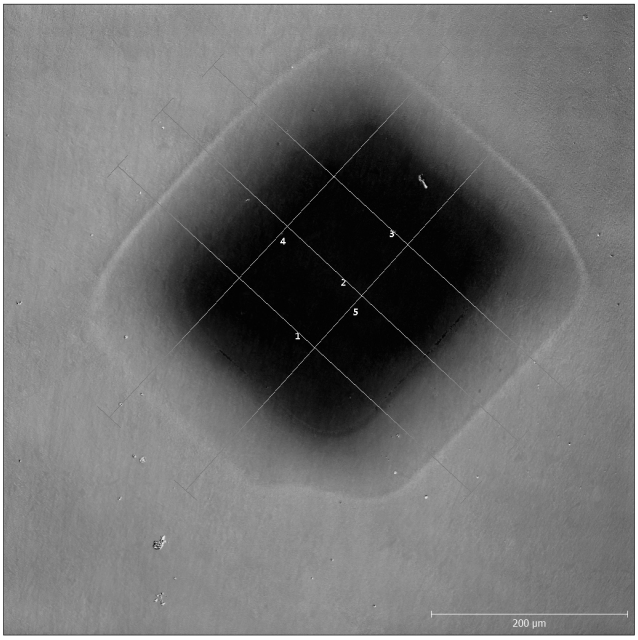

(a)

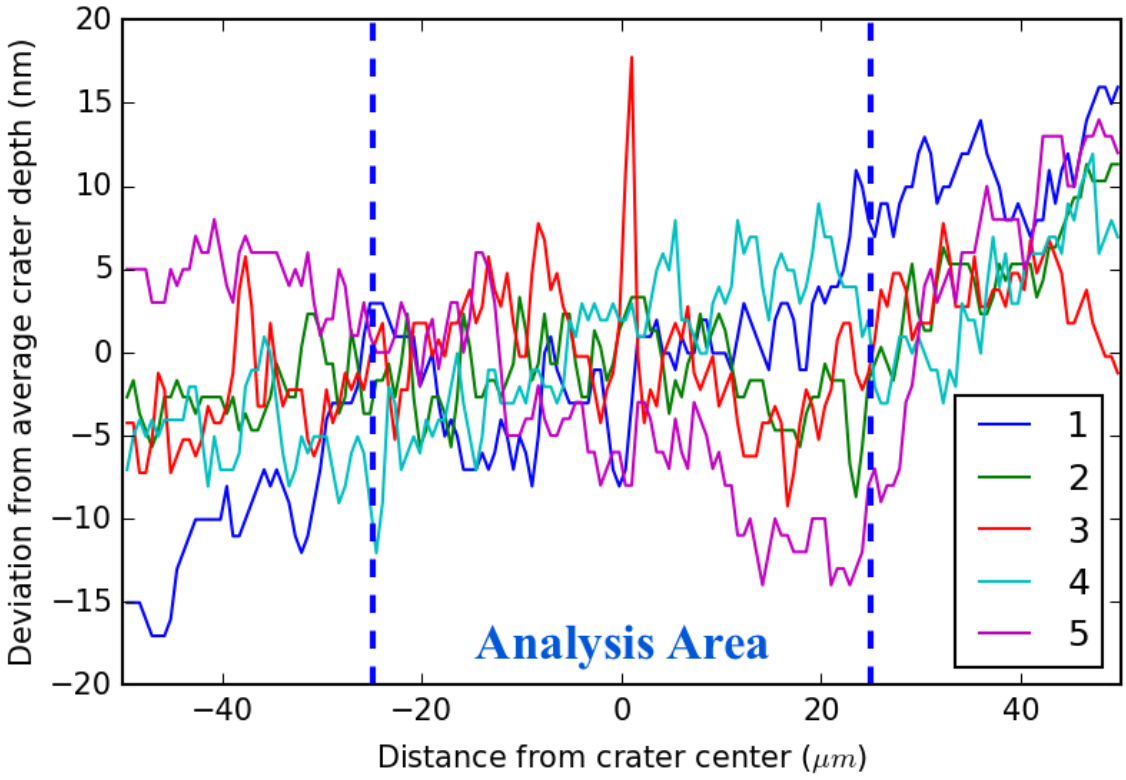

(b)

Figure 3.16: (a) Optical image of a sputter crater from the ToF-SIMS analysis. (b) Optical profilometry scans corresponding to the lines marked 1-5 in (a). The scans have been adjusted to present the deviation from the crater base. Dashed blue lines indicate the analysis area

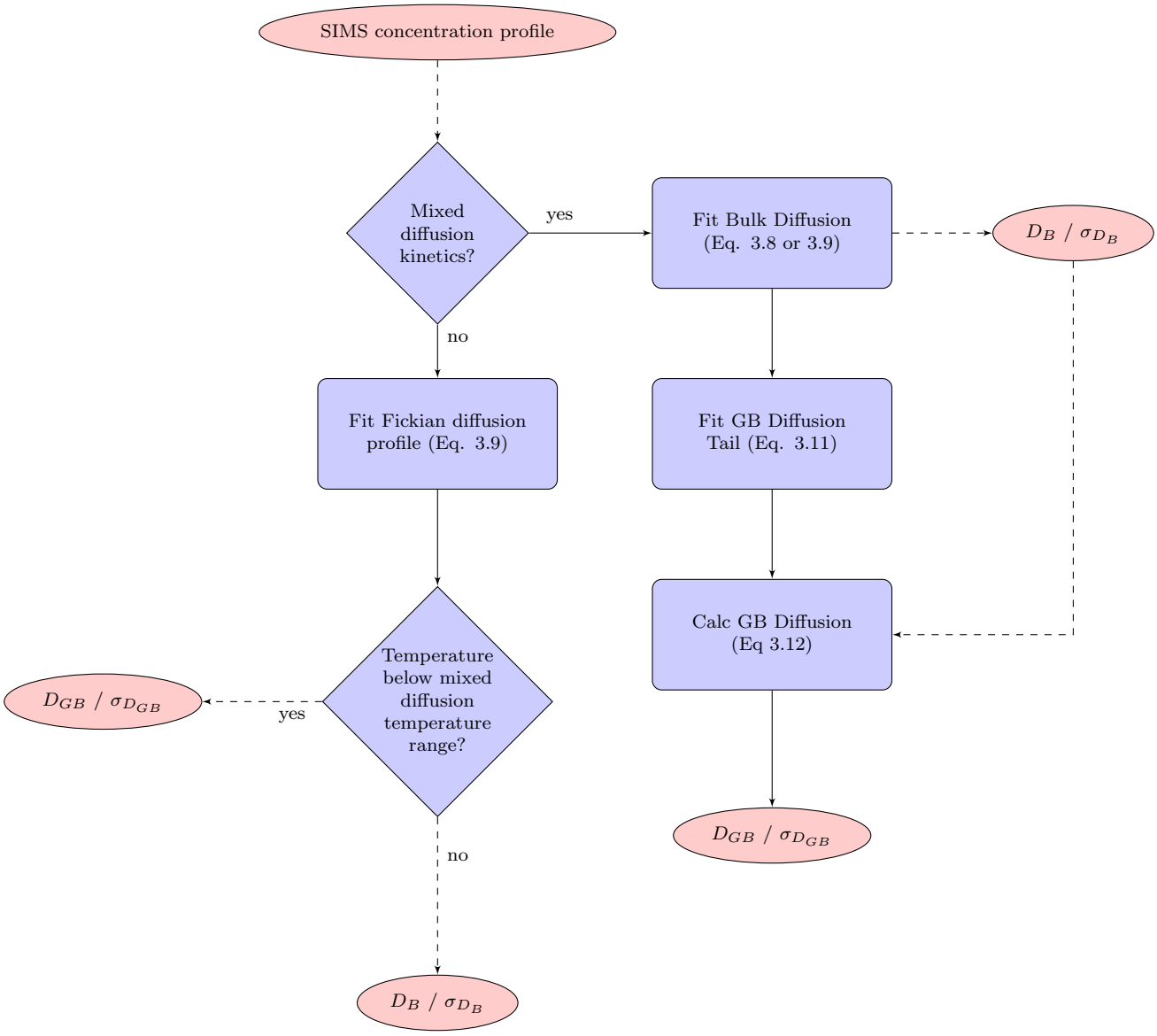

Figure 3.17: Flow chart for the diffusion analysis process

CHAPTER IV

Results

This chapter will present the FP concentration profiles resulting from thermal annealings or ion irradiations and measured using time of flight secondary ion mass spectrometry (ToF-SIMS), and fits to the diffusion equations detailed in Experimental Method chapter. Annealing temperatures ranged from 900°C to 1,300°C. The ion irradiations were conducted between 900°C and 1,100°C.

4.1 Thermally Annealed Diffusion Couples

Figure 4.1 shows the ToF-SIMS profile for a strontium diffusion couple before annealing. It revealed that the implanted FP was fully contained within the PyC. Vertical blue lines are used to mark the boundaries between the SiC cap, PyC and the SiC substrate. The sharp interfaces between the PyC and SiC layers on the as-fabricated diffusion couple exhibit widths, as defined by the full width at half maximum, of approximately 12s of sputtering time or 8 nm after calibration of the sputtering rate. This interface width is a systemic source of error due to both the roughness of the PyC/SiC interface and the flatness and planarity of the SIMS crater.

While several temperatures between 900°C and 1,300°C were evaluated, not all provided usable diffusion coefficients. A set of criteria was developed to determine if the diffusion coefficient from a concentration profile should be included in the diffusion

study:

1. The PECVD cap must be present.

2. FP concentration at the interface must be above the minimum detectability limit for SIMS.

3. Concentration profile must fit either types A,B, or C diffusion.

4. Minimum error on the diffusion coefficient must be less than the value of the diffusion coefficient.

The raw data from the depth profile of the first $1,100°$C:10hr strontium diffusion couple is shown in Figure 4.2. The interfaces between the PyC and SiC substrate layers have broadened to 11 nm in width indicating that silicon has diffused into the PyC from both the SiC cap and SiC substrate. This occurred at all temperatures and for all FPs investigated. Strontium in the PyC has diffused into both the SiC cap and into the SiC substrate. The strontium sensitivity in the PyC is an order of magnitude lower than in the SiC. As a result, one count in the PyC represents ten times the strontium concentration as does one count in the SiC. Carbon was not monitored due to poor sensitivity in positive mode (< 20 counts at each depth), which was evident for all diffusion couples in the as-received and annealed cases. The sensitivity factor at the interfaces changes as the interface is sputtered away and makes it very difficult to deconvolute the actual concentration profile at the interface. For this reason, the concentration in the interface region is not considered for analysis, which could have provided the relative solubilities in the SiC and the PyC.

The following three sub-sections present the concentration vs depth profiles for cesium, europium, and strontium diffusion in the SiC. The concentration profiles are limited to the SiC substrate where reduced senstivity factors (RSF) and sputter-rates can be applied to convert time and counts into depth in nm and concentration in

ppm. The diffusion equation (Eq. 3.9) was used to fit single mechanism profiles. Two mechanism profiles were fit using Eq. 3.9 for the slow diffusion mechanism and Eq. 3.10 for the fast diffusion mechanism based on the formalisms of the Fisher model. The slow mechanism is assumed to be bulk diffusion and the fast mechanism is assumed to be grain boundary diffusion in this chapter. The argument in support of this diffusion mode will be made in the Discussion section.

Table 4.1 lists the bulk diffusion equations for the bulk diffusion fits presented in the following three sub-sections. Table 4.2 list the grain boundary tail equations for the grain boundary diffusion fits presented in the following three sub-sections. The diffusion profile naming scheme is as follows: FP-Temperature:time-profile number. The $1,100$°C:10h annealing condition for strontium is the only cause in which multiple diffusion couples were fabricated and annealed. Sr-1100:10h-01 and Sr-1100:10h-02 are from one diffusion couple while, Sr-1100:10h-03 and Sr-1100:10h-04 are from the second. Tables 4.1 and 4.2 also list the Pearson χ^2, which is an indicator of the goodness of fit, and the p-value, which is the probability that the fit accurately describes the fitted data. Table 4.3 list the bulk and grain boundary diffusion coefficients calculated from the fits in Table 4.1 and Table 4.2.

4.1.1 Strontium

Figure 4.3 is a concentration profile of the $1,100$°C:10hr annealed condition for strontium. This profile for strontium exhibits two distinct mechanisms, believed to be bulk and grain boundary diffusion. The steeper depth profile is due to bulk diffusion and the long diffusion tail is believed to be due to grain boundary diffusion. A green dashed line shows the instantaneous source fit from Eq. 3.9 for bulk diffusion and a blue dashed line shows the fit for the grain boundary tail using Eq. 3.10. The bulk region reaches 30 nm into the SiC, while the grain boundary tail extends to 200 nm into the SiC.

Figure 4.4c presents (a) a diffraction contrast image and (b) a high angle annular dark field (HAADF) image of the PyC/SiC interface and SiC substrate from the 1,100°C:10hr-01 condition. The PyC/SiC interface is clearly visible in the HAADF image, while the grain structure and the locations of grain boundaries are visible in the diffraction contrast image. A STEM-EDS map of the strontium concentration for the region designated by the red box is shown in (c) . The PyC/SiC interface was identified from the HAADF image and is marked by a dashed white-line. The strontium concentration is high at the PyC/SiC interface. A small amount of strontium has diffused into the SiC substrate on the right side of the map. Figure 4.4d shows the corresponding depth profile where the x-axis corresponds to the depth below the PyC/SiC interface indicated in Figure 4.4c. The concentration measured at the interface by EDS is comparable to the concentration measured at the interface by SIMS and presented in Figure 4.3. The depth of penetration is also comparable to that measured by SIMS for the bulk diffusion front. No strontium was detected along grain boundaries due to the sensitivity limit of the ChemiSTEM EDS, which was estimated at 0.01%.

Figure 4.5 is the concentration profile in the SiC substrate of the 900°C:40hr annealed condition for strontium. The concentration profile exhibits a single diffusion mechanism that extends 25 nm into the SiC and can be fit with the instantaneous source formalism from Eq. 3.9. Figure 4.6 is the concentration profile in the SiC substrate of the 1,066°C:10hr annealed condition for strontium. The concentration profile exhibits two mechanisms that are assumed to be bulk and grain boundary diffusion. The bulk region extends further into the SiC to a distance of 25 nm, while the grain boundary tail reaches 92 nm into the SiC. The 1,066°C:10hr profile is clearly in the mixed diffusion kinetic regime and the 900°C:40hr is clearly not in the mixed diffusion regime. The Harrison formalism for diffusion used in this study indicates that all diffusion below the mixed diffusion kinetics dominant temperature regime is

due to fast diffusion, which in this study is assumed to be grain boundary diffusion. Thus the 900°C:40hr profile is attributed to grain boundary diffusion.

Two separate 1,100°C:10hr diffusion couples were prepared for strontium in two separate annealings. Two separate SIMS depth profiles were measured for each 1,100°C:10hr diffusion couple. Figure 4.3 presented the first concentration profile for the first diffusion couple. Figure 4.7 presents the second concentration profile for the same diffusion couple. Figures 4.8 and 4.9 present the two profiles from the second diffusion couple. The first three profiles all clearly exhibit two diffusion mechanisms that are fit with bulk and grain boundary diffusion formalisms from Eq. 3.9 and 3.10. The last profile might have a small bulk penetration region that can be fit with Eq. 3.9, but is excluded from this study due to difficulty in determining if that region is an artifact or an actual diffusion front. The grain boundary tail was fit using Eq. 3.10 rather than Eq. 3.9 as the single mechanism fit did not conform to the tail region. The bulk penetration depth ranged from 30 nm to 50 nm for the first three profiles. The grain boundary penetration depth ranged from 125 nm to 250 nm over all 4 profiles.

Two SIMS depth profiles were also measured from one 1,200°C:10hr strontium diffusion couple presented in Figures 4.10 and 4.11. The first profile exhibits mixed diffusion kinetics and was fit using the two-mechanism formalism using Eq. 3.9 and 3.10. The second profile appears to exhibit one mechanism, but does not conform to a normal diffusion profile between the PyC/SiC interface and what is likely the fast diffusion tail. The single mechanism formalism from Eq. 3.9 fit the profile, but the large penetration depth of 200 nm did not fit with the rest of the bulk diffusion measurements, but corresponded more to the grain boundary diffusion measurements which were exhibiting diffusion depths on the order of 200 nm, designating this diffusion coefficient as due to grain boundary diffusion.

Figure 4.12 is the concentration vs depth profile for the 1,300°C:10hr annealed

condition for strontium. This profile exhibits mixed diffusion kinetics and was fit using the two mechanism formalism. The bulk diffusion front extends to nearly 100 nm into the SiC, while the grain boundary tail reaches nearly 600 nm into the SiC.

4.1.2 Europium

Figures 4.13 is the concentration profile for europium diffusion in SiC at $1,100$°C:10hr. The profile exhibited mixed diffusion kinetics that were fit with the same two mechanism formalism used for strontium with Eq. 3.9 for the bulk region and Eq. 3.10 for the grain boundary diffusion tail. The noise in the europium signal is due to the noise in the silicon signal which is used as the reference for calculating concentration. Several profiles were conducted on this sample and all exhibited this noise for this one condition. This will show up in the error for the calculated diffusion coefficients.

Figure 4.14 and 4.15 are two concentration profiles from the same diffusion couple annealed at $1,200$°C10hr. Both exhibit mixed diffusion kinetics and can be fit with two separate mechanisms. The second profile begins at a concentration that is two orders of magnitude lower than the first. The second profile also has a much smaller bulk penetration depth at 50 nm vs. 200 nm.

Figure 4.16 is the concentration profile for europium diffusion at $1,300$°C10hr. There is a clear bulk penetration region that extends 150 nm into the SiC and a long grain boundary tail that extends over a micron into the SiC.

4.1.3 Cesium

Figure 4.17-4.20 are the concentration profiles for cesium diffusion in SiC for the 900°C:40h through $1,300$°C:10hr conditions. Cesium diffusion exhibits mixed diffusion kinetics that are fit with the two mechanism formalism used for strontium and europium using Eq. 3.9 and 3.10 in this temperature range. Both bulk and grain boundary penetration depths are very shallow at 20nm and 60nm at 900°C:40hr, but

steadily increase to nearly 50 nm for bulk diffusion and 250 nm for grain boundary diffusion at 1,300°C:10hr.

4.2 Ion Irradiated Diffusion Couples

The following three sub-sections report the concentration profiles for strontium, europium, and cesium diffusion under ion irradiation conditions at a dose rate of $4.6 \times 10^{-4} dpa\ s^{-1}$ to a total dose of 10 dpa between 900°C and 1,100°C. All three elements exhibited mixed diffusion kinetics that are fit with the two-mechanism formalism using Eq. 3.9 for the bulk region and Eq. 3.10 for the grain boundary tail. Table 4.4 lists the bulk diffusion equations for the bulk diffusion fits presented in the following three sub-sections. Table 4.5 list the grain boundary tail equations for the grain boundary diffusion fits presented in the following three sub-sections. Tables 4.4 and 4.5 also list the Pearson χ^2, which is an indicator of the goodness of fit, and the p-value, which is the probabitliy that the fit accurately describes the fitted data. Table 4.6 list the bulk and grain boundary diffusion coefficients calculated from the fits in Table 4.4 and Table 4.5.

4.2.1 Strontium

Figures 4.21-4.23 are the concentration profiles for strontium diffusion under ion irradiation from 900°C:6hr:10dpa through 1,100°C:6hr:10dpa. At 900°C:6hr:10dpa the bulk diffusion region reaches 100 nm into the SiC, while the grain boundary tail is nearly flat and extends past the limits of the SIMS depth profile. At 1,000°C:6hr:10dpa the bulk diffusion region extends nearly 120 nm into the SiC, while the grain boundary diffusion tail only reaches 600 nm and is measured near the limits of the SIMS sensitivity at 1 ppm. At 1,100°C:6hr:10dpa the penetration depth due to bulk diffusion increases to 200 nm, and that due to grain boundary diffusion reaches nearly 900 nm.

4.2.2 Europium

Figures 4.24-4.26 are the concentration profiles for europium diffusion under ion irradiation from 900°C through 1,100°C.At 900°C:6hr:10dpa the bulk diffusion region reaches 30 nm into the SiC, while the grain boundary tail reaches nearly 70 nm into the SiC. At 1,000°C:6hr:10dpa the penetration depths increase to 40 nm for the bulk diffusion region and 100 nm for the grain boundary tail. At 1,100°C:6hr:10dpa the overall concentrations within the SiC dropped significantly reducing the bulk penetration depth to 20nm, and the grain boundary tail penetration depth to 60 nm.

4.2.3 Cesium

Figures 4.27-4.29 are the concentration profiles for cesium diffusion under ion irradiation from 900°C:6hr:10dpa through 1,100°C:6hr:10dpa. At 900°C:6hr:10dpa the bulk diffusion region reaches 30 nm into the SiC, while the grain boundary tail reaches nearly 70 nm into the SiC. At 1,000°C:6hr:10dpa the penetration depths increase to 40 nm for the bulk diffusion region and 100 nm for the grain boundary tail. At 1,100°C:6hr:10dpa the overall concentrations within the SiC dropped significantly reducing the bulk penetration depth to 20nm, and the grain boundary tail penetration depth to 60 nm.

4.2.4 Interface Concentrations

Table 4.7 presents the maximum interface concentrations in the thermally annealed and ion irradiated conditions. Between 900°C and 1,100°C all three elements exhibit mixed diffusion kinetics at all three temperatures for the irradiated condition. Since strontium was the only element observed to exhibit grain boundary diffusion dominant kinetics at 900°C under purely thermal conditions, it is also the only element to change diffusion regime in this study. Both cesium and europium exhibit a significant decrease in the interface concentration under irradiation vs. thermal annealing,

while strontium exhibits a significant increase at 900°C that reduces in magnitude at 1,100°C. The 900°C interfacial enrichment for strontium is likely due to the difference in diffusion regime from grain boundary diffusion dominant, where the interface concentration is the grain boundary concentration, to mixed diffusion dominant, where the interface concentration is the matrix concentration.

Profile	Fit	χ^2_P
Cs-900:40h-01	$C(ppm) = 2,400exp\left(\frac{x^2}{220nm^2}\right)$	3.5, p=0.47
Cs-1100:10h-01	$C(ppm) = 1,200exp\left(\frac{x^2}{230nm^2}\right)$	1.7, p=0.79
Cs-1200:10h-01	$C(ppm) = 1,300exp\left(\frac{x^2}{360nm^2}\right)$	3, p=0.55
Cs-1300:10h-01	$C(ppm) = 58exp\left(\frac{x^2}{790nm^2}\right)$	2.4, p=0.66
Eu-1100:10h-01	$C(ppm) = 10,000exp\left(\frac{x^2}{250nm^2}\right)$	3.3, p=0.51
Eu-1200:10h-01	$C(ppm) = 8,200exp\left(\frac{x^2}{1,200nm^2}\right)$	1.9, p=0.75
Eu-1200:10h-02	$C(ppm) = 93exp\left(\frac{x^2}{500nm^2}\right)$	3.6, p=0.46
Eu-1300:10h-01	$C(ppm) = 410exp\left(\frac{x^2}{9,400nm^2}\right)$	2.8, p=0.59
Sr-1066:10h-01	$C(ppm) = 630exp\left(\frac{x^2}{11nm^2}\right)$	1.4, p=0.84
Sr-1100:10h-01	$C(ppm) = 710exp\left(\frac{x^2}{160nm^2}\right)$	1.2, p=0.87
Sr-1100:10h-02	$C(ppm) = 1,000exp\left(\frac{x^2}{250nm^2}\right)$	1.5, p=0.82
Sr-1100:10h-03	$C(ppm) = 35exp\left(\frac{x^2}{79nm^2}\right)$	2.8, p=0.59
Sr-1200:10h-01	$C(ppm) = 1,000exp\left(\frac{x^2}{1000nm^2}\right)$	1.8, p=0.77
Sr-1300:10h-01	$C(ppm) = 240exp\left(\frac{x^2}{23,000nm^2}\right)$	2.2, p=0.69

Table 4.1: Bulk diffusion fits to FP concentration profiles from thermal annealing. χ^2_P is the indicator of goodness of fit. The corresponding p-values are the probability that the fit accurately models the data. The sample naming scheme is as follows: FP-Temperature:time-profile number. The 1100C:10h annealing condition for strontium is the only cause in which multiple diffusion couples were fabricated and annealed. Sr-1100:10h-01 and Sr-1100:10h-02 are from one diffusion couple while, Sr-1100:10h-03 and Sr-1100:10h-04 are from the second.

Profile	Fit	χ^2_P
Cs-900:40h-01	$C(ppm) = 75exp\left(-0.091nm^{-6/5}x^{6/5}\right)$	4.2, p=0.52
Cs-1100:10h-01	$C(ppm) = 28exp\left(-0.039nm^{-6/5}x^{6/5}\right)$	3.8, p=0.57
Cs-1200:10h-01	$C(ppm) = 28exp\left(-0.044nm^{-6/5}x^{6/5}\right)$	3.5, p=0.62
Cs-1300:10h-01	$C(ppm) = 4.5exp\left(-0.017nm^{-6/5}x^{6/5}\right)$	3.2, p=0.67
Eu-1100:10h-01	$C(ppm) = 110exp\left(-0.028nm^{-6/5}x^{6/5}\right)$	3.5, p=0.62
Eu-1200:10h-01	$C(ppm) = 8.1exp\left(-0.015nm^{-6/5}x^{6/5}\right)$	3.3, p=0.65
Eu-1200:10h-02	$C(ppm) = 17exp\left(-0.033nm^{-6/5}x^{6/5}\right)$	3.9, p=0.56
Eu-1300:10h-01	$C(ppm) = 18exp\left(-0.0029nm^{-6/5}x^{6/5}\right)$	3.1, p=0.68
Sr-900:40h-01	$C(ppm) = 61exp\left(\frac{x^2}{11nm^2}\right)$	2.8, p=0.73
Sr-1066:10h-01	$C(ppm) = 680exp\left(-0.053nm^{-6/5}x^{6/5}\right)$	1.6, p=0.90
Sr-1100:10h-01	$C(ppm) = 590exp\left(-0.021nm^{-6/5}x^{6/5}\right)$	2.5, p=0.77
Sr-1100:10h-02	$C(ppm) = 47exp\left(-0.034nm^{-6/5}x^{6/5}\right)$	3.2, p=0.67
Sr-1100:10h-03	$C(ppm) = 4.3exp\left(-0.037nm^{-6/5}x^{6/5}\right)$	4.6, p=0.46
Sr-1100:10h-04	$C(ppm) = 36exp\left(-0.012nm^{-6/5}x^{6/5}\right)$	3.7, p=0.59
Sr-1200:10h-01	$C(ppm) = 120exp\left(-0.026nm^{-6/5}x^{6/5}\right)$	3.3, p=0.65
Sr-1200:10h-02	$C(ppm) = 85exp\left(-0.024nm^{-6/5}x^{6/5}\right)$	4.1, p=0.53
Sr-1300:10h-01	$C(ppm) = 10exp\left(-0.022nm^{-6/5}x^{6/5}\right)$	2.6, p=0.76

Table 4.2: Grain boundary diffusion fits to FP concentration profiles from thermal annealing. χ^2_P is the indicator of goodness of fit.

Profile	Temperature °C	Location	$D_B(cm^2s^{-1})$	$s\delta D_{GB}(cm^3s^{-1})$	Relative Error (%)
Cs-900:40h-01	900	PNNL	$1.5 \pm 0.96 \times 10^{-17}$	$1.6 \pm 0.88 \times 10^{-24}$	49
Cs-1100:10h-01	1100	PNNL	$6.5 \pm 4.7 \times 10^{-17}$	$1.7 \pm 1.6 \times 10^{-22}$	18
Cs-1200:10h-01	1200	PNNL	$9.9 \pm 2.9 \times 10^{-17}$	$4.7 \pm 2.4 \times 10^{-22}$	10
Cs-1100:10h-01	1300	PNNL	$2.2 \pm 1.6 \times 10^{-16}$	$3.9 \pm 1.2 \times 10^{-21}$	34
Eu-1100:10h-01	1100	IEN	$6.8 \pm 4.3 \times 10^{-18}$	$1.5 \pm 1.2 \times 10^{-22}$	3
Eu-1200:10h-01	1200	IEN	$3.4 \pm 1.0 \times 10^{-16}$	$8.7 \pm 3.0 \times 10^{-21}$	7
Eu-1200:10h-02	1200	IEN	$1.4 \pm 0.89 \times 10^{-16}$	$1.3 \pm 0.27 \times 10^{-20}$	4
Eu-1300:10h-01	1300	IEN	$2.6 \pm 0.47 \times 10^{-15}$	$3.7 \pm 0.67 \times 10^{-20}$	6
Sr-900:40h-01	900	PNNL	ND	$6.9 \pm 2.6 \times 10^{-25}$	
Sr-1066:10h-01	1066	IEN	$3 \pm 0.78 \times 10^{-18}$	$6.7 \pm 0.93 \times 10^{-23}$	10
Sr-1100:10h-01	1100	PNNL	$4.4 \pm 1.4 \times 10^{-17}$	$7.6 \pm 2.4 \times 10^{-22}$	6
Sr-1100:10h-02	1100	IEN	$6.8 \pm 4.3 \times 10^{-17}$	$3.1 \pm 1.7 \times 10^{-22}$	6
Sr-1100:10h-03	1100	IEN	$2.2 \pm 1.5 \times 10^{-17}$	$2.5 \pm 1.2 \times 10^{-22}$	7
Sr-1100:10h-04	1100	IEN	ND	$1.1 \pm 0.58 \times 10^{-21}$	18
Sr-1200:10h-01	1200	PNNL	$2.8 \pm 0.84 \times 10^{-16}$	$2.1 \pm 0.67 \times 10^{-21}$	6
Sr-1200:10h-02	1200	IEN	ND	$1.7 \pm 0.49 \times 10^{-21}$	14
Sr-1300:10h-01	1300	IEN	$6.3 \pm 4.9 \times 10^{-15}$	$2.6 \pm 2.1 \times 10^{-20}$	4

Table 4.3: Bulk and grain boundary diffusion coefficients for cesium, europium and strontium thermal diffusion. The relative error is the percent of the error in the grain boundary diffusion coefficient from fitting the grain boundary tail. ND indicates values that were not determined.

Profile	Fit	χ^2_P
Cs-900:40h-01	$C(ppm) = 130exp\left(\frac{x^2}{4{,}700nm}\right)$	2.7, p=0.61
Cs-1000:10h-01	$C(ppm) = 140exp\left(\frac{x^2}{1{,}900nm}\right)$	2.5, p=0.64
Cs-1100:10h-01	$C(ppm) = 580exp\left(\frac{x^2}{1{,}800nm}\right)$	1.9, p=0.75
Eu-900:10h-01	$C(ppm) = 1,100exp\left(\frac{x^2}{120nm}\right)$	1.9, p=0.75
Eu-1000:10h-01	$C(ppm) = 9,800exp\left(\frac{x^2}{120nm}\right)$	1.6, p=0.81
Eu-1100:10h-02	$C(ppm) = 2,400exp\left(\frac{x^2}{79nm}\right)$	2.1, p=0.71
Sr-900:40h-01	$C(ppm) = 2,300exp\left(\frac{x^2}{2{,}500nm}\right)$	2.2, p=0.69
Sr-1000:10h-01	$C(ppm) = 1,200exp\left(\frac{x^2}{4{,}300nm}\right)$	2.0, p=0.73
Sr-1100:10h-01	$C(ppm) = 750exp\left(\frac{x^2}{15{,}000nm}\right)$	2.3, p=0.68

Table 4.4: Bulk diffusion fits to FP concentration profiles from ion irradiation. χ^2_P is the indicator of goodness of fit.

Profile	Fit	χ^2_P
Cs-900:40h-01	$C(ppm) = 10exp\left(-0.00017x^{6/5}\right)$	2.5, p=0.77
Cs-1000:10h-01	$C(ppm) = 11exp\left(-0.0086x^{6/5}\right)$	3.1, p=0.68
Cs-1100:10h-01	$C(ppm) = 10exp\left(-0.0031x^{6/5}\right)$	2.2, p=0.82
Eu-900:10h-01	$C(ppm) = 7exp\left(-0.022x^{6/5}\right)$	3.4, p=0.63
Eu-1000:10h-01	$C(ppm) = 31exp\left(-0.022x^{6/5}\right)$	3.1, p=0.68
Eu-1100:10h-02	$C(ppm) = 23exp\left(-0.022x^{6/5}\right)$	2.9, p=0.71
Sr-900:40h-01	$C(ppm) = 11exp\left(-0.00039x^{6/5}\right)$	2.3, p=0.80
Sr-1000:10h-01	$C(ppm) = 3exp\left(-0.0087x^{6/5}\right)$	2.7, p=0.74
Sr-1100:10h-01	$C(ppm) = 32exp\left(-0.0024x^{6/5}\right)$	1.7, p=0.88

Table 4.5: Grain boundary diffusion fits to FP concentration profiles from ion irradiation. χ^2_P is the indicator of goodness of fit.

Profile	Temperature °C	D_B $(cm^2 s^{-1})$	$s\delta D_{GB}$ $(cm^3 s^{-1})$	Relative Error (%)
Cs-900:6h:10dpa-01	900	$1.3 \pm 1.0 \times 10^{-15}$	$1.7 \pm 1.1 \times 10^{-18}$	8
Cs-1000:6h:10dpa-01	1,000	$5.3 \pm 3.7 \times 10^{-16}$	$6.3 \pm 4.5 \times 10^{-20}$	9
Cs-1100:6h:10dpa-01	1,100	$5.2 \pm 1.0 \times 10^{-16}$	$1.1 \pm 0.2 \times 10^{-18}$	6
Eu-900:6h:10dpa-01	900	$3.4 \pm 1.8 \times 10^{-17}$	$9.5 \pm 4.6 \times 10^{-22}$	3
Eu-1000:6h:10dpa-01	1,000	$3.3 \pm 1.6 \times 10^{-17}$	$4.6 \pm 2.9 \times 10^{-22}$	6
Eu-1100:6h:10dpa-01	1,100	$2.2 \pm 1.1 \times 10^{-17}$	$1.9 \pm 1.0 \times 10^{-22}$	7
Sr-900:6h:10dpa-01	900	$7.0 \pm 4.3 \times 10^{-16}$	$7.9 \pm 6.5 \times 10^{-18}$	3
Sr-1000:6h:10dpa-01	1,000	$1.2 \pm 0.2 \times 10^{-15}$	$7.6 \pm 3.6 \times 10^{-19}$	9
Sr-1100:6h:10dpa-01	1,100	$4.1 \pm 1.6 \times 10^{-15}$	$3.4 \pm 2.3 \times 10^{-19}$	7

Table 4.6: Radiation enhanced diffusion coefficients for cesium, strontium and europium at a dose rate of 4.6×10^{-3} dpa s^{-1}

Fission Product	Temperature (°C)	Thermal Concentration (ppm)	Irradiated Concentration (ppm)
Cesium	900	2,200	200
	1,100	2,000	1,000
Europium	1,100	10,000	1,000
Strontium	900	60	2,000
	1,100	600	700

Table 4.7: The maximum FP concentration on the SiC side of the PyC/SiC interface for the thermal and radiation enhanced diffusion

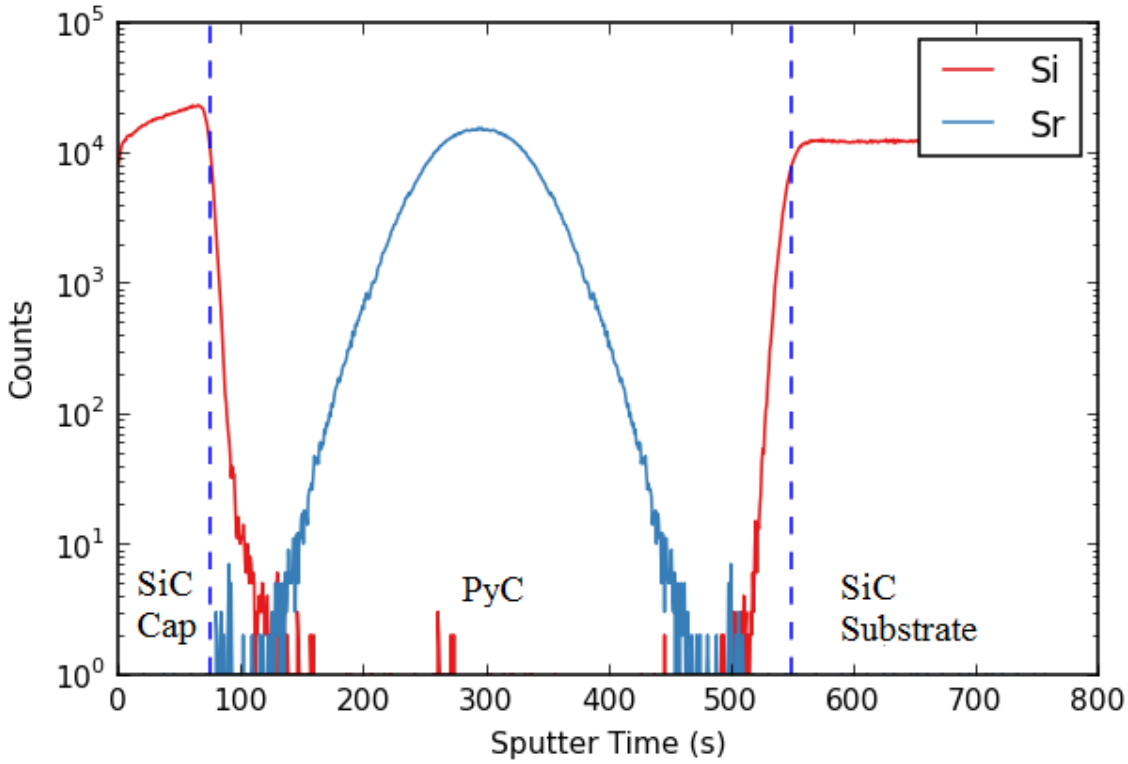

Figure 4.1: ToF-SIMS depth profile of a strontium diffusion couple in the as fabricated case. The silicon profile is used to navigate the layer structure which begins with the SiC cap at the surface, transitions to the PyC between 90s and 520s and finally to the SiC substrate after 520s. The strontium profile is completely contained within the PyC region, ensuring the integrity of the SiC substrate for diffusion analysis.

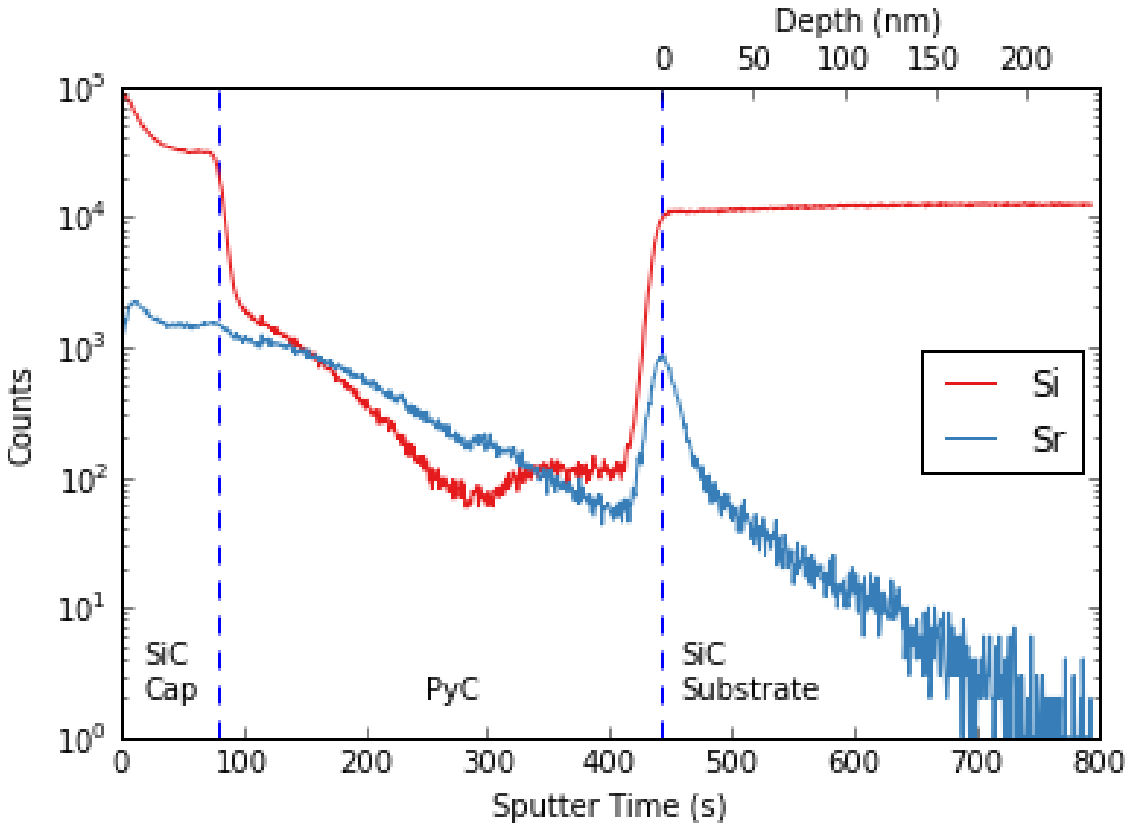

Figure 4.2: ToF-SIMS depth profile of the a $1,100°$C 10 hour strontium diffusion couple. A calibrated depth scale is also included for just the SiC substrate.

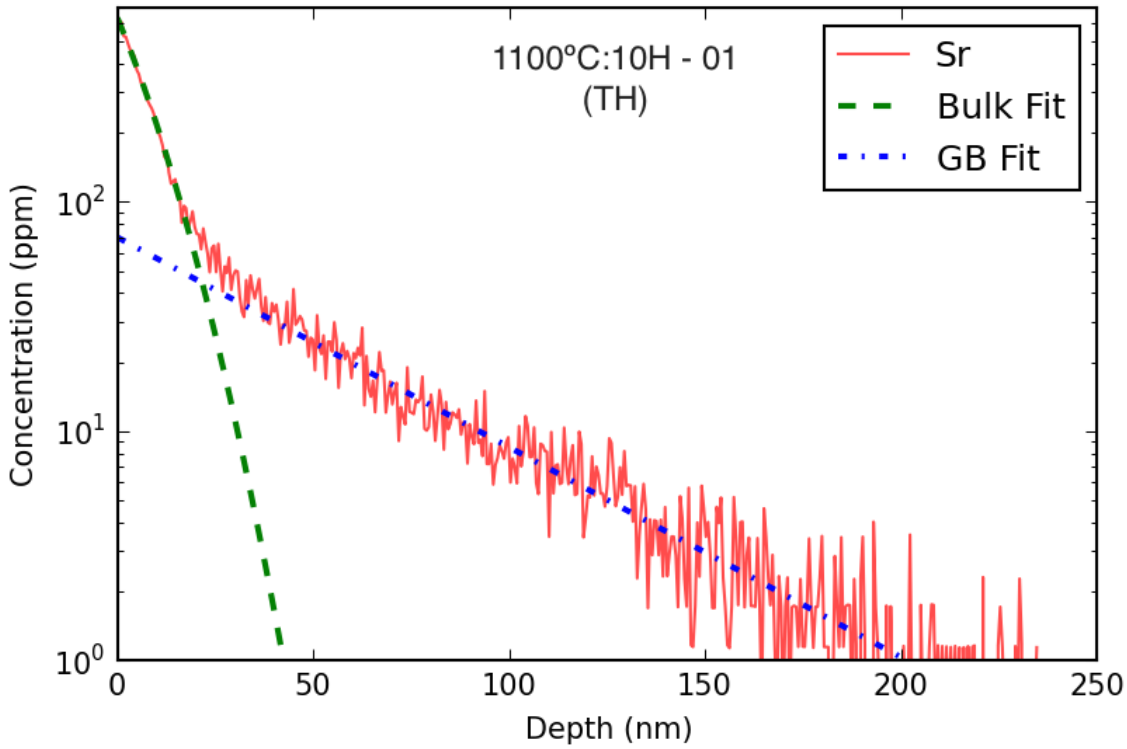

Figure 4.3: Calibrated and fitted concentration profiles for strontium at $1,100$°C for 10 hours exhibiting mixed diffusion kinetics. The steeper depth profile is due to bulk diffusion and the long diffusion tail is due to grain boundary diffusion.

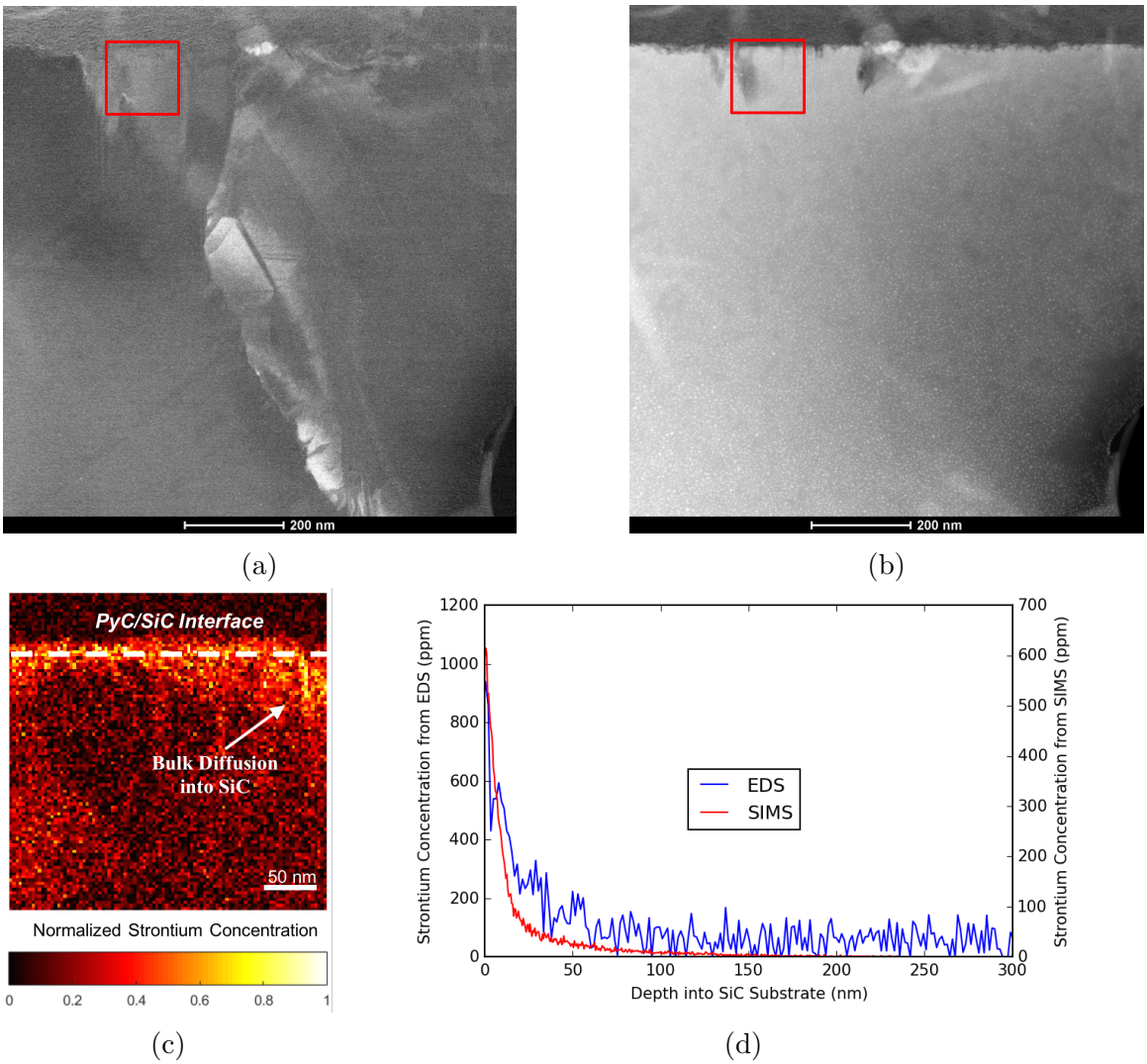

Figure 4.4: (a) Diffraction contrast image of the PyC/SiC interface and SiC substrate in the $1,100$°C:10hr-01 condition shown in Figure 4.2.
(b) HAADF image of the same region as (a).
(c) EDS map of strontium in SiC in the designated by the red box in (a) and (b). The map presents the normalized EDS intensity across the PyC/SiC interface and in the SiC substrate. An EDS map of the silicon concentration was used to identify the PyC/SiC Interface indicated by the dashed white line.
(d) The corresponding 1D depth profile below the PyC/SiC interface in (c) plotted in blue. The equivalant SIMS profile from Figure 4.3 is shown in red for comparison.

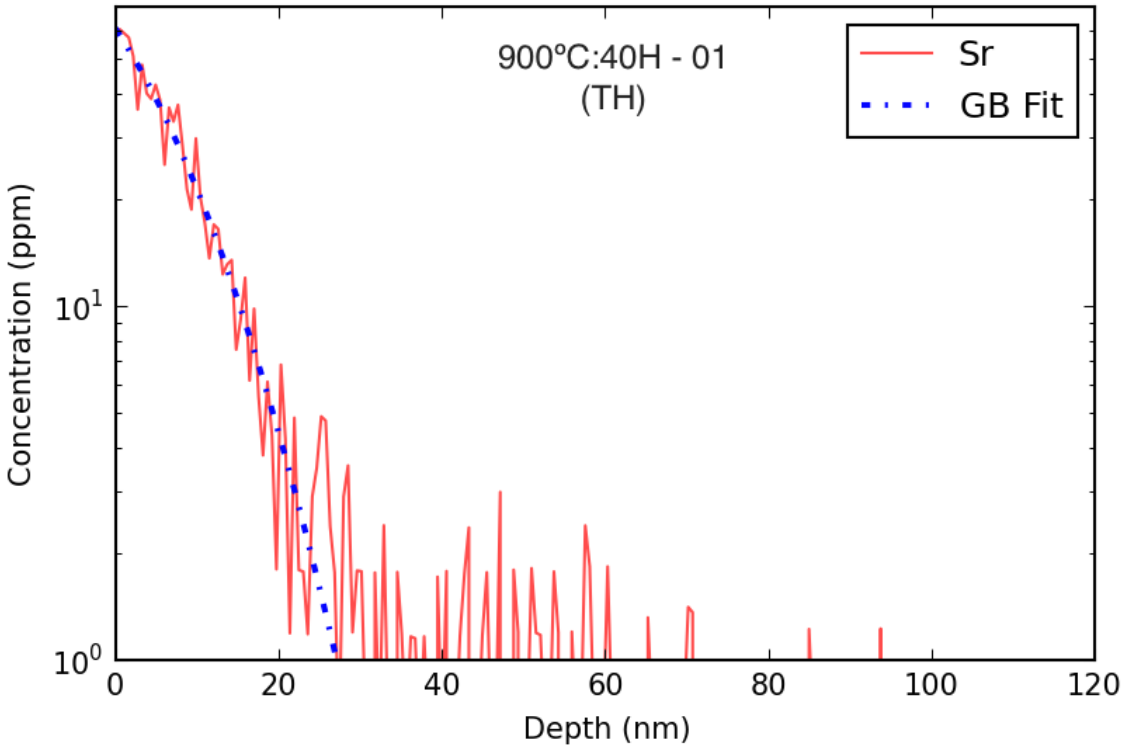

Figure 4.5: Calibrated and fitted concentration profiles for strontium at 900°C for 40 hours exhibiting grain boundary dominant diffusion kinetics.

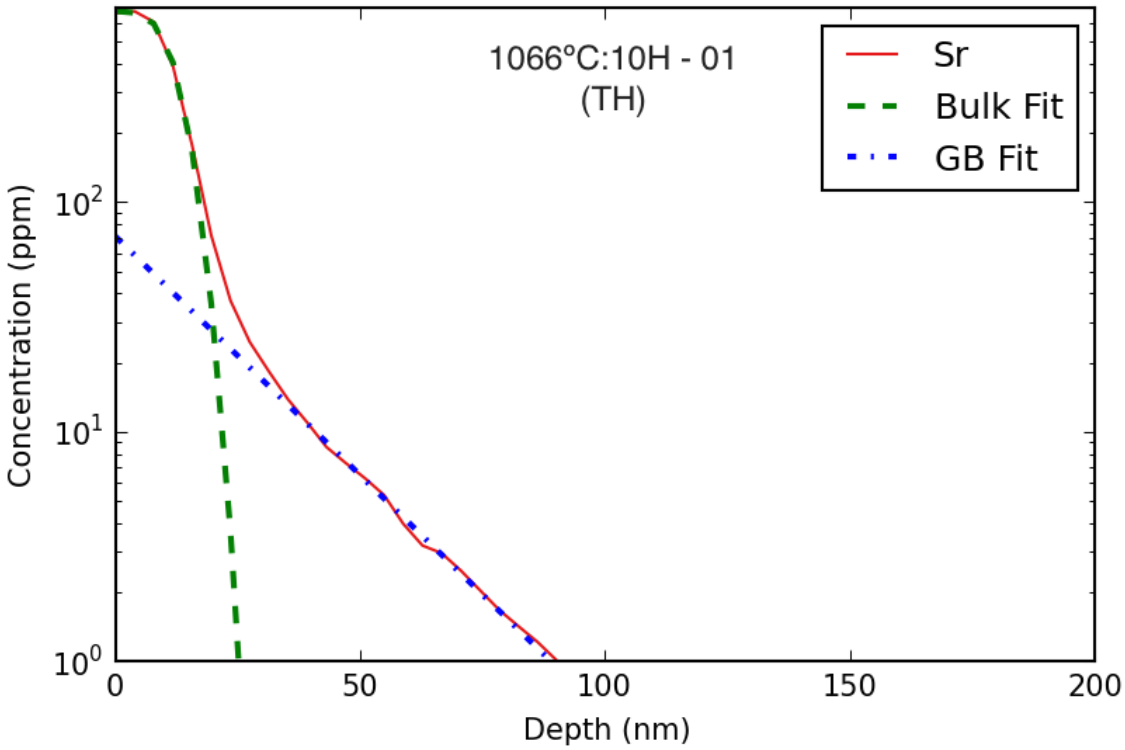

Figure 4.6: Calibrated and fitted concentration profiles for strontium at $1,066$°C for 10 hours exhibiting mixed diffusion kinetics. The steeper depth profile is due to bulk diffusion and the long diffusion tail is due to grain boundary diffusion.

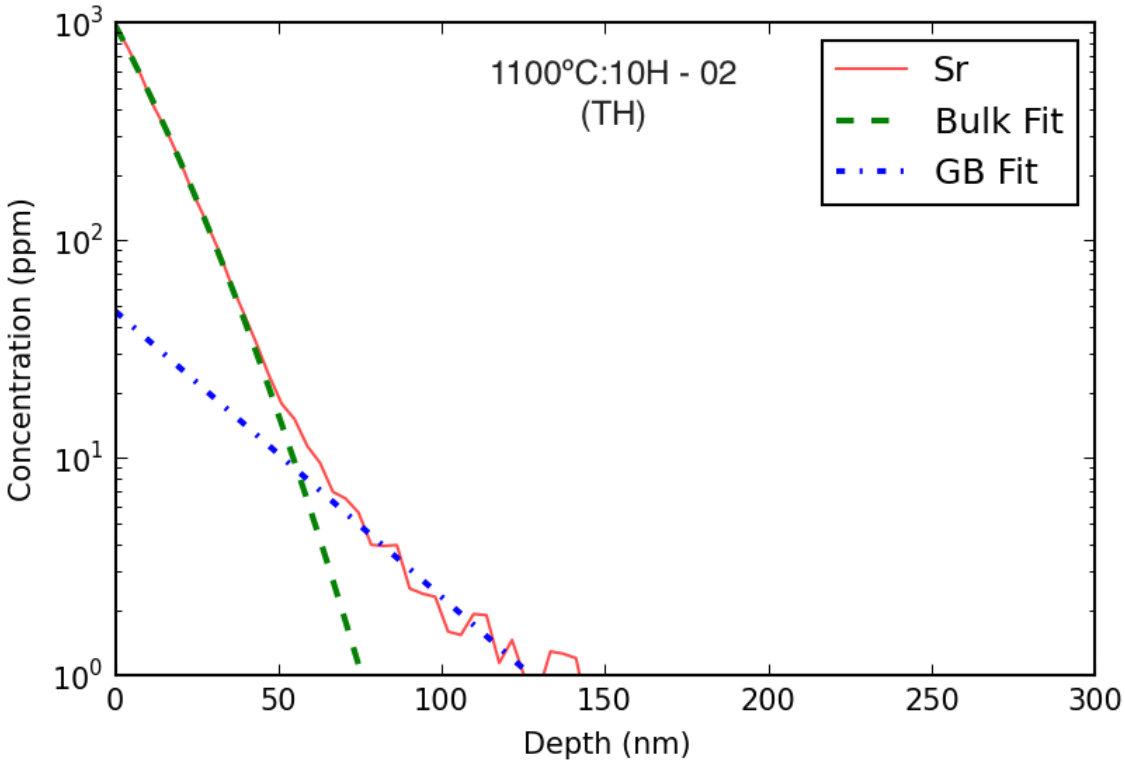

Figure 4.7: Calibrated and fitted concentration profiles for strontium at $1,100$°C for 10 hours exhibiting mixed diffusion kinetics. The steeper depth profile is due to bulk diffusion and the long diffusion tail is due to grain boundary diffusion.

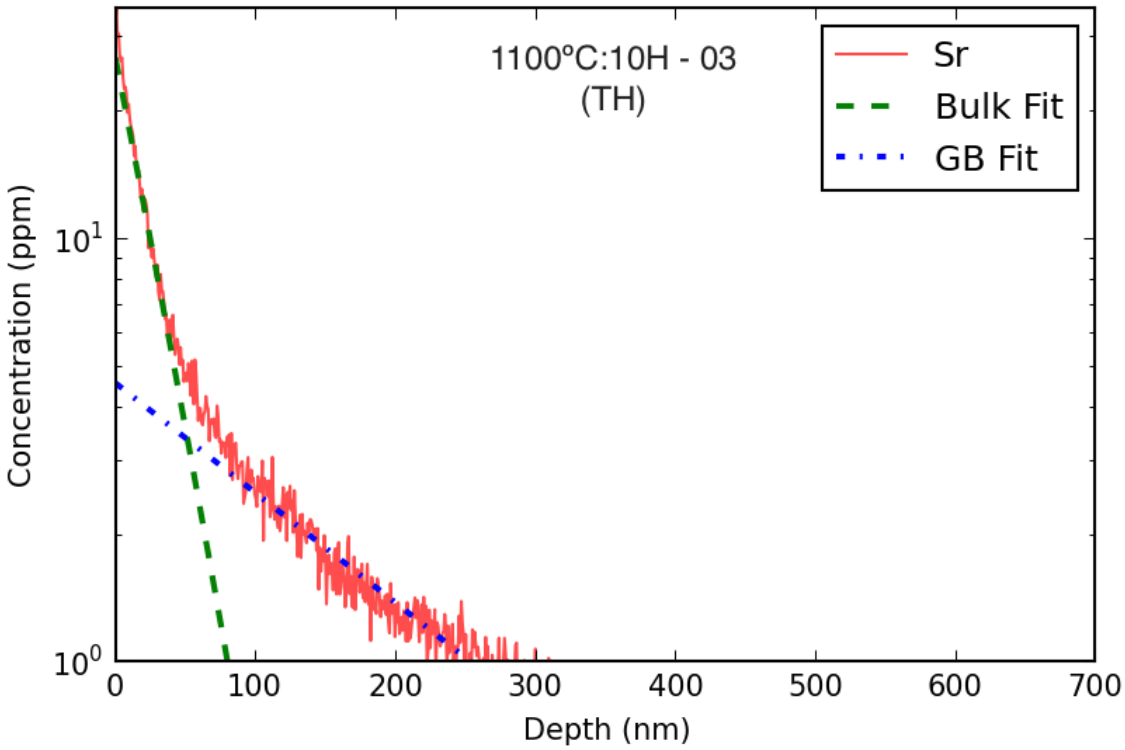

Figure 4.8: Calibrated and fitted concentration profiles for strontium at $1,100$°C for 10 hours exhibiting mixed diffusion kinetics. The steeper depth profile is due to bulk diffusion and the long diffusion tail is due to grain boundary diffusion.

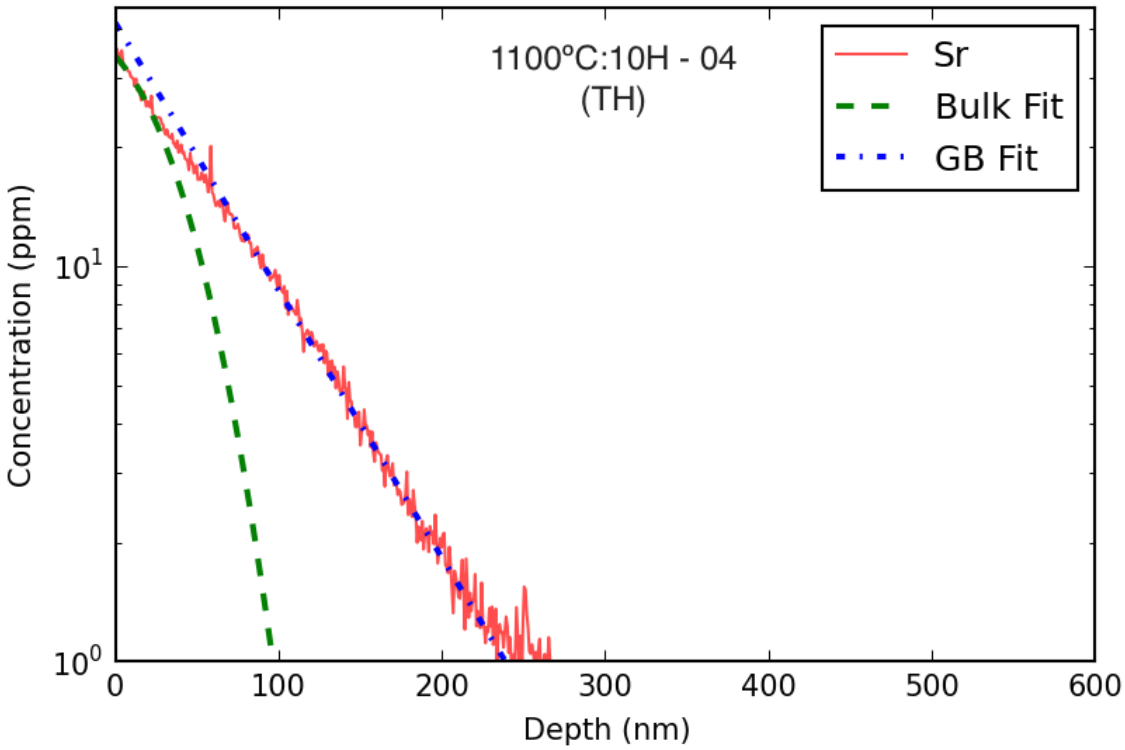

Figure 4.9: Calibrated and fitted concentration profiles for strontium at $1,100$°C for 10 hours exhibiting mixed diffusion kinetics. The steeper depth profile is due to bulk diffusion and the long diffusion tail is due to grain boundary diffusion.

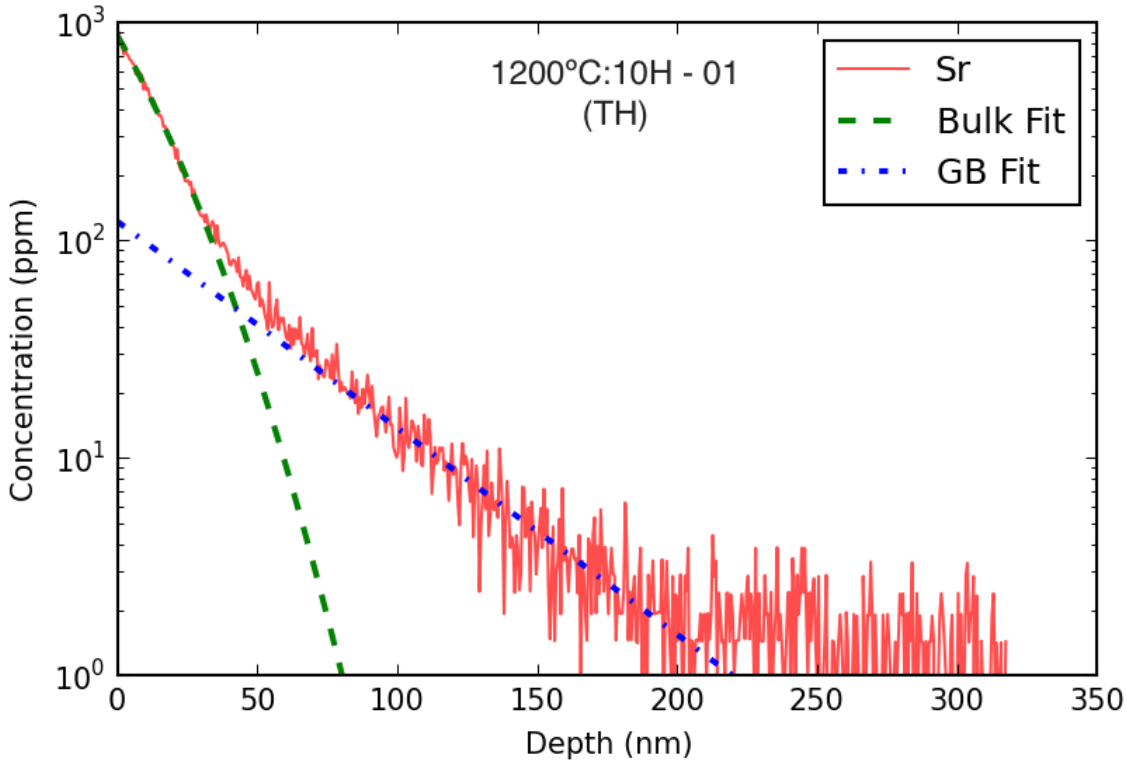

Figure 4.10: Calibrated and fitted concentration profiles for strontium at $1,200°C$ for 10 hours exhibiting mixed diffusion kinetics. The steeper depth profile is due to bulk diffusion and the long diffusion tail is due to grain boundary diffusion.

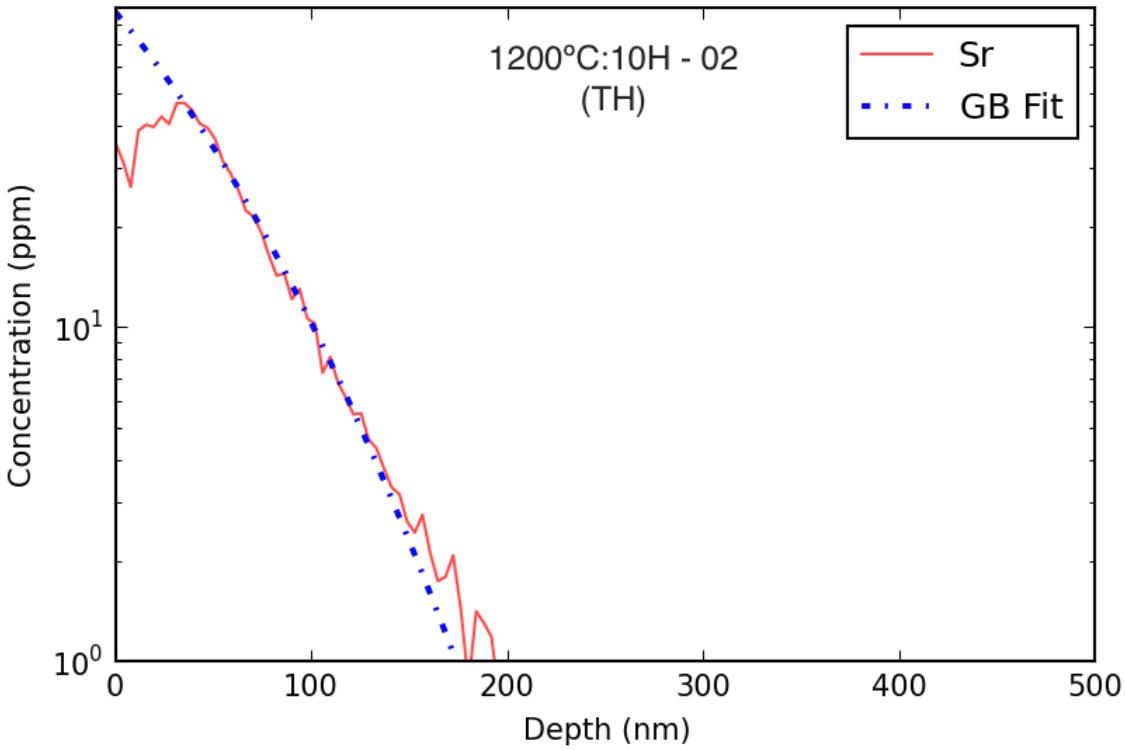

Figure 4.11: Calibrated and fitted concentration profiles for strontium at $1,200°C$ for 10 hours. Only the grain boundary diffusion coefficient could be extracted using the formalism for mixed diffusion kinetics

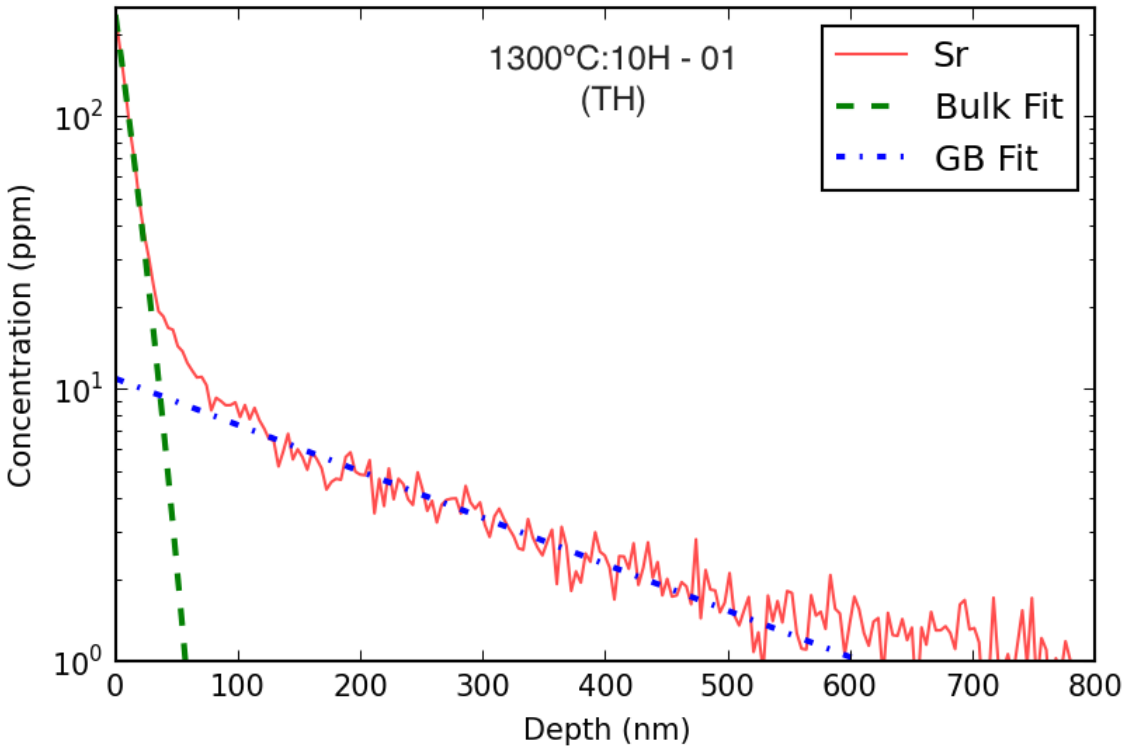

Figure 4.12: Calibrated and fitted concentration profiles for strontium at $1,300$°C for 10 hours exhibiting mixed diffusion kinetics. The steeper depth profile is due to bulk diffusion and the long diffusion tail is due to grain boundary diffusion.

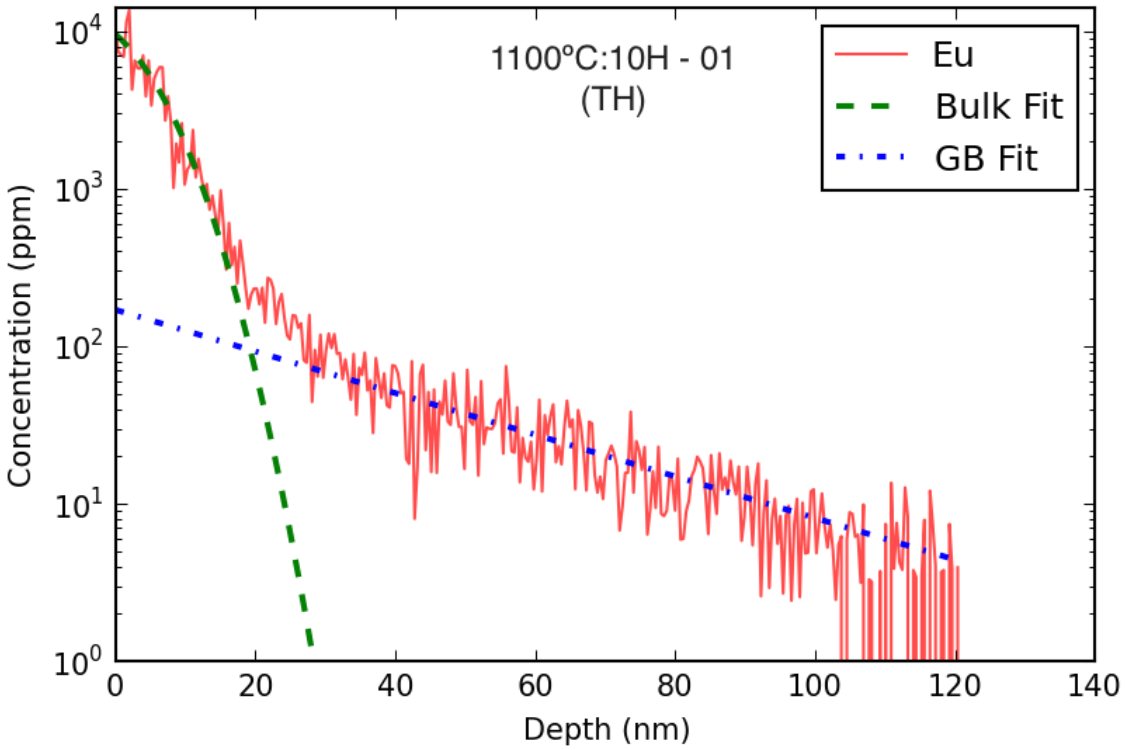

Figure 4.13: Calibrated and fitted concentration profiles for europium at $1,100$°C for 10 hours exhibiting mixed diffusion kinetics. The steeper depth profile is due to bulk diffusion and the long diffusion tail is due to grain boundary diffusion.

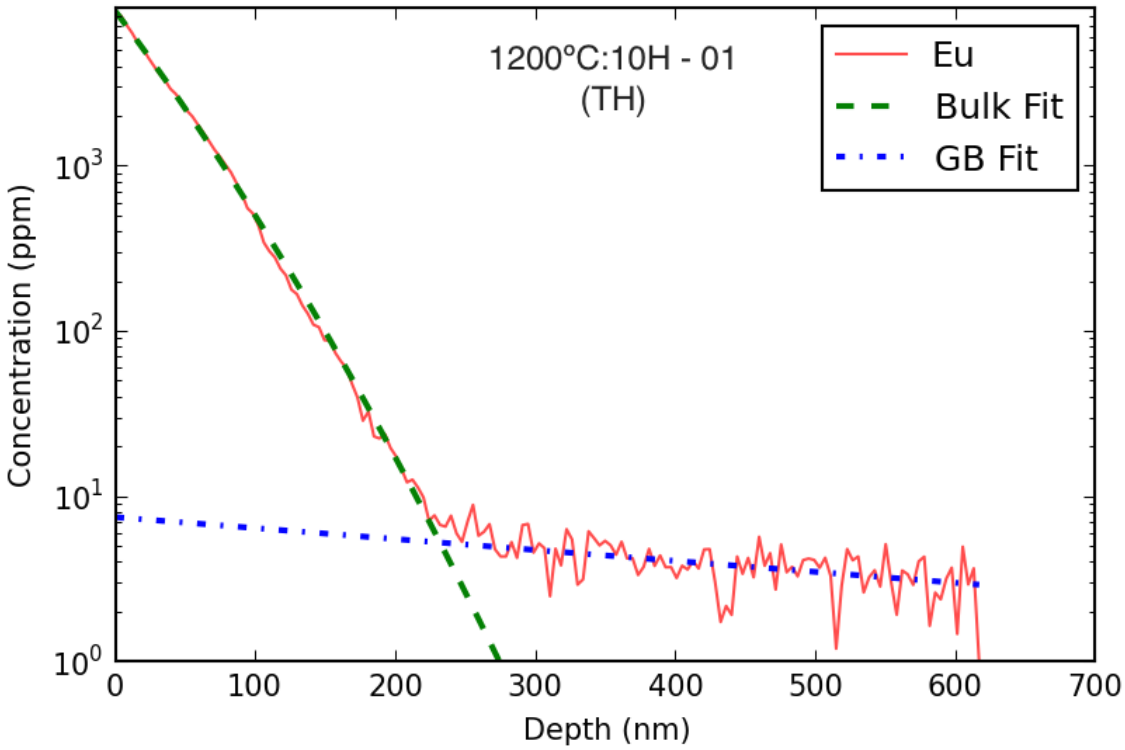

Figure 4.14: Calibrated and fitted concentration profiles for europium at $1,200$°C for 10 hours exhibiting mixed diffusion kinetics. The steeper depth profile is due to bulk diffusion and the long diffusion tail is due to grain boundary diffusion.

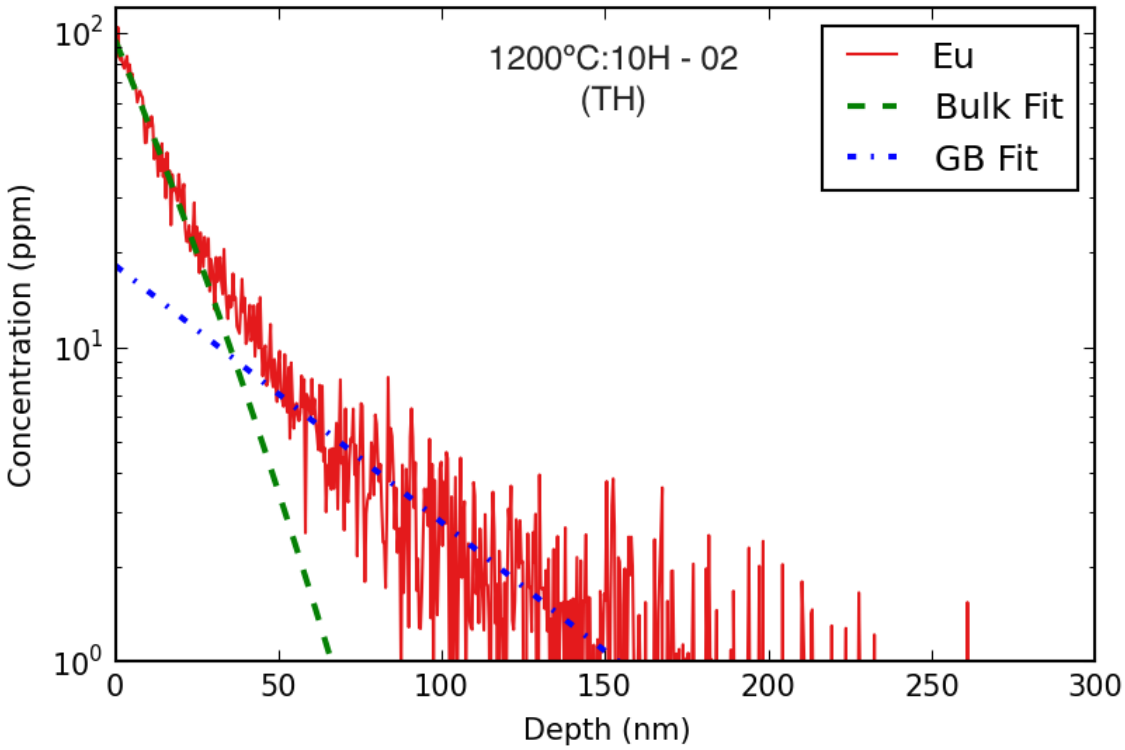

Figure 4.15: Calibrated and fitted concentration profiles for europium at $1,200$°C for 10 hours exhibiting mixed diffusion kinetics. The steeper depth profile is due to bulk diffusion and the long diffusion tail is due to grain boundary diffusion.

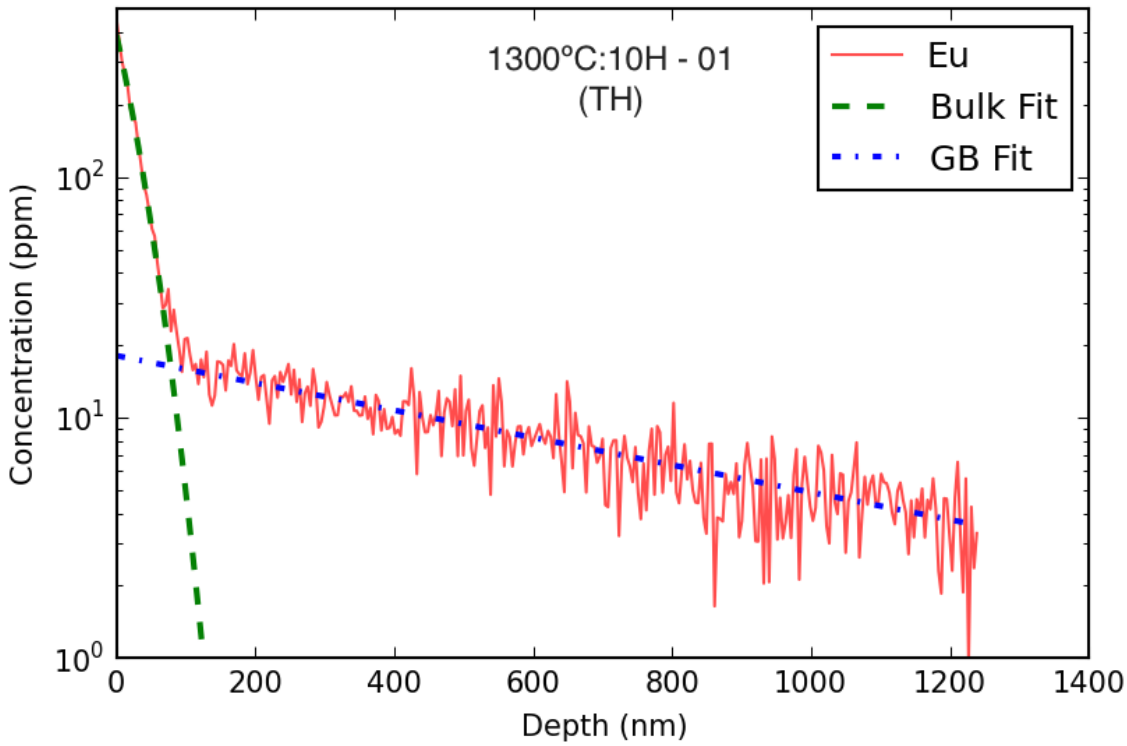

Figure 4.16: Calibrated and fitted concentration profiles for europium at $1,300$°C for 10 hours exhibiting mixed diffusion kinetics. The steeper depth profile is due to bulk diffusion and the long diffusion tail is due to grain boundary diffusion.

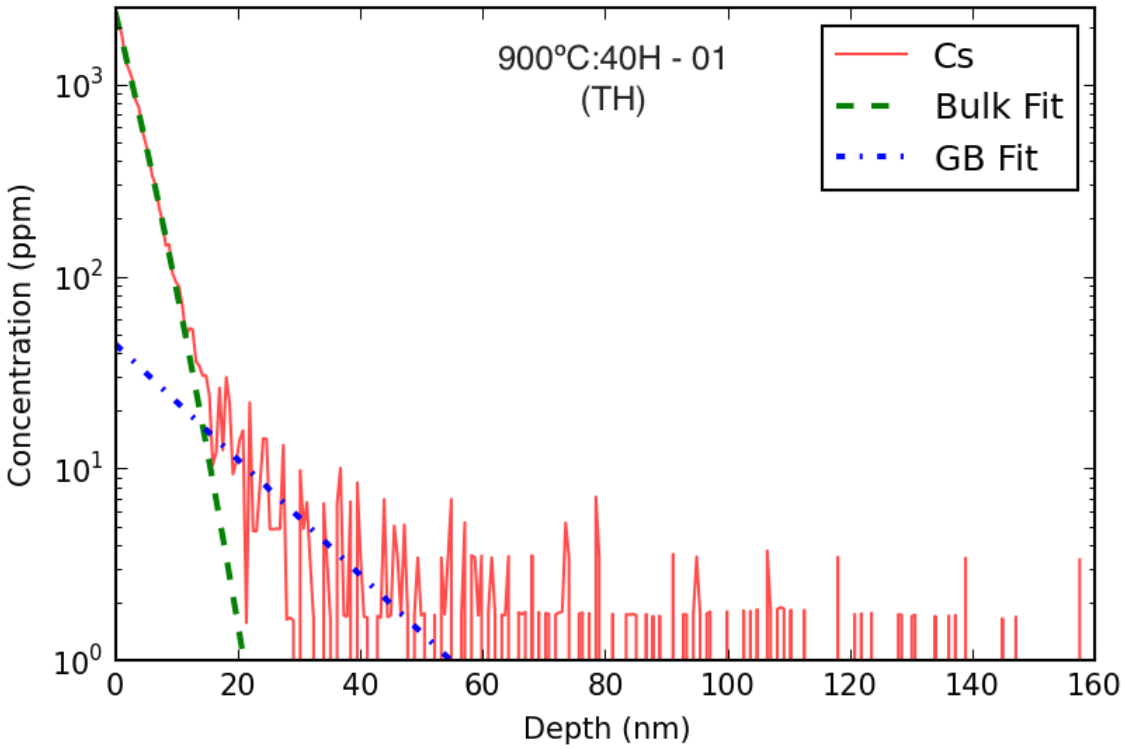

Figure 4.17: Calibrated and fitted concentration profiles for cesium at 900°C for 10 hours exhibiting mixed diffusion kinetics. The steeper depth profile is due to bulk diffusion and the long diffusion tail is due to grain boundary diffusion.

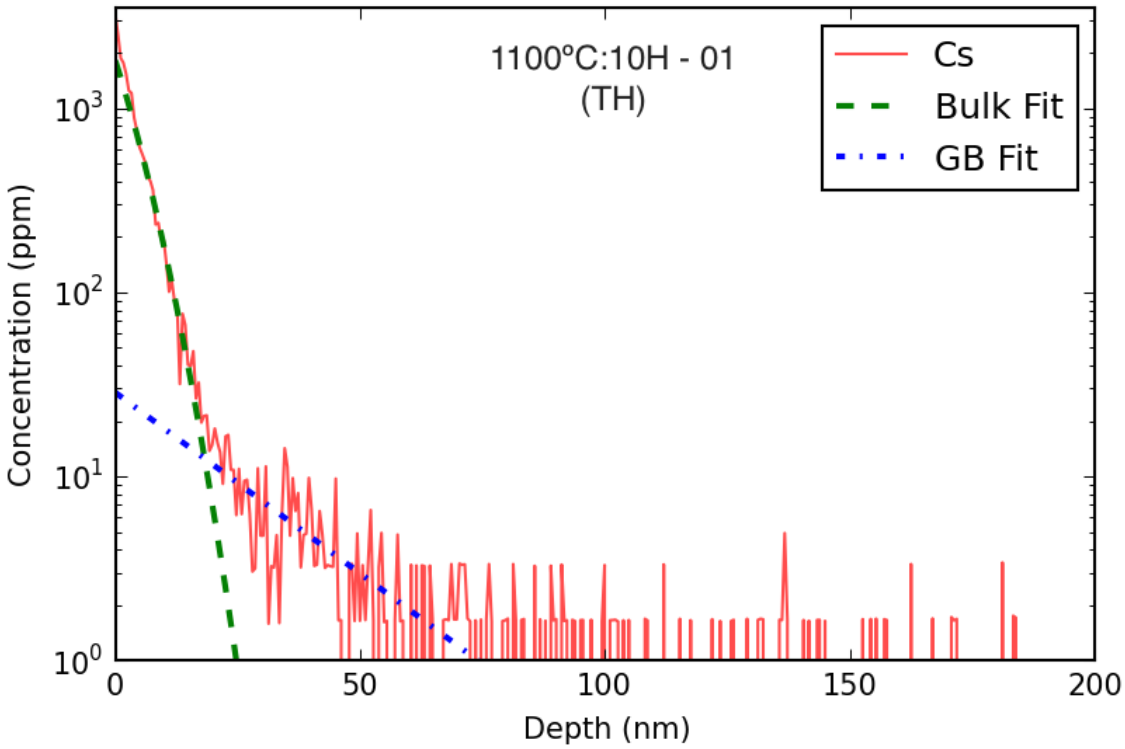

Figure 4.18: Calibrated and fitted concentration profiles for cesium at $1,100$°C for 10 hours exhibiting mixed diffusion kinetics. The steeper depth profile is due to bulk diffusion and the long diffusion tail is due to grain boundary diffusion.

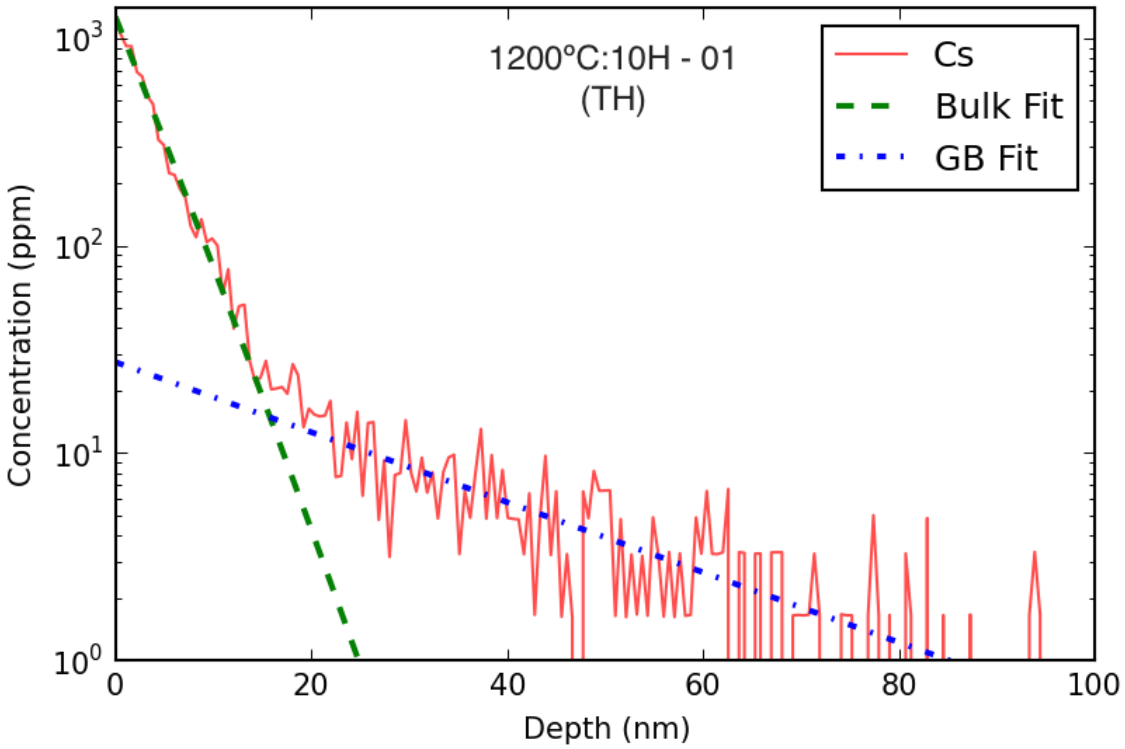

Figure 4.19: Calibrated and fitted concentration profiles for cesium at $1,200$°C for 10 hours exhibiting mixed diffusion kinetics. The steeper depth profile is due to bulk diffusion and the long diffusion tail is due to grain boundary diffusion.

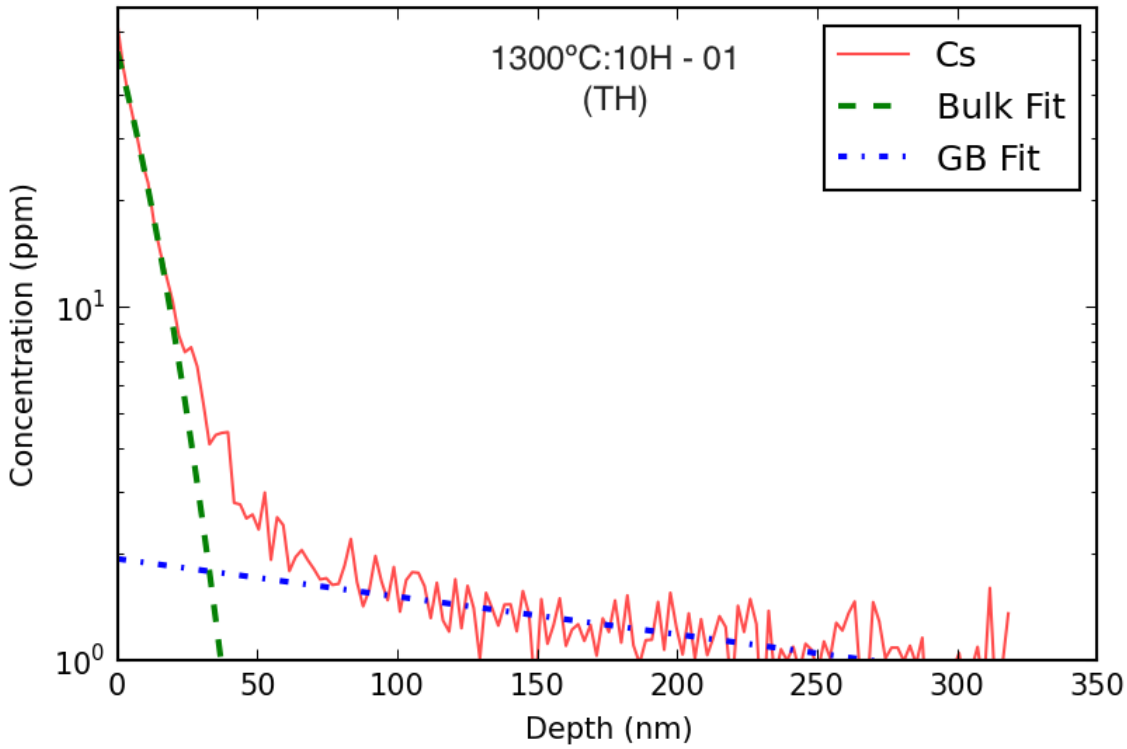

Figure 4.20: Calibrated and fitted concentration profiles for cesium at $1,300$°C for 10 hours exhibiting mixed diffusion kinetics. The steeper depth profile is due to bulk diffusion and the long diffusion tail is due to grain boundary diffusion.

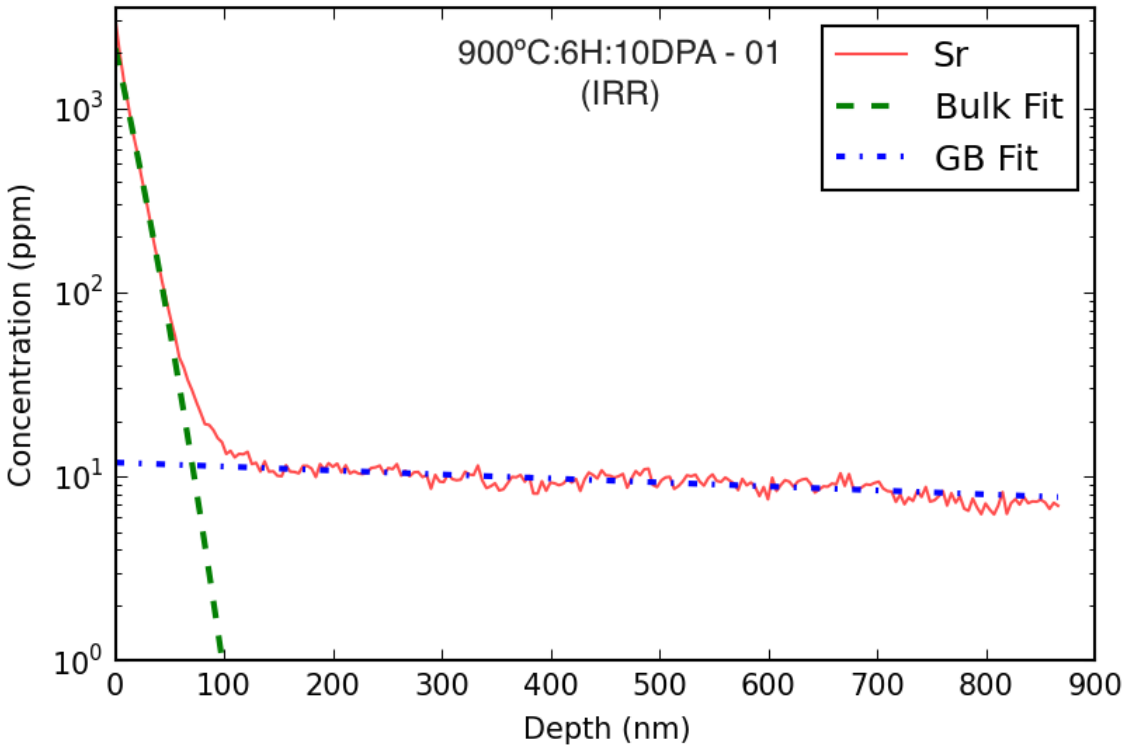

Figure 4.21: Calibrated and fitted concentration profiles for strontium at 900°C irradiated at $4.6 \times 10^{-4} dpa\ s^{-1}$ to 10 dpa over 6 hours. The steeper depth profile is due to bulk diffusion and the long diffusion tail is due to grain boundary diffusion.

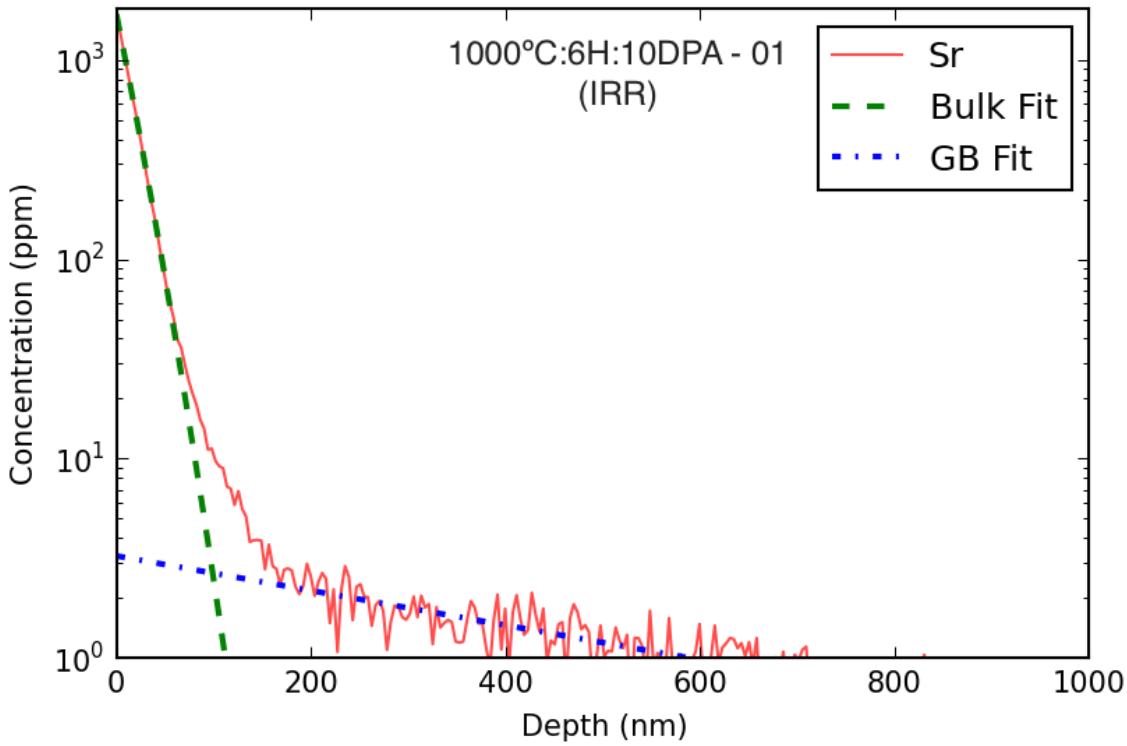

Figure 4.22: Calibrated and fitted concentration profiles for strontium at $1,000$°C irradiated at $4.6 \times 10^{-4} dpa\ s^{-1}$ to 10 dpa over 6 hours. The steeper depth profile is due to bulk diffusion and the long diffusion tail is due to grain boundary diffusion.

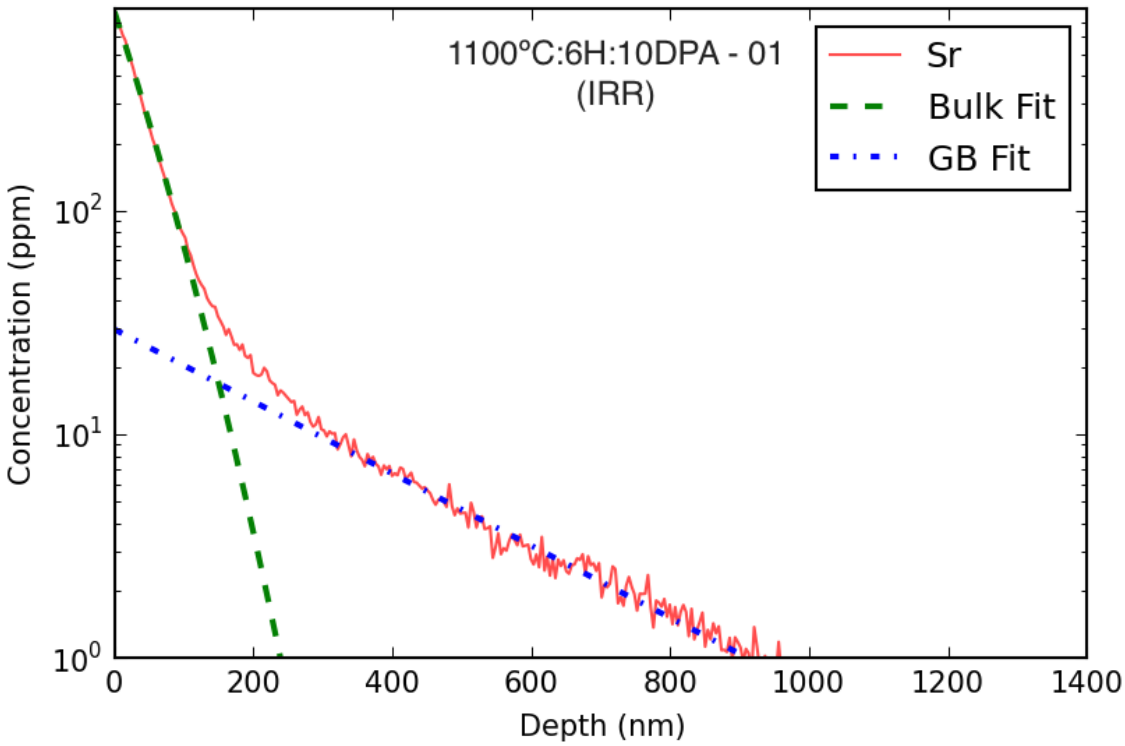

Figure 4.23: Calibrated and fitted concentration profiles for strontium at $1,100°C$ irradiated at $4.6 \times 10^{-4} dpa\ s^{-1}$ to 10 dpa over 6 hours. The steeper depth profile is due to bulk diffusion and the long diffusion tail is due to grain boundary diffusion.

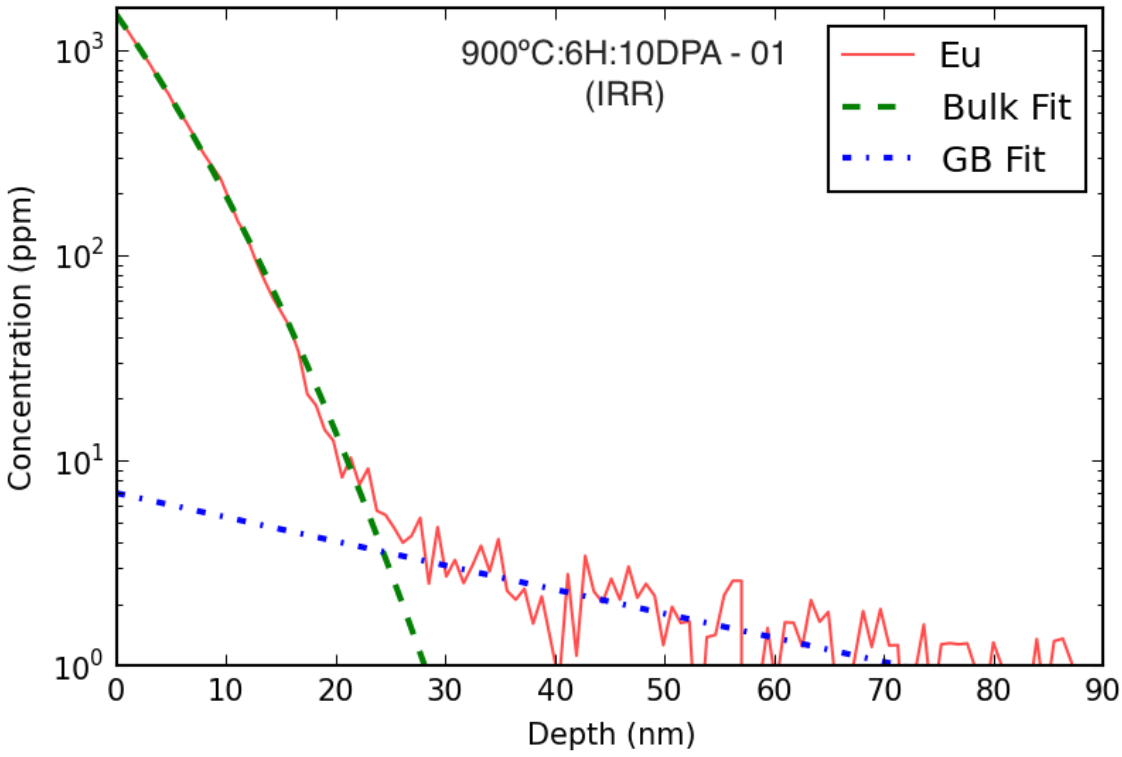

Figure 4.24: Calibrated and fitted concentration profiles for europium at 900°C irradiated at $4.6 \times 10^{-4} dpa\ s^{-1}$ to 10 dpa over 6 hours. The steeper depth profile is due to bulk diffusion and the long diffusion tail is due to grain boundary diffusion.

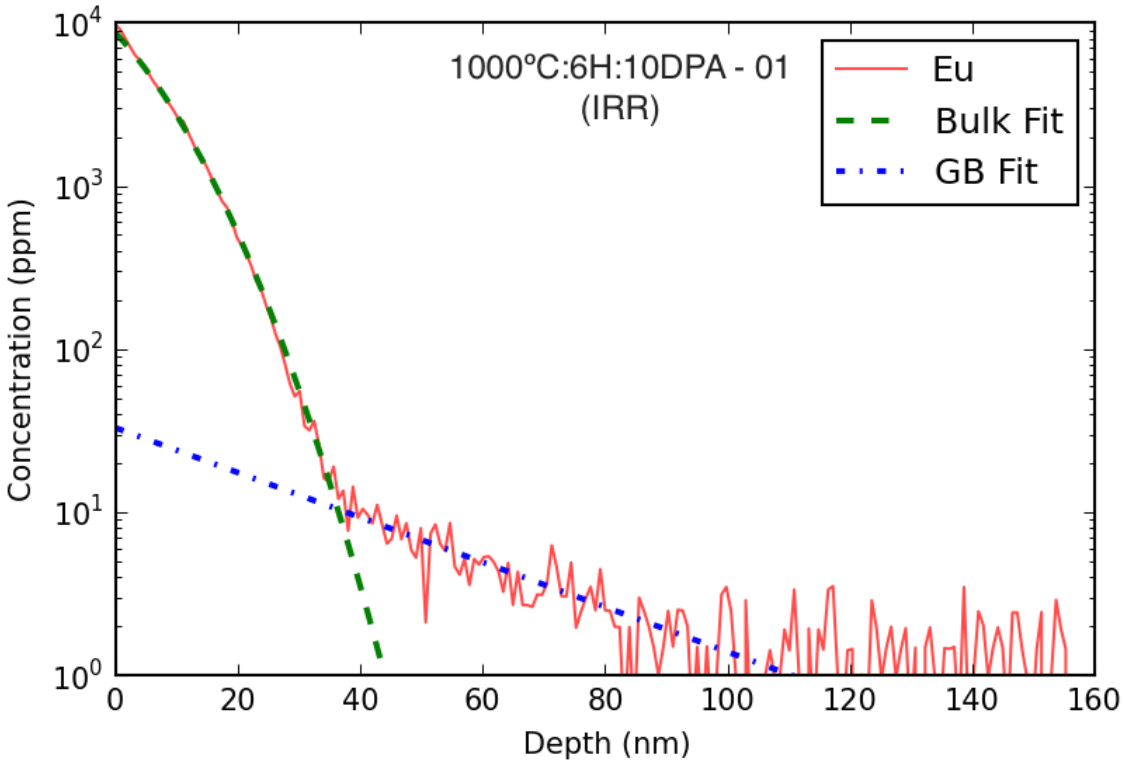

Figure 4.25: Calibrated and fitted concentration profiles for europium at $1,000$°C irradiated at $4.6 \times 10^{-4} dpa\ s^{-1}$ to 10 dpa over 6 hours. The steeper depth profile is due to bulk diffusion and the long diffusion tail is due to grain boundary diffusion.

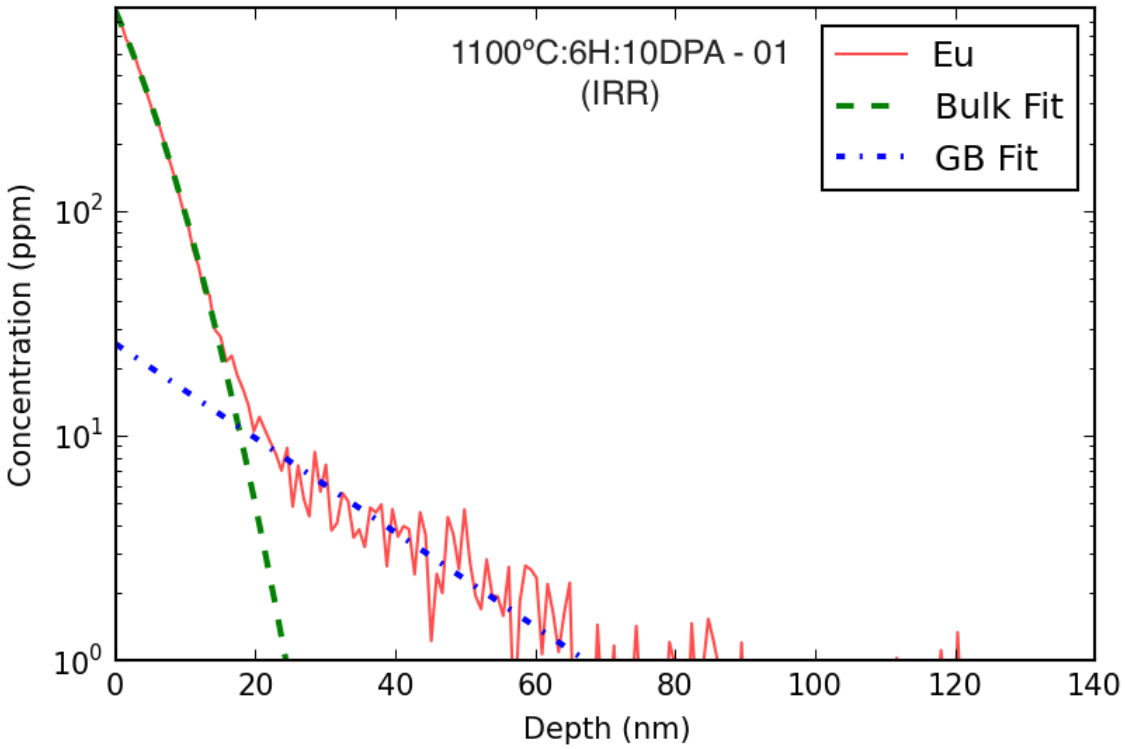

Figure 4.26: Calibrated and fitted concentration profiles for europium at $1,100°C$ irradiated at $4.6 \times 10^{-4} dpa\ s^{-1}$ to 10 dpa over 6 hours. The steeper depth profile is due to bulk diffusion and the long diffusion tail is due to grain boundary diffusion.

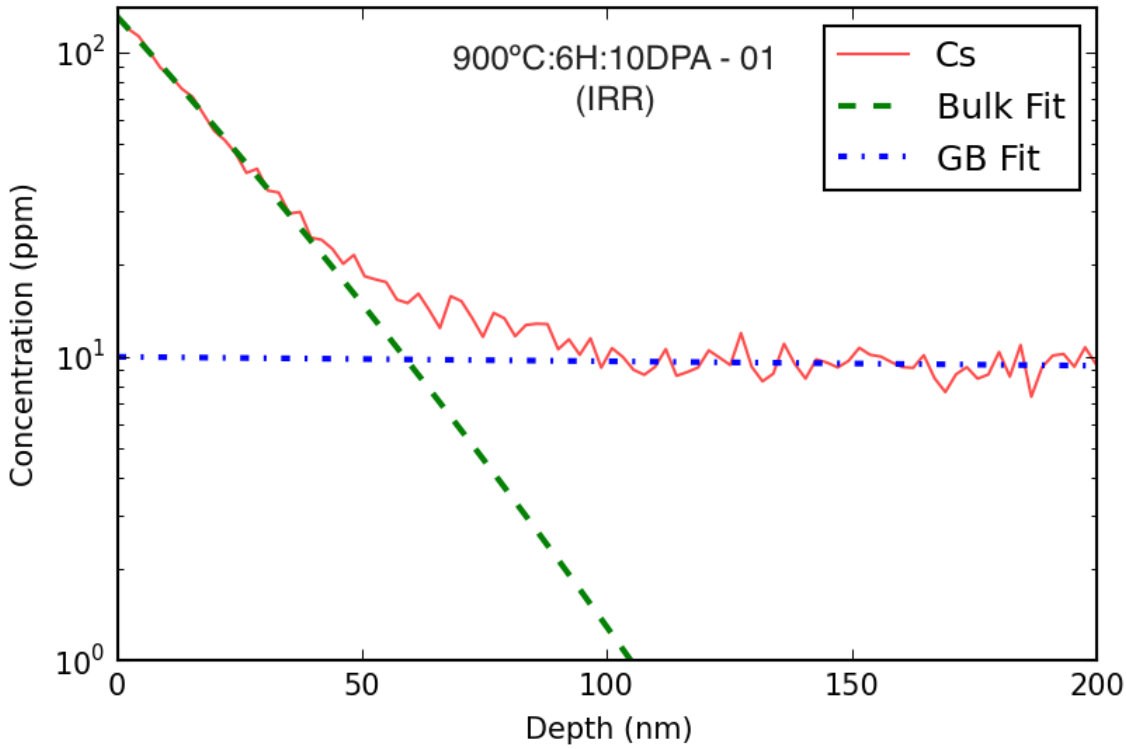

Figure 4.27: Calibrated and fitted concentration profiles for cesium at 900°C irradiated at $4.6 \times 10^{-4} dpa\ s^{-1}$ to 10 dpa over 6 hours. The steeper depth profile is due to bulk diffusion and the long diffusion tail is due to grain boundary diffusion.

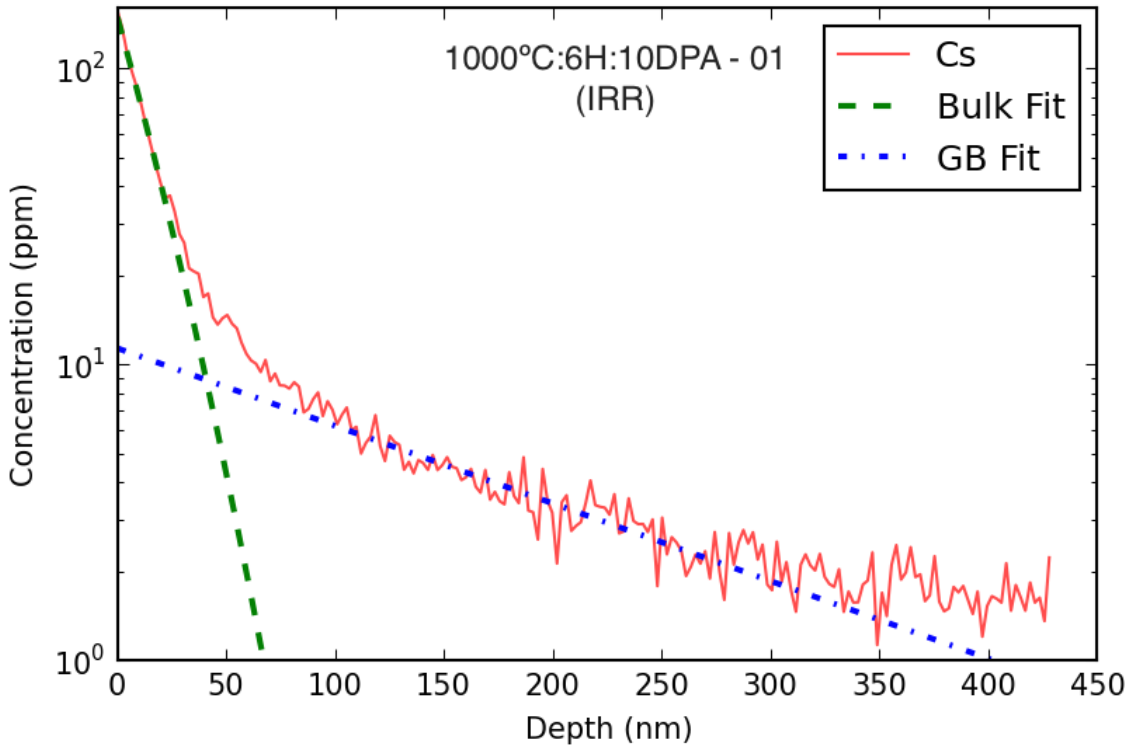

Figure 4.28: Calibrated and fitted concentration profiles for cesium at $1,000°C$ irradiated at $4.6 \times 10^{-4} dpa\ s^{-1}$ to 10 dpa over 6 hours. The steeper depth profile is due to bulk diffusion and the long diffusion tail is due to grain boundary diffusion.

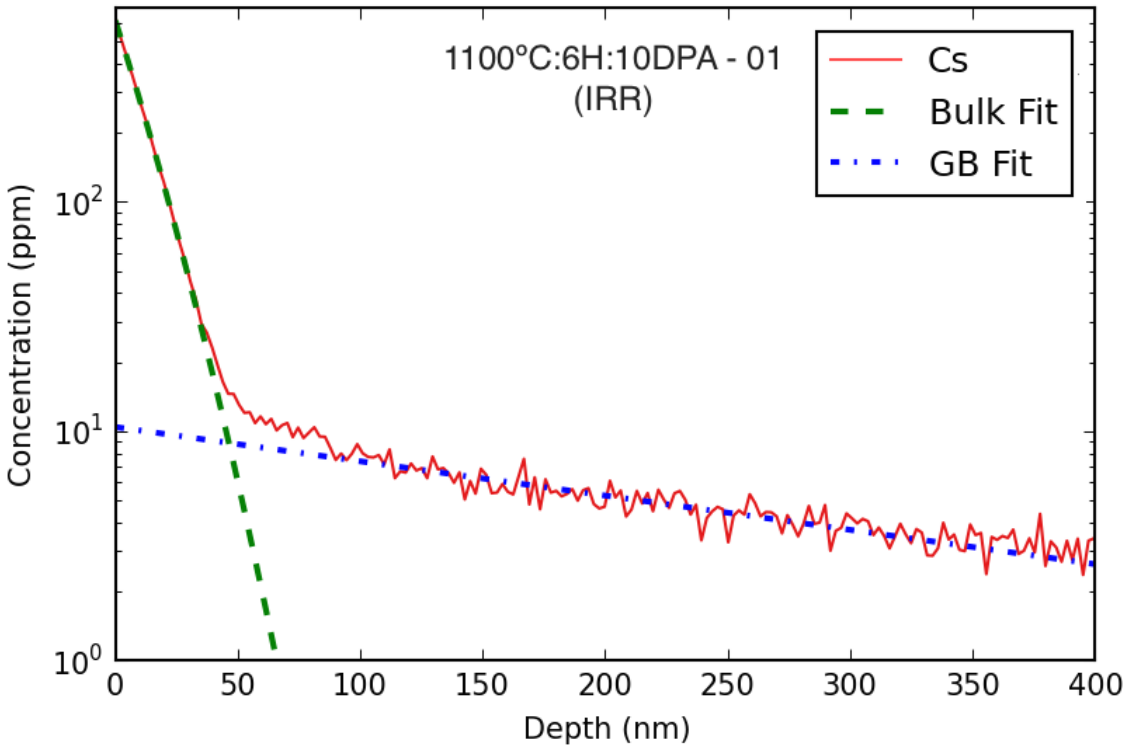

Figure 4.29: Calibrated and fitted concentration profiles for cesium at $1,100°C$ irradiated at $4.6 \times 10^{-4} dpa\ s^{-1}$ to 10 dpa over 6 hours. The steeper depth profile is due to bulk diffusion and the long diffusion tail is due to grain boundary diffusion.

CHAPTER V

Discussion

This chapter will evaluate the performance of the diffusion couple design and then determine the diffusion coefficients from the concentration profiles presented in Chapter IV, including the activation energies and pre-factors for both bulk and grain boundary diffusion in the thermally annealed condition. It will then compare these values to determine which is dominant for each fission product. This process will be repeated for the ion-irradiated condition. A point defect model will be used to determine the atomistics of diffusion of the FPs on the silicon and carbon sub-latices. The diffusion coefficients, activation energies and pre-factors will then be compared with literature data to determine their impact on fission product release modeling.

5.1 Diffusion Couple Performance

The properties of SiC are highly dependent on the fabrication process. This is true for thermo-mechanical [13] and chemical properties as evidenced by the vastly different diffusion fluxes of strontium through the SiC cap and into the SiC substrate as shown in Figure 4.2. The PECVD SiC produced here is initially amorphous and then slowly crystallizes upon heating. While the initial film may be deposited at theoretical density, the crystallization and hydrogen desorption result in a film with sub-theoretical density [90]. This reduces the efficacy of the SiC cap and

limited the temperature range of this study. Still, this study has been successful in containing enough of the implanted FP to measure the diffusion of cesium, europium and strontium between 900°C and 1,300°C and the radiation enhanced diffusion of these FPs between 900°C and 1,100°C.

Friedland et. al. attempted to study cesium and strontium diffusion by direct ion implantation into SiC [91–93]. They ion implanted FPs into polycrystaline 3C-SiC and single crystal 6H-SiC, annealed the samples at high temperature, and measured concentration using SIMS. For both FPs, redistribution of the FP was observed when the damaged SiC recrystalized, but not into the undamaged SiC at temperatures up to 1,500°C. In this study, cesium and strontium diffusion was observed as low as 900°C, but the FP was introduced into the SiC a fundamentally different manner. This could be due to the introduction of excessive radiation damage into the SiC from direct ion implantation, creating trapping sites for the FPs, or due to the lack of the PyC/SiC interface. The multi-layered diffusion couple also exhibits some trapping of FPs at the PyC/SiC interface as observed by the build up of strontium at the PyC/SiC interface seen in the EDS map in Figure 4.4c. If the radiation damage was solely responsible for the difference in diffusion behavior, then there would still be some observation of diffusion in the direct ion implantations, albeit greatly diminished in comparison to the measurements made in this study. It is likely that the thermodynamics across the PyC/SiC interface greatly increase the amount of FPs that can diffuse into the SiC vs. the FP precipitate/SiC interlace.

5.1.1 Reproducibility

The reproducibility of diffusion measurements was investigated by producing two separate 1,100°C:10hr strontium diffusion couples and taking two SIMS depth profiles from each diffusion couple. Bulk diffusion coefficients varied by a factor of 3, while grain boundary diffusion coefficients varied by a factor of 5, which is far less than the

orders of magnitude variability for the diffusion of FPs in SiC in the literature [1,93]. The strontium concentration at which bulk and grain boundary diffusion occurred at varied by nearly 2 orders of magnitude, but this had little impact on the diffusion coefficients, which are related to the slopes of the concentration profiles.

There are three major sources of variability in this study. The first is the variability in the quality of the SiC cap on each individual sample. The SiC cap ensures that the FP has enough residence time at the PyC/SiC interface to diffuse into the SiC. The PECVD process deposits a relatively uniform layer, but the dynamics of recrystallization and hydrogen desorption during annealing can greatly affect the final SiC cap density. This creates sample to sample variation, and variation within each sample, which were not characterized. An annealing pre-treatment at lower temperatures might ensure a more uniform high density SiC cap, reducing some of this variation.

The second source is the PyC/SiC interface. The EDS map of strontium in the 1,100°C:10hr condition presented in Figure 4.4c shows a localized nodule of strontium on the right side of the image. This preferential segregation at one portion of the PyC/SiC interface could be due to the local orientation mismatch between the PyC and SiC, the nature of the bonding at that location, or stress concentration due to the surrounding interface character.

The third source is the diffusion into SiC itself. Bulk diffusion should be relatively homogenous within SiC. Grain boundaries are heterogeneously located and differ in character. The grain boundary character is likely to play a role in both the segregation thermodynamics and the diffusion kinetics, controlling the concentration and the rate at which FPs diffuse along the boundary. This heterogeneity will create a variability in the measured diffusion coefficient depending on the distribution of grain boundaries that the SIMS profile averages over.

5.2 Fast Diffusion Paths

Bulk and grain boundary diffusion are assumed to be the only two active mechanisms in poly-crystalline 3C-SiC that is grown by CVD and is at theoretical density with minimum impurities such as the SiC used in this study. The Fisher model provides a method to analyze diffusion by two competing mechanisms, one that is isolated to small thin slabs and is relatively fast and the other that takes up the rest of the material but is relatively slow. The slow diffusion mechanism has been shown to be bulk diffusion via TEM in Figure 4.4.

Historically the fast mechanism has been assumed to be grain boundary diffusion and has been verified in a variety of model systems by studying diffusion in single crystal and poly-crystalline samples [49, 54, 56, 94–96]. While other features such as stacking faults and dislocations could also be fast diffusion paths, the general consensus is that the effects of fast pipe diffusion are observed as an enhancement of bulk diffusion when grain boundary diffusion is a competing mechanism as is the case in all poly-crystalline material [55, 97, 98].

Vapor phase diffusion via inter-connected porosity is another probable mechanism. The diffraction contrast and HAADF images shown in Figure 4.4a and Figure 4.4b show a notable lack of porosity and no indication that strontium has diffused via any additional paths. Theoretical density SiC should have no porosity, let alone the inter-connected network of porosity that is necessary for vapor phase diffusion. Honorato et al. investigated this mechanism for silver diffusion in SiC by tailoring the density of SiC coatings for their spherical diffusion couples [67]. They found that silver did not segregate to the porosity, but rather to grain boundaries at annealing temperatures of $1,500°C$.

It was also not possible to detect strontium along the grain boundaries visible in Figure 4.4a, but this could be due to the limited sensitivity of EDS or a grain boundary character dependence on diffusion. Decreasing temperature would increase

the segregation to grain boundaries increasing the local concentration but would also limit the diffusion kinetics across the PyC/SiC interface, limiting the peak concentrations available to the grain boundaries. These competing effects must be better evaluated to identify the ideal set of conditions for confirmation of grain boundary diffusion.

TEM observation of irradiated TRISO particles by Rooyen et al. have shown significant segregation to grain boundaries of silver, palladium, cesium and cadmium [9, 99, 100]. These FPs represent a wide distribution of chemical behavior and size effects, including cesium which is investigated in this study. The lack of alternative mechanisms, the extensive literature on diffusion in poly-crystalline systems that show the activation of grain boundary diffusion, and the TEM observations of TRISO fuel suggest that the fast mechanism observed in this study is in fact grain boundary diffusion.

5.3 Thermal Diffusion

5.3.1 Bulk Diffusion

Table 5.1 lists all the bulk thermal diffusion coefficients, calculated according to Eq. 3.9, in this study for all three elements. The majority of the bulk diffusion coefficient error comes from the shallow diffusion depths. Cesium bulk diffusion was measured between 900°C and 1,300°C. Europium bulk diffusion was measured between 1,100°C and 1,300°C. Strontium bulk diffusion was measured between 1,066°C and 1,300°C. Figure 5.1 is an Arrhenius plot of these diffusion coefficients and Arrhenius fits used to extract activation energies and pre-factors. Below 1,150°C cesium bulk diffusion is faster than either strontium or europium diffusion. Strontium bulk diffusion is faster than that for europium at all temperatures.

Table 5.2 lists the fitted activation energies and pre-factors. The scatter in

the data about the fit creates large errors in the pre-factors, while the error in the diffusion coefficients themselves dominate the error in the activation energy. The activation energies for europium and strontium bulk diffusion are very similar indicating they diffuse via similar hop mechanisms. There is no literature data on experimentally measured activation energies for specific mechanisms for cesium, strontium or europium diffusion. Shrader et al. calculated migration barriers for cesium in SiC [101]. They found that the fastest bulk diffusion mechanism involved a ring exchange process in which cesium could hop between substitutional carbon sites by temporarily moving into a silicon vacancy and involved the coordination of 2 negatively charged silicon vacancies to facilitate the process. The activation energy for this process was 5.14 eV, which is significantly higher than the measured activation energy of 1.0 eV. No calculations for either strontium or europium diffusion are available in the literature.

5.3.2 Grain Boundary Diffusion

This study was not able to directly measure the grain boundary diffusion coefficient, but rather the triple product of the diffusion coefficient, the grain boundary width and the segregation factor. The grain boundary width is already well characterized experimentally between 0.5 nm and 2 nm [60]. The segregation factor is far more difficult to measure or calculate. Experiments on model systems have noted that the segregation factor can vary by six orders of magnitude. The segregation of solute to the grain boundary is a thermodynamic process governed by a segregation energy and varies as a function of temperature:

$$s = exp(E_{seg}/kT) \tag{5.1}$$

As a result, the activation energy measured here is a sum of the migration barrier and the segregation energy. Calculating the segregation energy is also difficult. To first approximation, the segregation energy is the elastic energy released from the lattice when a solute moves from the bulk to the grain boundary [102]:

$$E_{Seg} = \frac{24\pi K G r^3 \xi^2}{3K + 4G} \tag{5.2}$$

where K is the solute bulk modulus, G is the matrix shear modulus, r is covalent radius of the solute atom and ξ is the misfit between the covalent radius of the solute atom and the atomic radius of the matrix itself: $\xi = (r - r_{matrix})/r$. Table 5.3 shows the parameters used in this calculation as well as the segregation energies using a matrix sheer modulus of 160GPa [13] and matrix atomic radius of 0.128 nm, which is the Si-C spacing in 3C-SiC. The covalent radii are very similar amongst these three elements, so the bulk modulus dominates the differences in segregation energies. Cesium has the lowest segregation energy due to a very low bulk modulus, while strontium has the highest due to a large bulk modulus. Cesium also has the largest misfit, suggesting that it undergoes the largest compressive strain from the lattice. This formalism is useful in elucidating trends in segregation behavior [103]. These segregation energies suggest that strontium is the mostly strongly segregating to grain boundaries, while cesium is the least strongly segregating and that europium segregation to grain boundaries should be similar but less than that of strontium.

Table 5.1 lists grain boundary diffusion coefficients, calculated by dividing the triple product ($s\delta D_{GB}$) from Eq. 3.12 by the $s\delta$ assuming δ is 1 nm and using Eq. 5.1 for s with the segregation energies in Table 5.3. Cesium grain boundary diffusion was measured between 900°C and 1,300°C. Europium grain boundary diffusion was measured between 1,100°C and 1,300°C. Strontium grain boundary diffusion was measured between 900°C and 1,300°C. It also lists the relative error from the fit of

the grain boundary tail vs the total error in the grain boundary diffusion coefficient. In all cases the majority of the error in the grain boundary diffusion coefficient comes from the error in the bulk diffusion coefficient. Cesium has higher relative grain boundary errors due to very low overall grain boundary diffusion resulting in shallow profiles with larger fitting errors than the comparable strontium or europium profiles. The high segregation energies for strontium and europium suggest that these two FPs have slow diffusion kinetics, but the thermodynamics of grain boundary segregation drive them to diffuse in comparable amounts via grain boundaries.

Figure 5.2 is an Arrhenius plot of the triple products with the Arrhenius fits used to extract activation energies and pre-factors. Below $1,100°C$ cesium grain boundary diffusion is faster than either strontium or europium grain boundary diffusion. Above $1,100°C$ cesium grain boundary diffusion is slowest. Europium grain boundary diffusion is faster than that for strontium at all temperatures.

Table 5.2 also lists the fitted activation energies and pre-factors for grain boundary diffusion. The activation energies for europium and strontium grain boundary diffusion are very similar indicating that they diffuse via similar paths. There are no experimental values for grain boundary diffusion of cesium, europium or strontium diffusion in SiC. Rabone et al. investigated the hop mechanisms for cesium diffusion along $\Sigma 5$ grain boundaries [104] using accelerated density functional theory (DFT). They found very large incorporation energies ($> 7eV$) for cesium in the $\Sigma 5$ grain boundary suggesting that the solubility of cesium in $\Sigma 5$ grain boundaries is very low. They also calculated migration barriers at various locations along the $\Sigma 5$ grain boundary which ranged from 2 eV to 5.4 eV. Assuming that the lowest energy hop is preferred, these calculations are very close to the migration energy measured in this study at 2.2 eV. Their calculations did not consider significant restructuring of the $\Sigma 5$ grain boundary near the incorporation site for cesium and the electron density maps indicated that cesium bonding to the grain boundary could play an important factor in altering the

migration energies.

This is the first time that the thermally driven bulk and grain boundary diffusion of cesium, europium and strontium were measured in SiC. Cesium exhibited mixed diffusion kinetics between 900°C and 1,300°C indicating that both bulk and grain boundary diffusion mechanisms are active. Strontium exhibited grain boundary dominant diffusion kinetics at 900°C, but mixed diffusion kinetics above 1,066°C. Europium exhibited mixed diffusion kinetics above 1,100°C, but was not measured below this temperature. The segregation energies of strontium and europium are similar suggesting that europium will exhibit grain boundary dominant kinetics below 1,066°C.

5.4 Radiation Enhanced Diffusion

5.4.1 Bulk Diffusion

The radiation enhanced diffusion (RED) of cesium, europium and strontium via the bulk was measured at a dose rate of 4.6×10^{-4} dpa s^{-1} using ion irradiation as the damage source. Table 5.4 lists the bulk diffusion coefficients calculated in this study using Eq.3.9. Bulk diffusion was measurable for all three elements between 900°C and 1,100°C in the irradiated condition.

Figures 5.3 - 5.5 plot the RED coefficient as well as the thermal diffusion coefficients for cesium, europium and strontium bulk diffusion. The cesium RED coefficient exhibits significant enhancement over thermal diffusion and trends weakly down with temperature. Europium bulk RED at 1,100°C is comparable with thermal diffusion. Below this temperature the europium RED enhancement should be significant. Strontium bulk RED exhibits significant enhancement at all temperatures and a strongly increasing trend with temperature.

Table 5.5 lists the activation energies for bulk RED. The activation energies

for strontium and europium bulk diffusion are very similar under purely thermal conditions. Under irradiation, that changes drastically. Strontium bulk RED is faster than either europium or cesium bulk RED for bulk diffusion. Only strontium bulk RED exhibits the expected behavior of a thermally controlled process as a function of temperature with a positive activation energy.

Figure 5.6 shows the radiation enhancement for the bulk diffusion for all three fission products of interest. The bulk diffusion enhancement is plotted in blue with solid, dotted, and dashed lines differentiating between cesium, europium, and strontium. At 900°C all three elements show significant enhancement of diffusion via the bulk. This enhancement is negligible by 1,100°C for europium bulk diffusion. Cesium bulk and strontium bulk radiation enhancement both become negligible by 1,300°C. The significantly larger radiation enhancement for strontium and europium bulk diffusion vs. cesium bulk diffusion suggest that defect concentrations are more closely coupled with strontium and europium bulk diffusion than cesium bulk diffusion. This could also imply that more defects are involved in the migration of strontium and europium diffusion than cesium diffusion.

5.4.2 Grain Boundary Diffusion

The RED of cesium, europium and strontium via grain boundaries was measured at a dose rate of 4.6×10^{-4} dpa s^{-1} using ion irradiation as the damage source. Table 5.4 lists the grain boundary diffusion coefficients calculated in this study as well as the relative errors from the fit of the grain boundary tail vs the total error in the grain boundary diffusion coefficient. Grain boundary diffusion coefficients were calculated by dividing the triple product ($s\delta D_{GB}$) from Eq. 3.12 by the $s\delta$ assuming δ is 1 nm and using Eq. 5.1 for s with the segregation energies in Table 5.3. Grain boundary diffusion was measurable for all three elements between 900°C and 1,100°C in the irradiated condition. The high segregtion energies for strontium and europium

suggest that grain boundary diffusion kinetics are slower than bulk diffusion kinetics but the thermodynamics of grain boundary segregation allow for comparable diffusion via both mechanisms.

Figures 5.7 -5.9 plot the radiation enhanced diffusion coefficient as well as the thermal diffusion coefficients for cesium, europium and strontium grain boundary diffusion. Both strontium and europium grain boundary diffusion exhibit downward trends with temperature, while cesium grain boundary diffusion has an inflection around $1,000$°C. Both cesium and strontium RED exhibit significant enhancement over thermal diffusion. Europium also exhibits an enhancement of RED over thermal diffusion, but the enhancement is eliminated by $1,100$°C.

Table 5.5 also lists the activation energies for grain boundary RED. It was not possible to fit an Arrhenius curve to the cesium grain boundary RED values. The activation energies for strontium and europium grain boundary diffusion are also very similar under purely thermal conditions. Under irradiation, that changes drastically. Strontium RED is faster than europium, but comparable with cesium RED for grain boundary diffusion.

Figure 5.10 shows the radiation enhancement for bulk and grain boundary diffusion for all three fission products of interest. The bulk enhancement is plotted in blue while the grain boundary enhancement is plotted in red. At 900°C all three elements show significant enhancement of diffusion by grain boundaries. This enhancement is negligible by $1,100$°C for europium grain boundary diffusion. Strontium grain boundary radiation enhancement becomes negligible by $1,300$°C. Cesium grain boundary diffusion exhibits enhancement up to $1,300$°C.

Both cesium and strontium exhibit significant radiation enhancement between 900°C and $1,300$°C, while the radiation enhancement of europium is negligible by $1,100$°C. Both cesium and strontium also exhibit a larger enhancement for grain boundary diffusion than bulk diffusion, while europium exhibits the opposite behavior.

The difference for the enhancement of europium diffusion is within an order of magnitude. This is the error of the thermal and radiation enhanced diffusion coefficients indicating that the two mechanisms exhibit the same enhancement within error. Cesium grain boundary diffusion exhibits significantly more radiation enhancement than bulk diffusion indicating that cesium grain boundary diffusion is more limited by the concentration of defects available to mediate diffusion than cesium bulk diffusion in SiC. The enhancement for strontium diffusion via bulk or grain boundaries is similar across all temperature ranges, and the difference in slopes is most likely due to the error in the measurements. The enhancement for europium diffusion for both mechanisms is within the error of the diffusion measurements. This suggest that europium diffusion is the least limited by defect concentrations.

5.4.3 Point Defect Reaction Model

The radiation enhancement of bulk diffusion is governed by the flux of point defects [83]. Radiation enhanced diffusion coefficients should follow the defect concentrations. At low irradiation temperatures the production of point defects overwhelms thermal defects and the concentrations grow to be so large that recombination of point defects dominates. As the temperature continues to rise the flux of point defects to sinks becomes significant, reducing the point defect concentrations. Eventually the thermally supported concentration of defects becomes significant and dominates the trend in defect concentrations.

The point defect reaction equations were solved for SiC to verify the temperature range in which the point defect concentrations transition from thermally dominated to radiation dominated and to determine whether these transitions are consistent with our results for cesium, europium and strontium RED. The rate of change in the vacancy and interstitial concentrations for silicon and carbon are given by:

$$\begin{aligned}\frac{dC_i^{Si}}{dt} =& K_0^{Si} - k_{ii}^{Si} C_i^{Si} C_i^{Si} - k_{iv}^{Si} C_i^{Si} C_v^{Si} \\ & - k_{ii}^{SiC} C_i^{Si} C_i^C - k_{iv}^{Si-C} C_i^{Si} C_v^C - k_{is}^{Si} C_i^{Si} C_s\end{aligned} \tag{5.3}$$

$$\begin{aligned}\frac{dC_v^{Si}}{dt} =& K_0^{Si} - k_{iv}^{Si} C_v^{Si} C_i^{Si} - k_{vv}^{Si} C_v^{Si} C_v^{Si} \\ & - k_{iv}^{C-Si} C_v^{Si} C_i^C - k_{vv}^{SiC} C_v^{Si} C_v^C - k_{vs}^{Si} C_i^{Si} C_s\end{aligned} \tag{5.4}$$

$$\begin{aligned}\frac{dC_i^C}{dt} =& K_0^C - k_{ii} C_i^C C_i^{Si} - k_{iv}^{C-Si} C_i^C C_v^{Si} \\ & - k_{ii}^C C_i^C C_i^C - k_{iv}^C C_i^C C_v^C - k_{is}^C C_i^{Si} C_s\end{aligned} \tag{5.5}$$

$$\begin{aligned}\frac{dC_v^C}{dt} =& K_0^C - k_{iv}^{Si-C} C_i^{Si} C_v^C - k_{vv}^{SiC} C_v^{Si} C_v^C \\ & - k_{iv}^C C_i^C C_v^C - k_{vv}^C C_v^C C_v^C - k_{vs}^C C_i^C C_s\end{aligned} \tag{5.6}$$

Here, dC_j^A/dt is time differential for the concentration of species j on sub-lattice A. K_0^{Si} and K_0^C are the damage production rates on either sub-lattice obtained from SRIM using the Kinchin-Pease mode to determine K_0 and the full cascade mode to calculate how the damage is partitioned to either sub-lattice [81]. k_{jl}^A is the reaction rate coefficient between species j and l on sub-lattice A. C_s is the sink density.

There are two primary sinks in CVD-SiC: stacking faults and grain boundaries. Sinks strengths, defined as k_m^2 where m refers to the sink, provide a way to compare the relative importance of various sinks in the material for the point defect concentrations. The sink strength for stacking faults is: $k_{sf}^2 = z_{sf}\rho_{sf}$, where z_{sf} is the bias to stacking faults and ρ_{sf} is the stacking fault density. The bias for stacking faults is generally no more than 2% [83], and the stacking fault density in SiC is $10^{14} cm^{-2}$ [76], yielding a

stacking fault sink strength of $1.02 \times 10^{14} cm^{-2}$. The sink strength for grain boundaries is: $k_{gb}^2 = 24/d^2$, where d is the grain size [83]. The grain size in the CVD SiC used in this study is $1.8 \mu m$, yielding a grain boundary sink strength of $7.4 \times 10^{10} cm^{-2}$.The sink strength for stacking faults is three orders of magnitude higher than the sink strength for grain boundaries indicating that grain boundaries do not control the overall point defect concentrations reducing the sink term to annihilation at stacking faults, therefore C_s is the stacking fault density, ρ_{sf}.

Table 5.6 defines the reaction rate coefficients which are functions of the interaction radii and point defect diffusivities. The interstitial diffusivities are given in literature [37]. Vacancy diffusivities were back-calculated from the self-diffusion coefficients [105] and the vacancy formation energies [22] assuming carbon and silicon self-diffusion in SiC occur by way of vacancies near the melting temperature [106, 107].

$$D^{Si} = D_v^{Si} C_v^{Si} + D_i^{Si} C_i^{Si} \approx D_v^{Si} C_v^{Si}$$
$$D^{C} = D_v^{C} C_v^{C} + D_i^{C} C_i^{C} \approx D_v^{C} C_v^{C}$$

$$D_v^{Si} \approx D^{Si}/C_v^{Si} \tag{5.7}$$

$$D_v^{C} \approx D^{C}/C_v^{C} \tag{5.8}$$

Table 5.7 lists the parameters used to calculate the resulting point defect diffusivities. The radii for point defect interaction are based on the geometry of the two inter-penetrating FCC lattices and the nearest neighbor distances. The zinc-blende system is an FCC lattice with a two atom basis: one on the origin and another of the opposing type on $^1/_4$ the body diagonal. The geometry factors for nearest neighbor interactions on the same sub-lattice and opposing sub lattices are the same. The nearest neighbor distance for defects on the same sub-lattice is then the nearest neighbor distance of the FCC lattice which is $^1/_{\sqrt{2}} a_0$. The nearest neighbor distance for opposing lattices

is the basis distance or the nearest atom distance which is $^{\sqrt{3}}/_{4}a_0$. Figure 5.11 shows two ball and stick models labeling the near atom distance and the nearest neighbor distance. Table 5.8 defines the interaction radii and the parameters necessary to the point defect concentrations.

At steady-state, all the differentials of concentration with time in Eqs (5.3-5.6) are set equal to 0, which leaves a set of coupled equations that can be solved numerically as a function of temperature. A scientific computing and analysis package,SciPy [89], was used to solve these coupled non-linear equations to determine the point defect concentration under ion-irradiation and neutron irradiation damage rates.

Figure 5.12 shows the point defect concentrations determined from Eqs. (5.3-5.6) under the ion irradiation conditions used here. There are three regimes for the point defect concentration. At low temperatures, the production of defects by irradiation swamps the thermal concentrations. As temperature increases, the diffusivity of point defects increase, increasing the loss rate due to recombination and annihilation at sinks. A constant production rate and increasing loss rate creates a decreasing point defect concentration as a function of temperature. At high temperatures, the thermal production of point defects controls the point defect concentration. Excess point defects created by irradiation are quickly removed from the system via loss mechanisms and the material returns to thermal equillibrium. At intermediate temperatures these two regimes overlap, creating an athermal knee region where the point defect concentrations are flat. The carbon vacancy concentration decreases with temperature between 900°C and $1,100$°C. Conversely, the silicon vacancy concentration monotonically increases between 900°C and $1,100$°C. Both interstitial concentrations have inflection points in this temperature range.

Figure 5.13 shows the point defect concentrations determined from Eqs. (5.3-5.6) using a dose rate of $1.6 \times 10^{-7} dpa\ s^{-1}$ which is relevant to neutron irradiation conditions as per the AGR-1 fuel irradiation campaign conducted by INL at the

Advanced Test Reactor [2]. The knees in the defect concentrations shift to much lower temperatures, below 900°C, below the irradiation temperature range for AGR-1 and the expected operating temperature range for TRISO in a VHTR. This indicates that a neutron irradiation campaign would not be able to observe the inflection points in the diffusion coefficient to determine the sub-lattice and defects associated with FP diffusion in SiC. Similarly, they indicate that the RED of FPs in SiC under neutron irradiation will be monotonically increasing over the expected operating temperature range of a VHTR.

The carbon vacancy concentration under ion irradiation decreases as a function of temperature up to $1,100$°C, in agreement with the weakly decreasing trends for cesium bulk, europium bulk, europium grain boundary and strontium grain boundary diffusion. Similarly, the weakly increasing trend for strontium bulk diffusion corresponds well with the positive temperature dependence of the silicon vacancy concentration. The inflection at $1,000$°C for cesium grain boundary diffusion could correspond with either silicon or carbon interstitial concentration.

A sensitivity study was conducted to determine the effect of error in the parameters on the point defect concentrations. Defect migration energies in SiC are strong functions of the Fermi level which depend on the doping. The parameters used in this study assume that SiC is neither n-type or p-type, which could significantly alter the migration energies based on amount and type of fission products in SiC. The migration energies have intrinsic errors on the order of 1 eV [16, 22, 37]. The point defect concentrations exhibited deviations of 710% per eV change in a single migration energy. Concurrent changes in multiple migration energies resulted in larger sensitivities and the sensitivity of the point defect concentrations to a change in all four migration energies was 100,000% per eV, indicating that there are strong coupling effects on the migration energies and the point defect concentrations. It is not possible to calculate diffusion coefficients directly from the point defect concentrations

as the exact mechanism that defines how point defects mediate diffusion is not known. As a result, the absolute magnitude of the point defect concentrations and the relative magnitudes are of little consequence to the overall conclusions from this study, which focuses on the location of the inflection points to correlate fission product diffusion with a sub-lattice defect. The inflection points exhibited deviations of 100°C per eV change in the migration energies. The inflection points in the silicon interstitial and silicon vacancy concentrations are within 60°C of each other, which could change the defect on the silicon sub-lattice associated with strontium bulk diffusion. The sensitivity in the temperature of the inflection points does not affect the other conclusions.

At a dose rate relevant to ion irradiation, $4.6 \times 10^{-4} dpa\ s^{-1}$, the point defect concentrations are insensitive to any deviation in the sink density within the limitations of error in a numerical solution. At a sink density of $10^18 cm^{-2}$, the numerical solutions for the point defect concentrations became unstable. Decreasing the sink density to 0, had no effect on the point defect concentration, indicating that the recombination of point defects controls the point defect concentration. At a dose rate relevant to neutron irradiation conditions, $1.6 \times 10^{-7} dpa\ s^{-1}$, the point defect concentrations do change as a function of the sink density. The point defect concentrations exhibit a change of 0.08% per % change in the sink density. The inflections points exhibit deviations of 5.5×10^{-4} °C per % change in the sink density. This corresponds to a 0.55°C deviation in the inflection points for a factor 10 increase in the sink density, which doesn't alter the correlations between point defects and diffusivities identified in this study.

This is the first time that the radiation enhanced bulk and grain boundary diffusion of cesium, europium and strontium were measured in SiC. All three FPs exhibited mixed diffusion kinetics with measurable diffusion coefficients between 900°C and 1,100°C indicating that both mechanisms are important for these three FPs. Europium

had negligible radiation enhancement for bulk and grain boundary diffusion by $1,100°C$. All but cesium grain boundary diffusion exhibited negligible enhancement at $1,300°C$. A point defect model elucidated the atomistics associated with FP Diffusion. It indicates that cesium bulk, europium bulk and grain boundary, as well as strontium grain boundary diffusion are likely to proceed on the carbon sublattice, while strontium bulk diffusion is likely to proceed via the silicon sublattice.

5.5 Comparison with Reactor Data

5.5.1 FP Release Data

The IAEA TECDOC-978 report contains the most widely accepted and utilized diffusion data to benchmark TRISO FP release [1]. The suggested pre-factors and activation energies from the TECDOC are listed in Table 5.9. The TECDOC lists two activation energies for cesium and strontium corresponding to a low temperature mechanism below $1,600°C$ and a high temperature mechanism above this temperature. This study was limited to $1,300°C$ and can only be compared with the low temperature mechanism from the TECDOC. The low temperature activation energy of cesium at 1.3 eV from the TECDOC compares favorably with the bulk diffusion coefficient of 1.0 eV calculated here. Neither the bulk nor grain boundary activation energies measured here for strontium compare with the TECDOC's low temperature activation energy at 2.1 eV.

Figure 5.14 is an Arrhenius plot of cesium diffusion data from past TRISO test programs used to calculate the fits for high temperature ($> 1,600°C$) and low temperature ($< 1,600°C$) diffusion mechanisms in the IAEA TECDOC-978. These diffusion coefficients were obtained by irradiating TRISO fuel in hexagonal compacts or spherical pebbles in materials test reactors and test gas reactors, followed by annealing in a furnace at high temperature. The release rate of cesium was monitored during the

annealing and then plotted against ideal solutions of the diffusion equation assuming the SiC is the key retaining layer to calculate a diffusion coefficient. Defect fractions and failure fractions were difficult to quantify in these irradiations and the quality of the TRISO fuel varied greatly. As a result, TRISO particles could have failed during irradiation or annealing, release a full particle's inventory of cesium, which would then be averaged over the entire compact or pebble. It is believed that most of the literature data that trends with the high temperature and low temperature mechanisms for the IAEA fits are due to release from TRISO failure. There is batch of historic data that is significantly lower than the rest from Myers/Nabielek circled in red in Figure 5.14. This is from the German TRISO program which has historically had the lowest defect fraction of any TRISO program, and as a result the best quality TRISO particles. The low release diffusion coefficients from Myers/Nabielek support the theory that the rest of the release measurements are of failed TRISO averaged over a compact or pebble and not diffusion through intact SiC.

Diffusion coefficients from thermal annealing are plotted on top of the literature data in Figure 5.15a . Bulk diffusion coefficients are plotted in blue while grain boundary diffusion coefficients are plotted in red. The grain boundary diffusion coefficient are plotted using the segregation energies tabulated in Table 5.3 and a grain boundary width of 1 nm. Both bulk and grain boundary diffusion coefficients from this study agree with the Myers/Nabielek diffusion coefficients from high quality German TRISO fuel. The agreement between the cesium diffusion coefficients measured in this study and the cesium diffusion coefficients measured by Myers/Nabielek via cesium release measurements of high quality TRISO fuel support the premise that high quality SiC should exhibit minimal cesium diffusion.

RED coefficients from the ion irradiations are plotted on top of the literature data in Figure 5.15b. Bulk diffusion coefficients are plotted in blue while grain boundary diffusion coefficients are plotted in red. Open circles indicate diffusion coefficients

from the ion irradiations, while closed circles are for RED coefficients that have been dose rate adjusted to the neutron irradiation dose rate discussed in the next section. The ion irradiation RED coefficients show a significant diffusion enhancement well over the cesium diffusion coefficients seen in TRISO fuel and straddle the low temperature fit from ref [1]. This suggests that radiation damage could be a key component of the variability in cesium release.

As stated previously the fabrication route is key to the performance of SiC. Small differences such as CVD vs. fluidized bed CVD, which are the two processes for the substrate used here vs. TRISO SiC, can greatly change the chemical and thermo-mechanical properties [13]. Still the trends should be comparable as the substrate used here is theoretical density CVD 3C-SiC with a similar grain size to TRISO SiC [108]. Qualitatively, the trends in the diffusion data agree with what has been seen in the literature. At low temperatures, cesium appears to be more mobile than strontium [109]. Strontium release correlates well with europium release [2, 62, 110, 111]. Recent TRISO test fuel shows an order of magnitude greater europium release than strontium, which correlates well with a larger grain boundary diffusion coefficient for europium than strontium both determined in this study and in the literature [112].

5.5.2 Fission Product Release Modeling

Most of the measurements made in this study were in the mixed diffusion regime. In fuel and in fuel modeling, it is difficult to model or to incorporate a dual diffusion system. One way to work around this is to use an effective diffusion coefficient. The Kalnin equation [113] is a mean-field approximation for effective diffusion of solutes in a material. It accounts for the partial trapping of solutes by the bulk, the energy barrier for a solute to diffuse into the bulk from the grain boundary, as well as the effect of networking of grain boundaries around grains creating additional trapping

area. As a result, the effective diffusion coefficient can be lower than either bulk or grain boundary diffusion coefficients if the grain boundary segregation factor is large and the bulk and grain boundary diffusion coefficients are comparable. This is an indicator that the solubility of the solute in the bulk and grain boundary is as important in the mobility of the solute as the diffusivity.

The Kalnin equation is defined as:

$$D_{eff} = \frac{sD_{GB}\left[(3-2)D_B + 2fsD_{GB}\right]}{(1-f+sf)\left[gD_B + (3-f)sD_{GB}\right]} \tag{5.9}$$

where f is the fraction of atomic sites belonging to grain boundaries and s is the segregation factor. For solute diffusion f can be defined by:

$$f = \frac{q\delta}{d} \tag{5.10}$$

where q is a geometry factor for the shape of grains and the dimensionality of the diffusion paths. For 3D diffusion $q \sim 3$. δ is the grain boundary width and d is the grain size. δ ranges from 0.5 nm to 2 nm, depending on the grain boundary type [60]. The term sD_{GB} can come from the mixed diffusion measurements of grain boundary diffusion.

The dot-dashed red line in Figure 5.15a is the effective thermal diffusion coefficient calculated using equation 5.9, a segregation energy of 0.39 eV as calculated in Table 5.3, δ of 1nm, q of 3, d of 1.8μm and the cesium diffusion coefficients for the case of thermal annealing. The effective thermal diffusion coefficient (D_{Eff}) is very similar in slope to the TECDOC fit in the low temperature regime, but 2.5 orders of magnitude lower. This difference in magnitude between the effective thermal diffusion coefficient calculated here and the TEDOC fit agrees with the discrepancy observed in predictions of cesium release by PARFUME using the TECDOC fit and those measured by deconsolidation-leach-burn-leach method for the NGNP AGR-1

irradiation [112]. Figure 5.16 shows the cesium release for 6 compacts from the AGR-1 irradiation that exhibit between 1 and 3 orders of magnitude over-prediction in cesium release by PARFUME using the IAEA diffusion coefficients as compared with release measurements [112]. The quality of the SiC used here is a limiting case and should exhibit the lowest diffusion coefficients for cesium. This validates the premise that high quality TRISO SiC should have minimal cesium release. The release levels corresponding to these diffusion coefficients are less than the total inventory of a single TRISO particle [1]. This also validates the assumption that cesium release greater than the total inventory of a single particle can be used to determine if any TRISO particles have fully fractured SiC.

The RED coefficients plotted in Figure 5.15b are those measured in the ion irradiated samples. However, to properly compare with the literature data, which are a result of reactor irradiations at much lower dose-rates, the RED coefficients have to be scaled to account for the difference in dose-rate. There are two limits on the scaling of the RED coefficients based on the microstructure that controls the point defect concentrations. One limit is when recombination of point defects controls the point defect concentrations, which occurs at low temperature and high dose-rates. The other limit is when annihilation of defects at sinks controls the point defect concentration, which occurs at high temperatures and low dose-rates. The definition of high and low temperature as well as high and low dose-rates are microstructure dependent [83]. It is likely that the ion irradiations, due to the higher dose rates, are closer to the recombination dominant regime and the neutron irradiations, due to their lower dose rates, are closer to sink dominant regime, but can not be verified. The exact scaling law is $D_{RED} \propto K_0^n$, where n is between 0.5 and 1, and accounts for the likelihood that the two dose-rates are in different point defect regimes. The neutron dose rate corrected RED coefficients plotted in Figure 5.15b assume the scaling is $K_0^0.5$ to calculate the worst case diffusion coefficient for cesium release.

These coefficients span the range between the thermal diffusion coefficients and the IAEA low temperature mechanism, suggesting that radiation is a key factor in the variability of cesium release.

Comparison with activation energies and pre-factors suggested by IAEA TECDOC-978 reveals a disagreement of 2 to 3 orders of magnitude in diffusion coefficients measured in this study for thermal conditions and those suggested in the TECDOC. Still, effective thermal diffusion coefficients calculated in this study agree well with the lower bounds of diffusion coefficients calculated from cesium release measurements and effective RED coefficients span most of the range in diffusion coefficients calculated from cesium release, suggesting that variations in irradiation conditions due to temperature and dose rate affect variations in diffusion observed with TRISO fuel test irradiations. The agreement between the thermal diffusion coefficients for cesium and the lower bounds of cesium diffusion coefficients calculated from cesium release measurements suggest that TRISO with flawless SiC should retain it's full inventory and that high cesium release is a valid indicator of SiC fracture.

Profile	Temperature °C	Location	$D_B(cm^2s^{-1})$	$D_{GB}(cm^2s^{-1})$	Relative Error (%)
Cs-900:40h-01	900	PNNL	$1.5 \pm 0.96 \times 10^{-17}$	$3.4 \pm 1.9 \times 10^{-19}$	49
Cs-1100:10h-01	1100	PNNL	$6.5 \pm 4.7 \times 10^{-17}$	$6.4 \pm 5.9 \times 10^{-17}$	18
Cs-1200:10h-01	1200	PNNL	$9.9 \pm 2.9 \times 10^{-17}$	$2.2 \pm 1.1 \times 10^{-16}$	10
Cs-1100:10h-01	1300	PNNL	$2.2 \pm 1.6 \times 10^{-16}$	$2.2 \pm 0.68 \times 10^{-15}$	34
Eu-1100:10h-01	1100	IEN	$6.8 \pm 4.3 \times 10^{-18}$	$6.9 \pm 5.4 \times 10^{-19}$	3
Eu-1200:10h-01	1200	IEN	$3.4 \pm 1.0 \times 10^{-16}$	$6.7 \pm 2.3 \times 10^{-17}$	7
Eu-1200:10h-02	1200	IEN	$1.4 \pm 0.89 \times 10^{-16}$	$1.0 \pm 0.21 \times 10^{-17}$	4
Eu-1300:10h-01	1300	IEN	$2.6 \pm 0.47 \times 10^{-15}$	$4.5 \pm 0.81 \times 10^{-17}$	6
Sr-900:40h-01	900	PNNL	ND	$2.2 \pm 0.83 \times 10^{-23}$	
Sr-1066:10h-01	1066	IEN	$3 \pm 0.78 \times 10^{-18}$	$1.0 \pm 0.14 \times 10^{-21}$	10
Sr-1100:10h-01	1100	PNNL	$4.4 \pm 1.4 \times 10^{-17}$	$1.5 \pm 0.48 \times 10^{-20}$	6
Sr-1100:10h-02	1100	IEN	$6.8 \pm 4.3 \times 10^{-17}$	$6.2 \pm 3.4 \times 10^{-20}$	6
Sr-1100:10h-03	1100	IEN	$2.2 \pm 1.5 \times 10^{-17}$	$5.0 \pm 2.4 \times 10^{-20}$	7
Sr-1100:10h-04	1100	IEN	ND	$2.2 \pm 1.2 \times 10^{-19}$	18
Sr-1200:10h-01	1200	PNNL	$2.8 \pm 0.84 \times 10^{-16}$	$8.8 \pm 2.8 \times 10^{-19}$	6
Sr-1200:10h-02	1200	IEN	ND	$7.1 \pm 2.0 \times 10^{-19}$	14
Sr-1300:10h-01	1300	IEN	$6.3 \pm 4.9 \times 10^{-15}$	$2.1 \pm 1.7 \times 10^{-17}$	4

Table 5.1: Bulk and grain boundary diffusion coefficients for cesium, europium and strontium thermal diffusion. The relative error is the percent of the error in the grain boundary diffusion coefficient from fitting the grain boundary tail. ND indicates values that were not determined. The sample naming scheme is as follows: FP-Temperature:time-profile number. The 1100C:10h annealing condition for strontium is the only cause in which multiple diffusion couples were fabricated and annealed. Sr-1100:10h-01 and Sr-1100:10h-02 are from one diffusion couple while, Sr-1100:10h-03 and Sr-1100:10h-04 are from the second.

Fission Product	D_0^B $(cm^3 s^{-1})$	E_0^B (eV)	$s\delta D_0^{GB}$ $(cm^3 s^{-1})$	E_A^{GB} (eV)
Cesium	$2.1 \pm 1.5 \times 10^{-13}$	$1.0 \pm 0.1eV$	$1.9 \pm 8.8 \times 10^{-14}$	2.2 ± 0.6
Europium	$1,300 \pm 2,500$	5.5 ± 0.3	$5.4 \pm 31 \times 10^{-5}$	4.7 ± 0.8
Strontium	$1,200 \pm 57,000$	5.7 ± 0.6	$1.4 \pm 1.6 \times 10^{-5}$	4.6 ± 0.1

Table 5.2: Activation energies and pre-factors for cesium, europium and strontium bulk and grain boundary diffusion

FP	K (GPa)	r (pm)	ξ	E_{seg} (eV)
Cesium	1.6	225	0.43	0.39
Europium	8.3	198	0.35	0.91
Strontium	13.2	195	0.34	1.28

Table 5.3: The segregation energy for FPs assuming that only the elastic strain energy is significant.

Profile	Temperature °C	D_B $(cm^2 s^{-1})$	D_{GB} $(cm^2 s^{-1})$	Relative Error (%)
Cs-900:6h:10dpa-01	900	$1.3 \pm 1.0 \times 10^{-15}$	$3.6 \pm 2.3 \times 10^{-13}$	8
Cs-1000:6h:10dpa-01	1,000	$5.3 \pm 3.7 \times 10^{-16}$	$1.8 \pm 1.3 \times 10^{-14}$	9
Cs-1100:6h:10dpa-01	1,100	$5.2 \pm 1.0 \times 10^{-16}$	$4.1 \pm 0.74 \times 10^{-13}$	6
Eu-900:6h:10dpa-01	900	$3.4 \pm 1.8 \times 10^{-17}$	$1.2 \pm 0.57 \times 10^{-18}$	3
Eu-1000:6h:10dpa-01	1,000	$3.3 \pm 1.6 \times 10^{-17}$	$1.2 \pm 0.72 \times 10^{-18}$	6
Eu-1100:6h:10dpa-01	1,100	$2.2 \pm 1.1 \times 10^{-17}$	$8.7 \pm 4.6 \times 10^{-19}$	7
Sr-900:6h:10dpa-01	900	$7.0 \pm 4.3 \times 10^{-16}$	$2.5 \pm 2.1 \times 10^{-16}$	3
Sr-1000:6h:10dpa-01	1,000	$1.2 \pm 0.2 \times 10^{-15}$	$6.5 \pm 3.1 \times 10^{-17}$	9
Sr-1100:6h:10dpa-01	1,100	$4.1 \pm 1.6 \times 10^{-15}$	$6.8 \pm 4.6 \times 10^{-17}$	7

Table 5.4: Radiation enhanced diffusion coefficients for cesium, strontium and europium at a dose rate of 4.6×10^{-3} dpa s^{-1}

Fission Product	D_0^B $(cm^2 s^{-1})$	E_A^B (eV)	$s\delta D_0^{GB}$ $(cm^3 s^{-1})$	E_A^{GB} (eV)
Cesium	$1.7 \pm 4.7 \times 10^{-17}$	-0.4 ± 0.3	ND	ND
Europium	$1.9 \pm 2.9 \times 10^{-18}$	$-0.3 \pm .2$	$1.7 \pm 1.3 \times 10^{-26}$	-1.1 ± 1.0
Strontium	$3.6 \pm 1.9 \times 10^{-9}$	1.6 ± 0.6	$1.1 \pm 0.7 \times 10^{-23}$	-1.2 ± 0.7

Table 5.5: Activation energies and pre-factors for bulk and grain boundary RED of cesium, europium and strontium.

Reaction Rate Coefficients ($cm^3 s^{-1}$)	
k_{iv}^{Si}	$4\pi r_{iv}^{Si}(D_i^{Si} + D_v^{Si})$
k_{iv}^{C}	$4\pi r_{iv}^{C}(D_i^{C} + D_v^{C})$
k_{iv}^{Si-C}	$4\pi r_{iv}^{Si-C}(D_i^{Si} + D_v^{C})$
k_{iv}^{C-Si}	$4\pi r_{iv}^{C-Si}(D_i^{C} + D_v^{Si})$
k_{ii}^{Si}	$4\pi r_{ii}^{Si} 2D_i^{Si}$
k_{ii}^{C}	$4\pi r_{ii}^{C} 2D_i^{C}$
k_{vv}^{Si}	$4\pi r_{vv}^{Si} 2D_v^{Si}$
k_{vv}^{C}	$4\pi r_{vv}^{C} 2D_v^{C}$
k_{ii}	$4\pi r_{ii}(D_i^{Si} + D_i^{C})$
k_{vv}	$4\pi r_{vv}(D_v^{Si} + D_v^{C})$
k_{is}^{Si}	$4\pi z_{id} D_i^{Si}$
k_{vs}^{Si}	$4\pi z_{vd} D_v^{Si}$
k_{is}^{C}	$4\pi z_{id} D_i^{C}$
k_{vs}^{C}	$4\pi z_{vd} D_v^{C}$

Table 5.6: Reaction rate coefficients for the point defect reaction model.

Diffusion Coefficients ($cm^2 s^{-1}$)	
D_i^{Si}	$1.23 \times 10^{-3} exp\left(\frac{-0.74eV}{kT}\right)$
D_v^{Si}	$8.36 \times 10^{7} exp\left(\frac{-2.65eV}{kT}\right)$
D_i^{C}	$3.3 \times 10^{-3} exp\left(\frac{-1.53eV}{kT}\right)$
D_v^{C}	$2.62 \times 10^{8} exp\left(\frac{-2.82eV}{kT}\right)$

Table 5.7: Diffusion coefficients for the point defect reaction model.

Quantity	Value
a_0	4.335Å [13]
r_{iv}^{Si}	$48/\sqrt{2}a_0 = 14.7nm$
r_{iv}^{C}	$48/\sqrt{2}a_0 = 14.7nm$
r_{iv}^{Si-C}	$48\sqrt{3}/4a_0 = 9.0nm$
r_{iv}^{C-Si}	$48\sqrt{3}/4a_0 = 9.0nm$
r_{ii}^{Si}	$84/\sqrt{2}a_0 = 25.7nm$
r_{ii}^{C}	$84/\sqrt{2}a_0 = 25.7nm$
r_{vv}^{Si}	$84/\sqrt{2}a_0 = 25.7nm$
r_{vv}^{C}	$84/\sqrt{2}a_0 = 25.7nm$
r_{ii}^{SiC}	$84\sqrt{3}/4a_0 = 15.8nm$
r_{vv}^{SiC}	$84\sqrt{3}/4a_0 = 15.8nm$
z_{id}	1.02 [83]
z_{vd}	0.98 [83]
C_s	$10^{14}cm^{-2}$ [76]
E_{m-i}^{Si}	$0.74eV$
E_{m-v}^{Si}	$2.65eV$
E_{m-i}^{C}	$1.53eV$
E_{m-v}^{C}	$2.82eV$

Table 5.8: Quantities for the point defect reaction model.

Fission Product	Low Temperature		High Temperature		Thermal Diffusion			
	D_0 $(cm^2 s^{-1})$	E_A (eV)	D_0 $(cm^2 s^{-1})$	E_A (eV)	D_0^B $(cm^2 s^{-1})$	E_A^B (eV)	D_0^{GB} $(cm^2 s^{-1})$	E_A^{GB} (eV)
Cesium	5.5×10^{-10}	1.3	1.6×10^{2}	5.3	2.1×10^{-13}	1.0	1.9×10^{-14}	2.6
Strontium	1.2×10^{-5}	2.1	1.8×10^{10}	8.2	1,200	5.5	1.4×10^{-5}	6

Table 5.9: Activation energies and pre-factors suggested by the IAEA TECDOC-978 compared with activation energies and pre-factors for bulk and grain boundary diffusion measured in this study. [1].

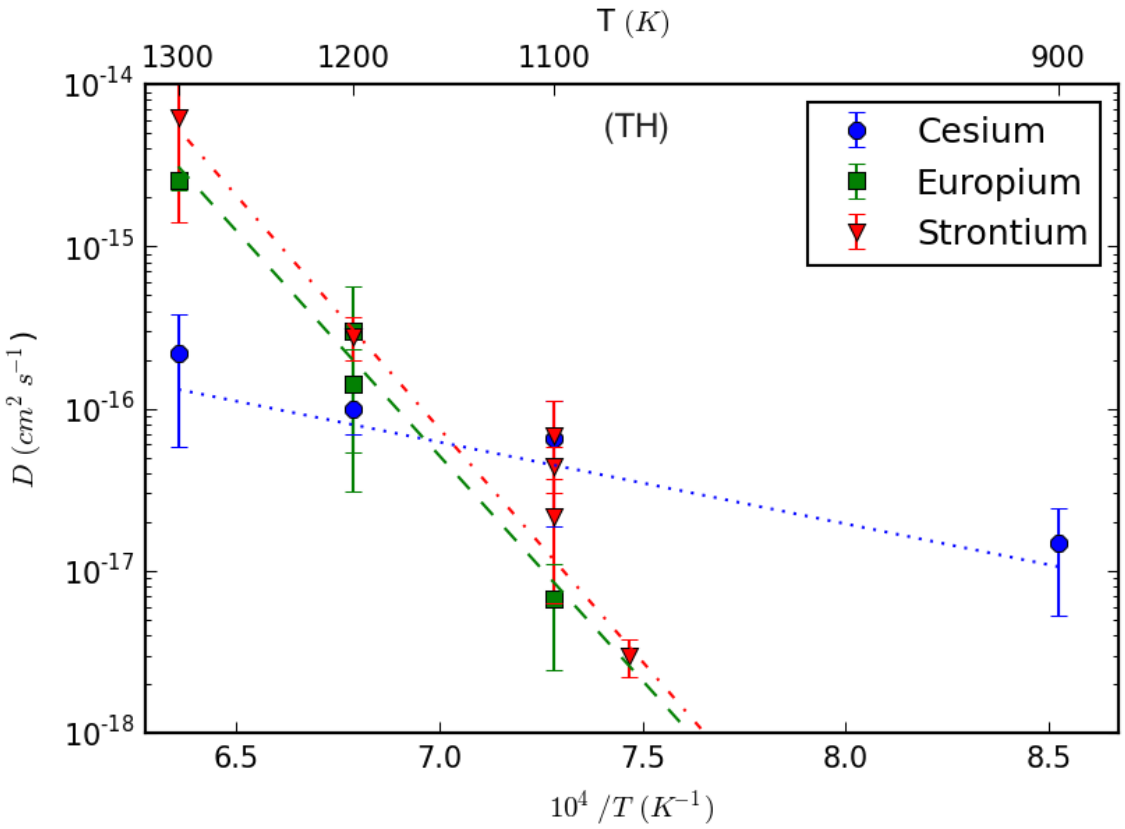

Figure 5.1: Arrhenius plot for cesium, europium and strontium thermal bulk diffusion.

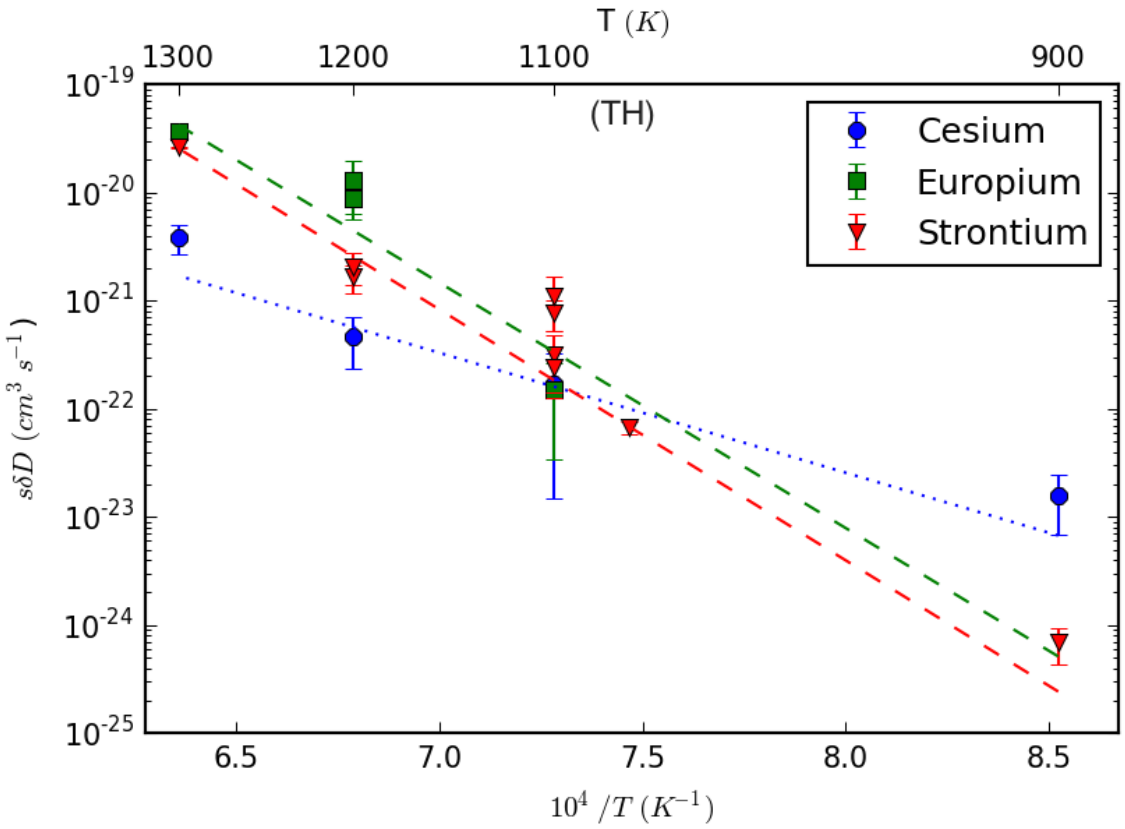

Figure 5.2: Arrhenius plot for cesium, europium and strontium thermal grain boundary diffusion.

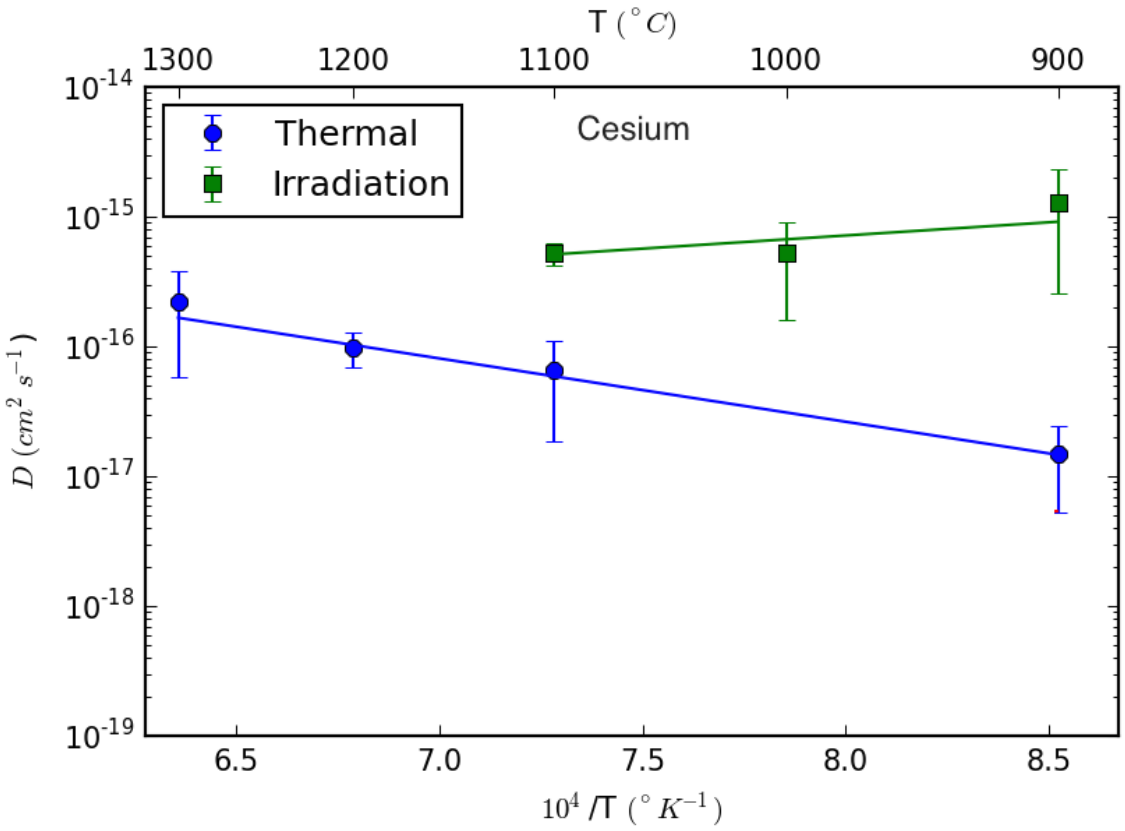

Figure 5.3: Cesium bulk thermal and radiation enhanced diffusion.

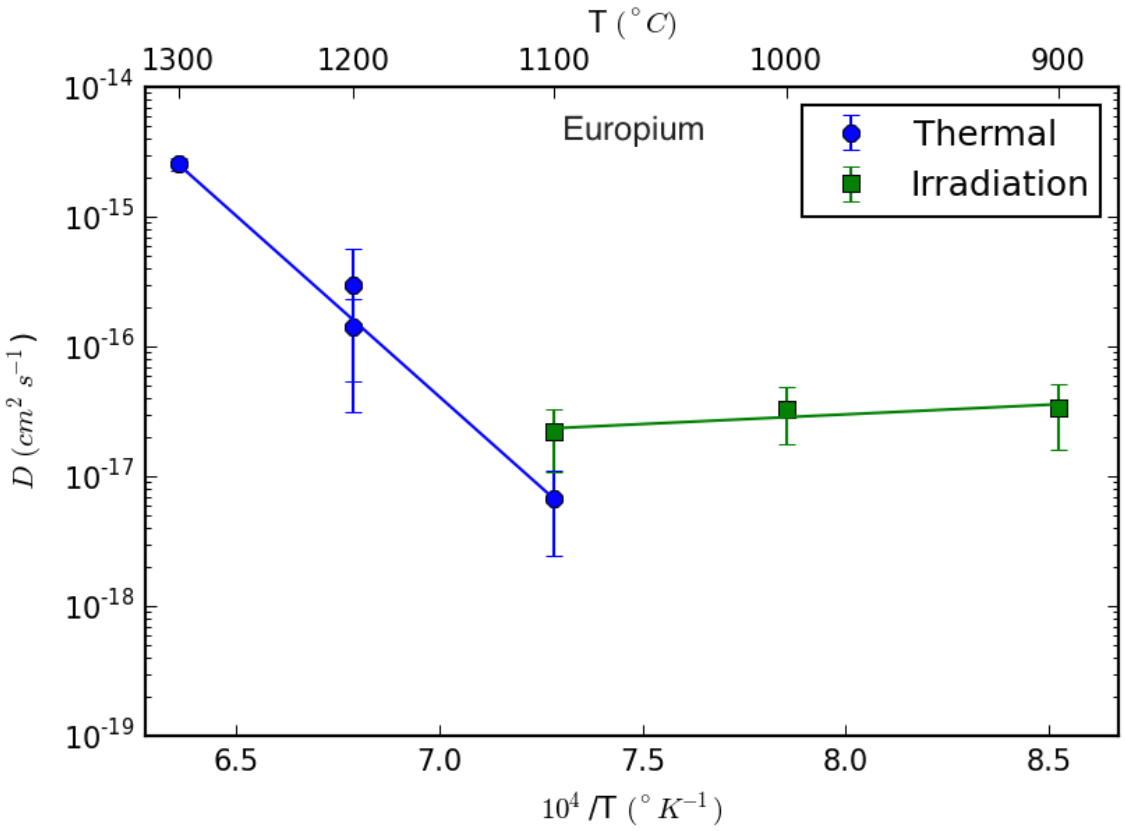

Figure 5.4: Europium bulk thermal and radiation enhanced diffusion.

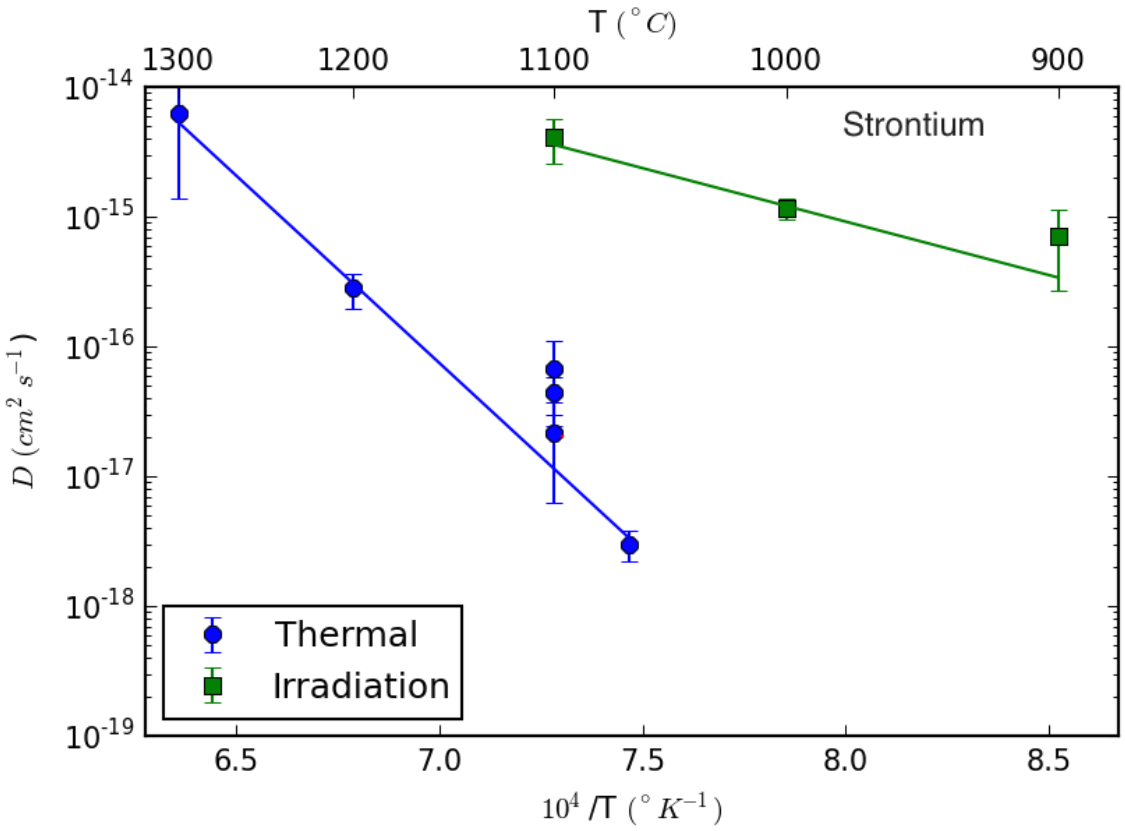

Figure 5.5: Strontium bulk thermal and radiation enhanced diffusion.

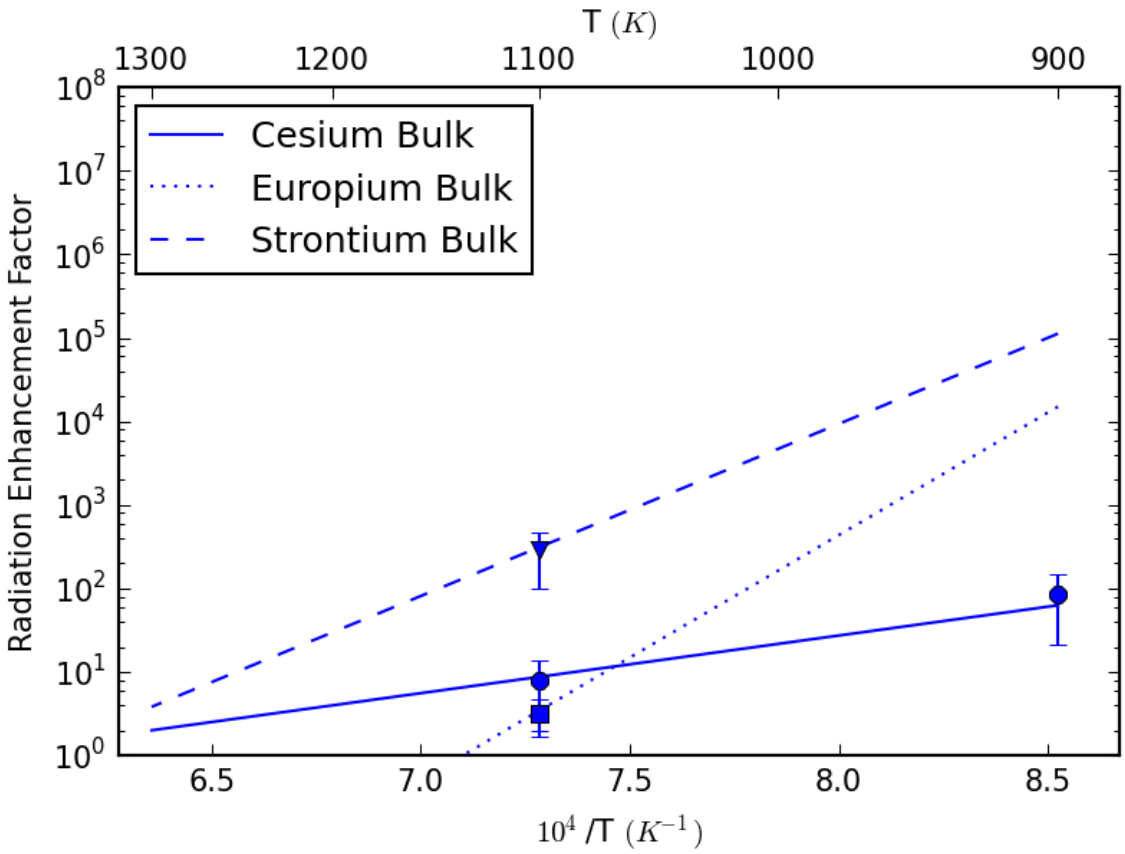

Figure 5.6: Radiation enhancement for the bulk diffusion of cesium, strontium and europium

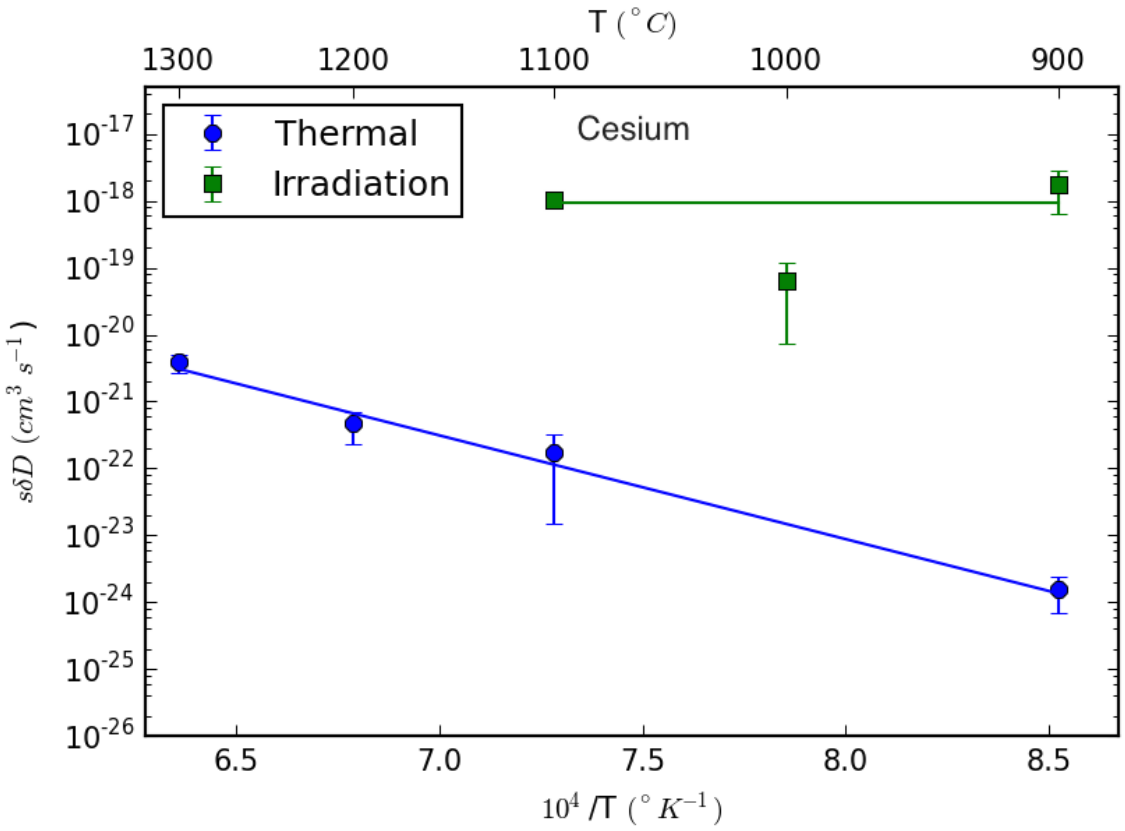

Figure 5.7: Cesium grain boundary thermal and radiation enhanced diffusion.

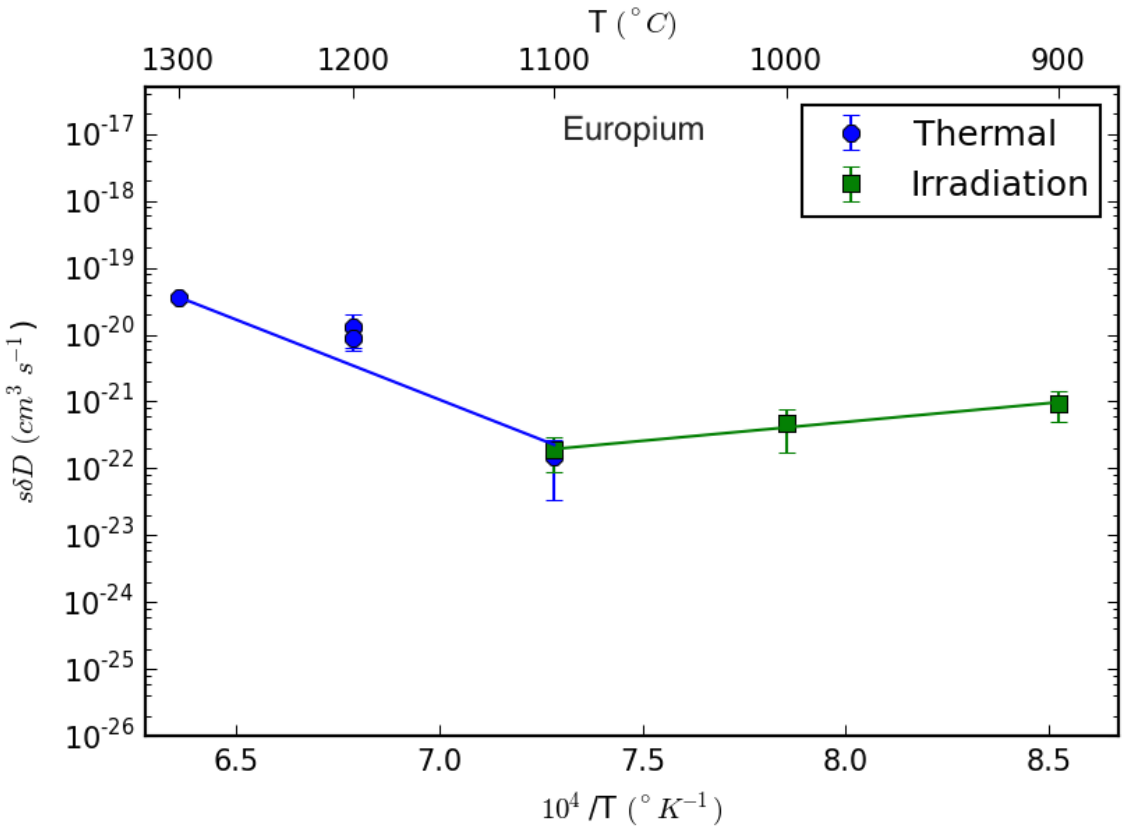

Figure 5.8: Europium grain boundary thermal and radiation enhanced diffusion.

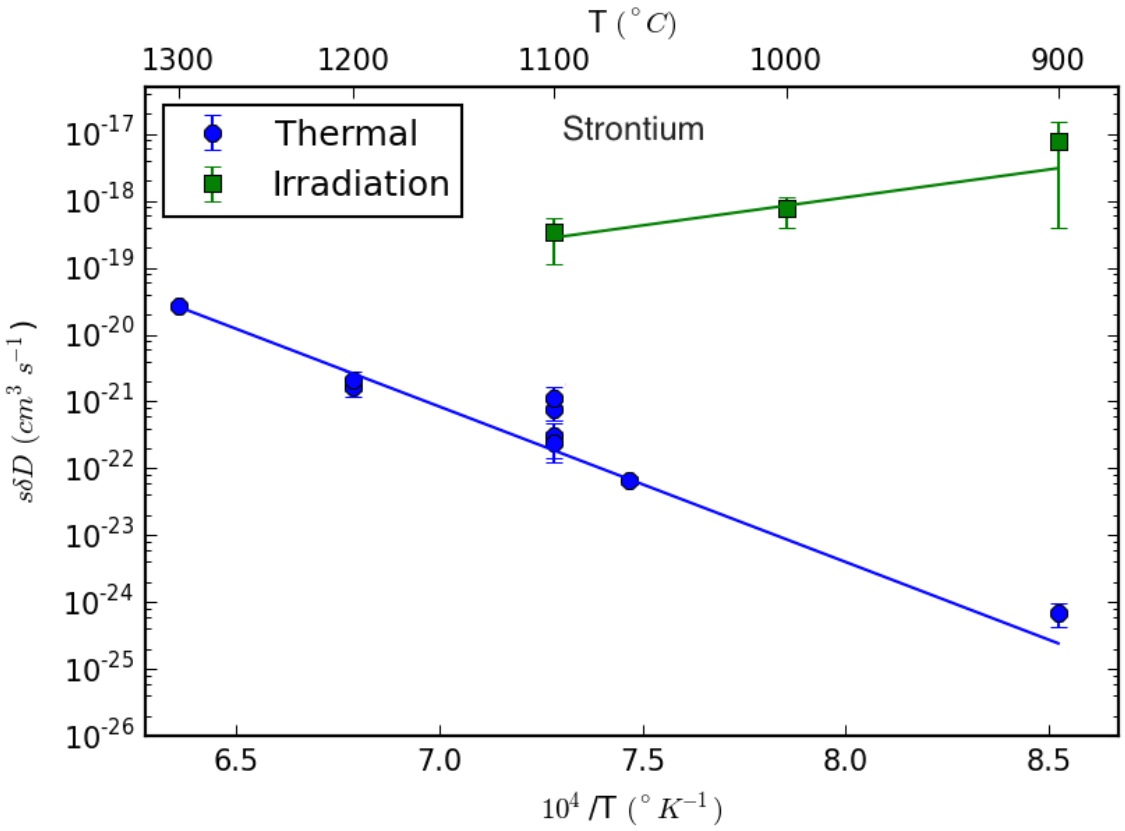

Figure 5.9: Strontium grain boundary thermal and radiation enhanced diffusion.

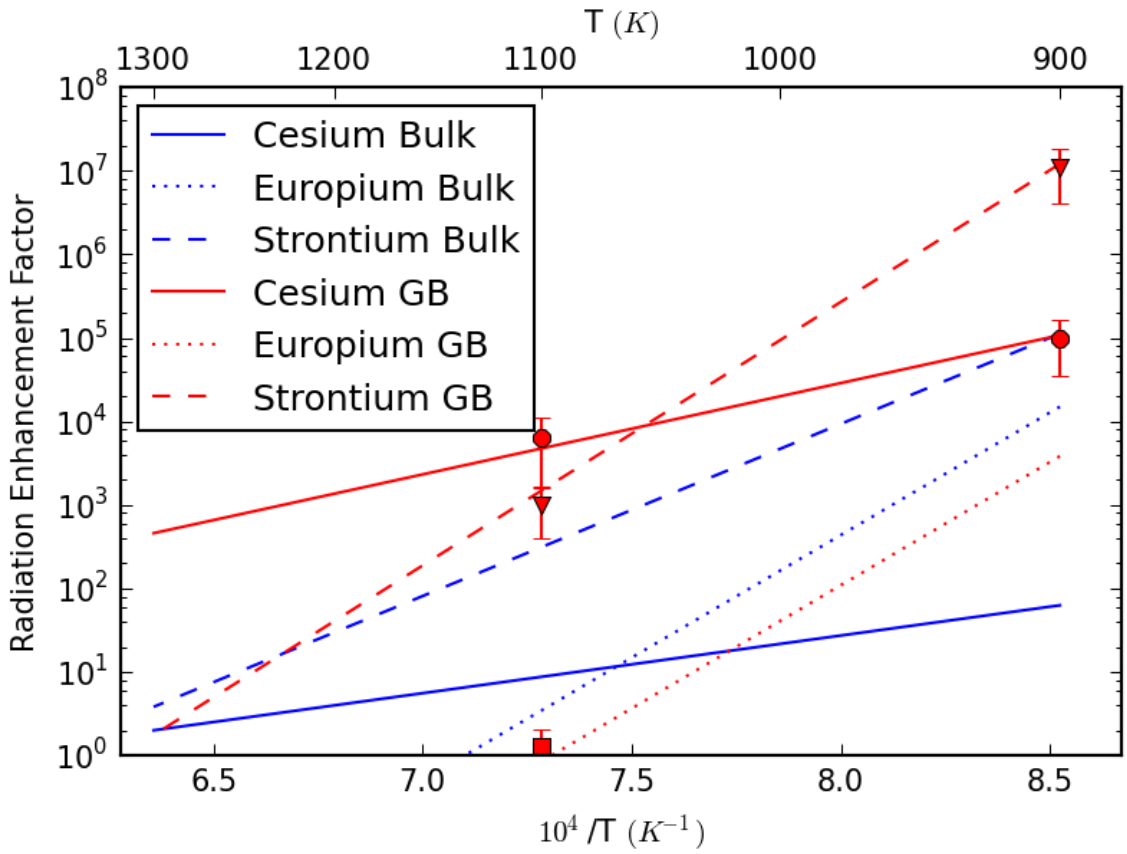

Figure 5.10: Radiation enhancement factor for the bulk and grain boundary diffusion of cesium, strontium and europium

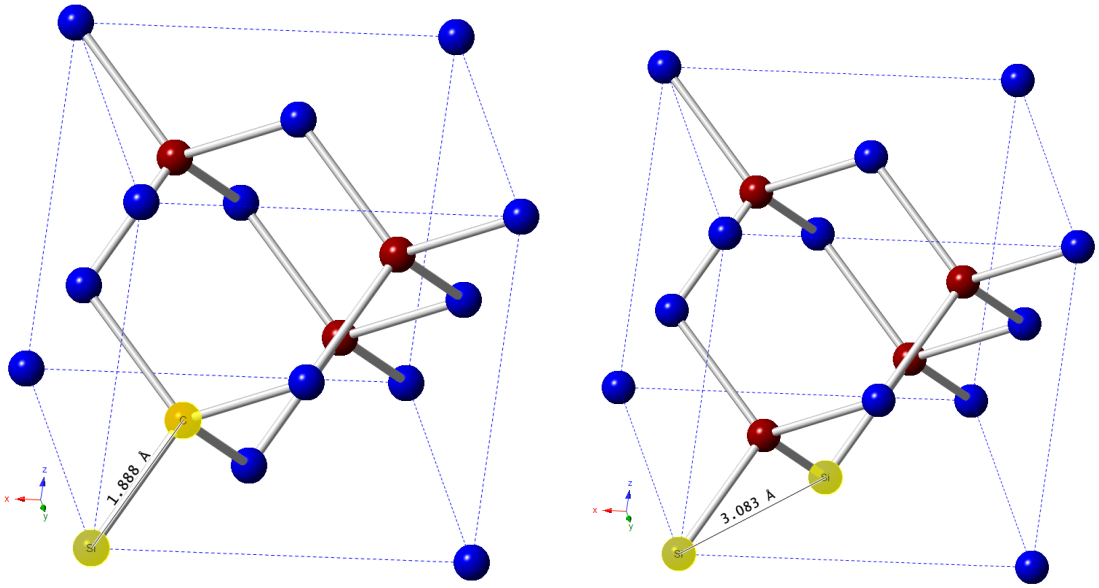

(a) (b)

Figure 5.11: Ball and stick model of the SiC unit cell with carbon in red and silicon in blue labeling (a) the nearest atom distance and (b) the nearest neighbor distance.

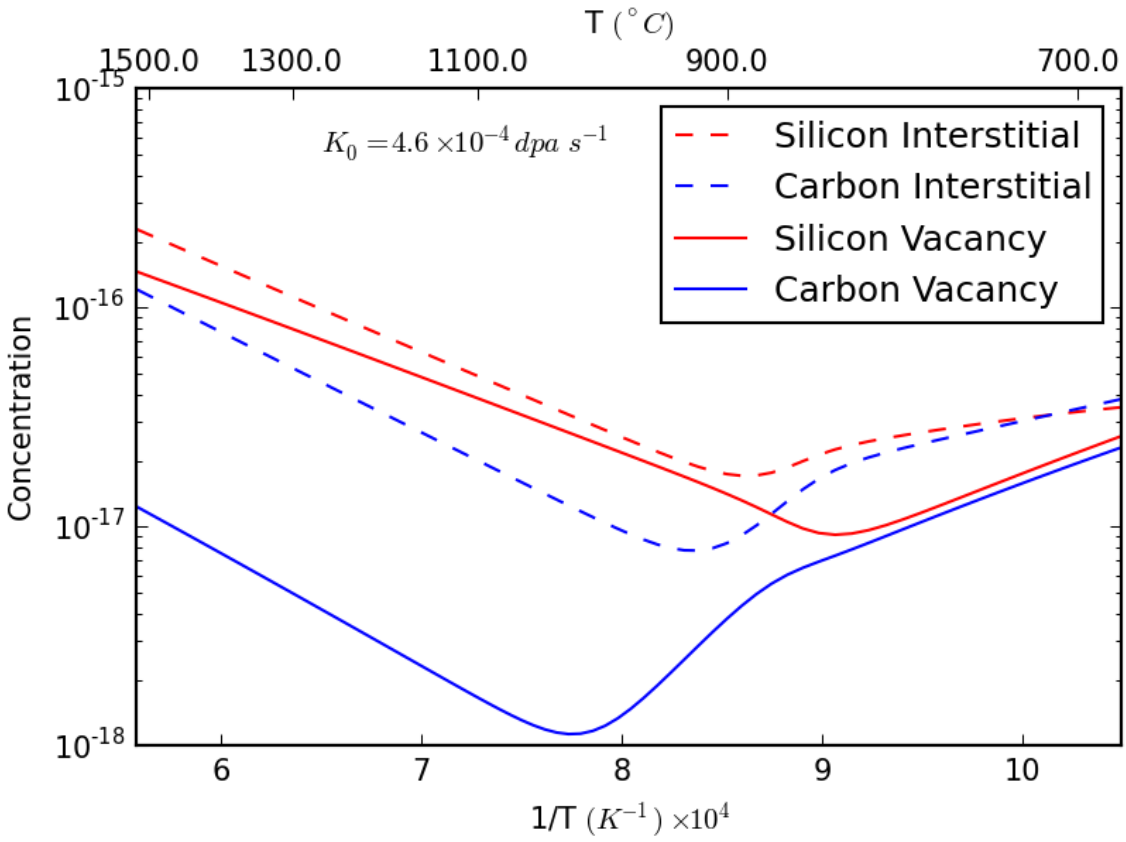

Figure 5.12: Point defect concentrations for SiC under ion irradiation conditions.

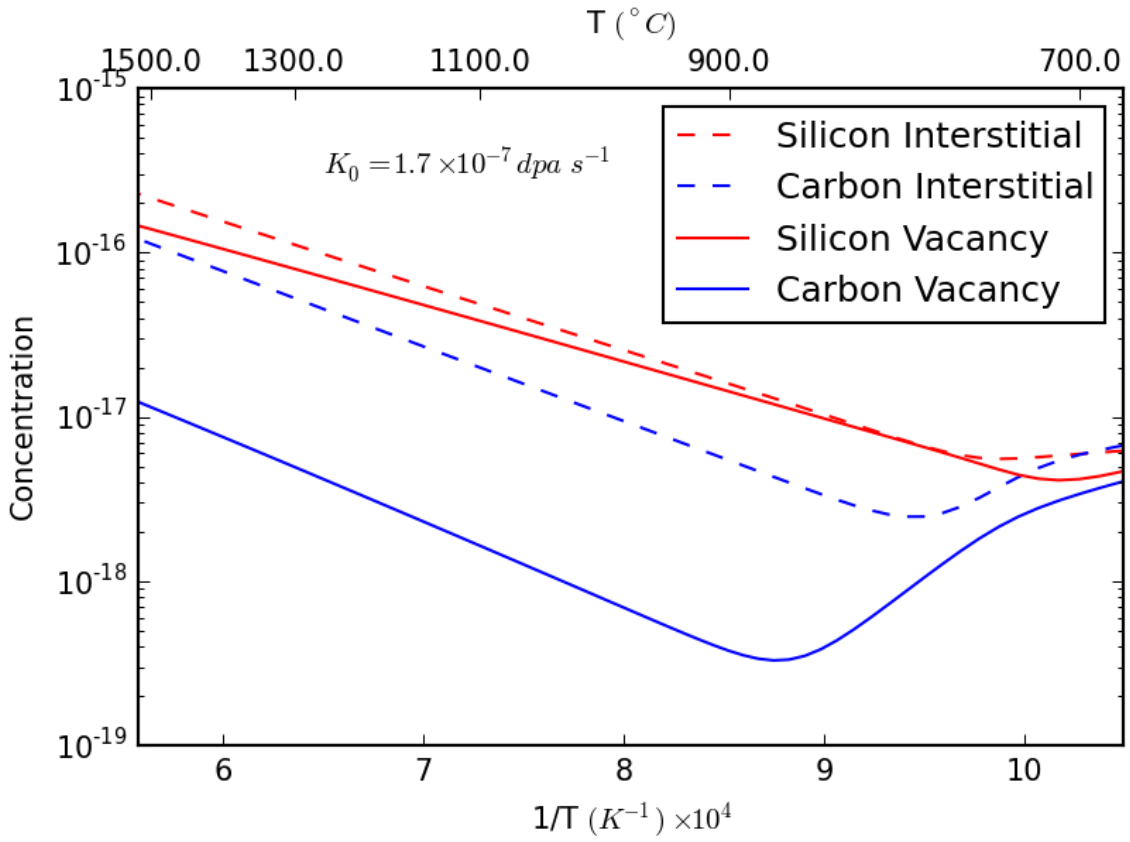

Figure 5.13: Point defect concentrations for SiC under neutron irradiation conditions.

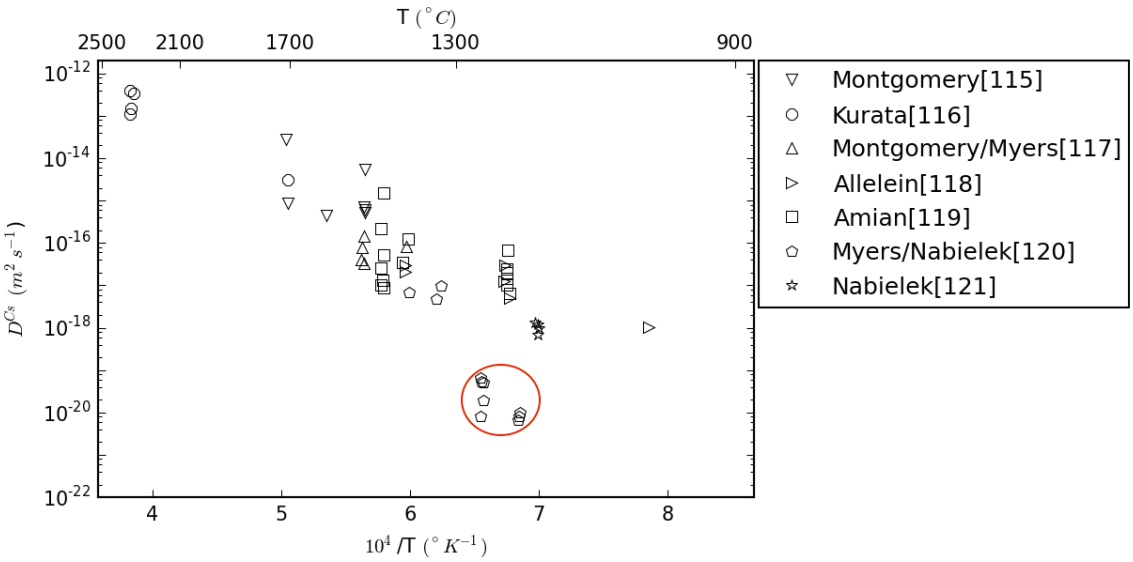

Figure 5.14: Arrhenius plot for cesium diffusion measured using post-irradiation heating experiments [114–121]. The very low release cesium diffusion coefficients from Myers/Nabielek are circled in red

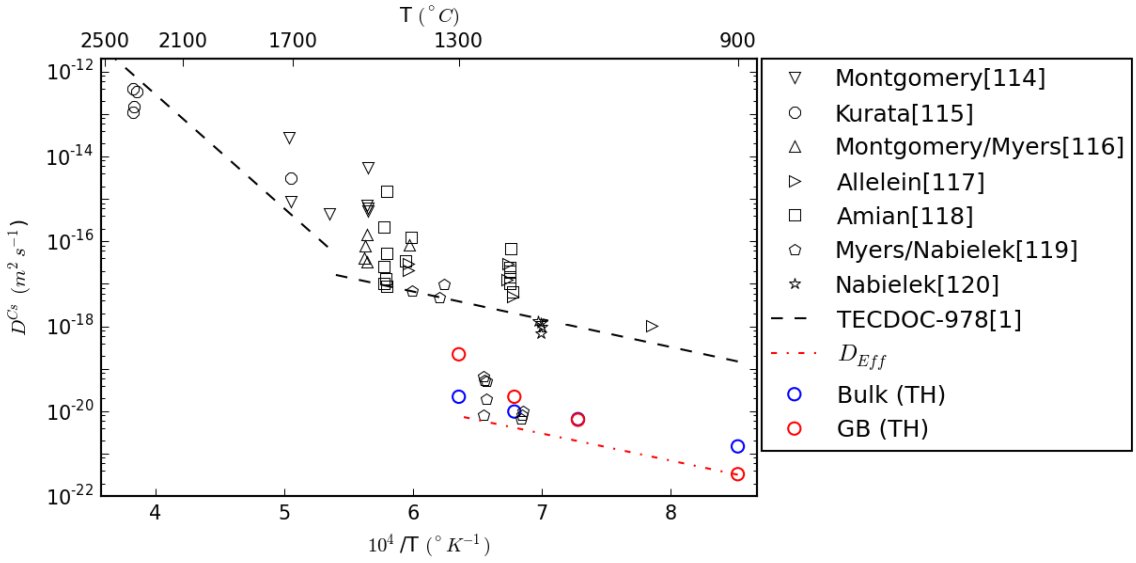

(a)

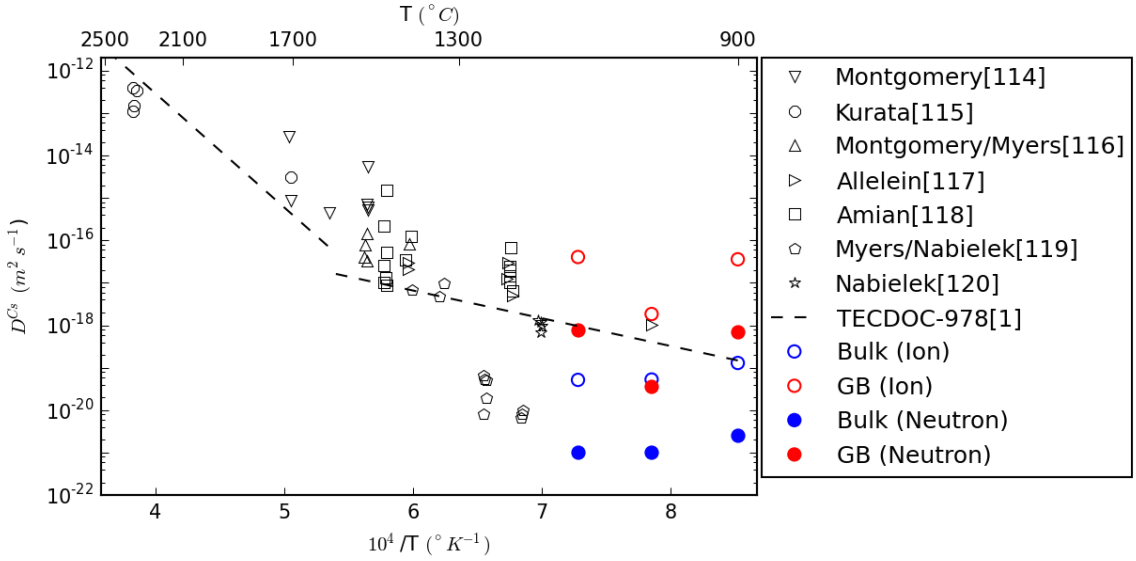

(b)

Figure 5.15: Same plot as 5.14 with (a) thermal bulk and grain boundary diffusion coefficients from this study plotted in red and blue open circles or (b) the ion irradiated bulk and grain boundary RED coefficients plotted in red and blue open circles and closed circles for the dose rate corrected RED coefficients calculated by assuming that the diffusion coefficient scales by the square-root of the dose rate for a ion irradiation dose rate of $4.6 \times 10^{-4} dpa\ s^{-1}$ and a neutron dose rate of $1.7 \times 10^{-7} dpa\ s^{-1}$ [2].

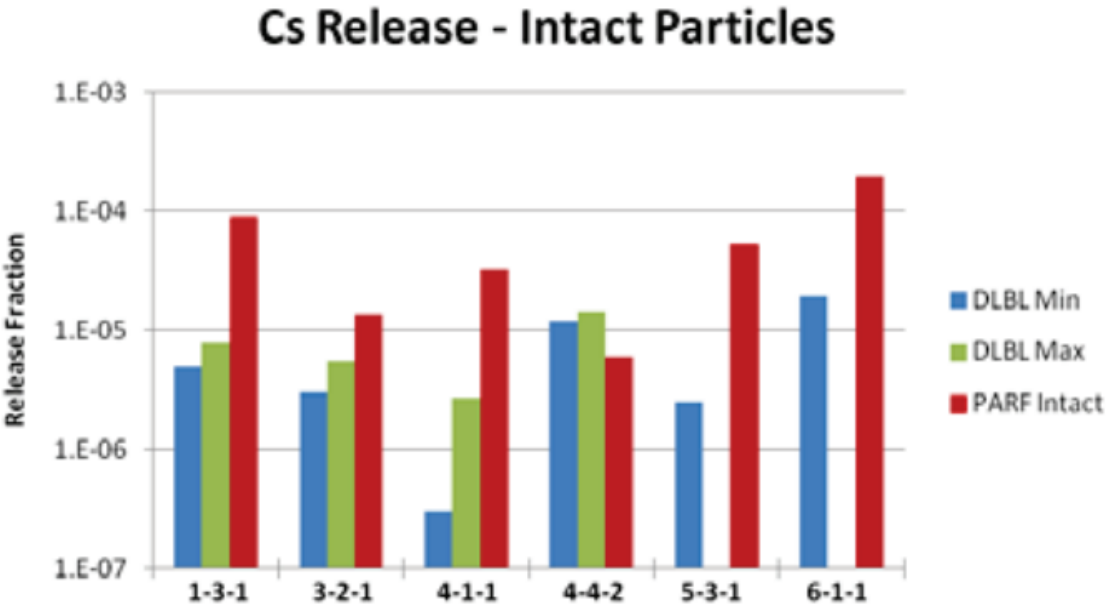

Figure 5.16: Cesium release for 6 compacts that exhibit between 1 and 3 orders of magnitude over-prediction by PARFUME as compared with release measurements made by the deconsolidation-leach-burn-leach method [112].

CHAPTER VI

Conclusion

The major conclusions of this thesis are:

1. A novel multi-layer diffusion couple was developed to investigate the diffusion of fission products in SiC under prototypical very high temperature reactor conditions. This design introduces fission products to SiC below the solubility limit without causing excess radiation damage to the SiC and was successful in retaining enough cesium, europium and strontium between 900°C and 1,300°C for a measureable portion of the implanted fission product to diffuse into the SiC substrate under purely thermal and ion irradiation conditions.

2. Diffusion measurements were performed on cesium, europium, and strontium diffusion in SiC between between 900°C and 1,300°C and were able to resolve bulk diffusion and isolate grain boundary diffusion for all three fission products under purely thermal condition. These are the first successful measurements of fission product diffusion in SiC in nearly 60 years of research investigating fission product release in TRISO fuel.

3. Radiation enhanced diffusion measurements were performed using 4.5 MeV silicon ion irradiation as an emulatant for neutron irradiation. The bulk and grain boundary radiation enhanced diffusion of cesium, europium, and strontium

were measured between 900°C and 1,100°C at a dose rate of $4.6 \times 10^{-4} dpa\ s^{-1}$ and exhibited significant enhancements, ranging from 100× to 10^7×, over thermal diffusion for both bulk and grain boundary diffusion. These are also the first successful measurements of fission product radiation enhanced diffusion in SiC.

4. Cesium, europium, and strontium all exhibit mixed diffusion kinetics between 900°C and 1,300°C under thermal conditions indicating that both bulk and grain boundary mechanisms are active. They also exhibit mixed diffusion kinetics between 900°C and 1,100°C under ion irradiation conditions indicating that both mechanism are active under irradiation as well. Neither mechanism dominates in this temperature range under either set of conditions.

5. A defect reaction model for the point defect concentrations under thermal and irradiation conditions show that both the carbon and silicon sub-lattices are important for fission product diffusion. It indicates that cesium bulk, europium bulk and grain boundary, as well as strontium grain boundary diffusion are likely to proceed on the carbon sub-lattice, while strontium bulk diffusion is likely to proceed via the silicon sub-lattice.

6. The thermal diffusion of cesium measured in this study agrees with the best case cesium diffusion coefficients measured from cesium release from German TRISO fuel, which is well known in the community to have had the lowest defect fraction of all the historic TRISO test campaigns. This further supports the premise that high quality TRISO fuel should exhibit minimal cesium release, and that cesium release is a good indicator of TRISO fuel failure.

CHAPTER VII

Future Work

This dissertation was focused on establishing a methodology to isolate and analyze the diffusion of three key FPs: cesium, europium, and strontium in SiC. These three FPs are important from a radiological health perspective. There are several other FPs that are of importance in order to eventually license TRISO fuel and need to be investigated using the multilayer diffusion couple developed in this study. Iodine and cerium are also important FPs for public health concerns [73]. Silver and palladium are two FPs with significant importance for the operation of any reactor concept utilizing TRISO [12]. Silver shows the most erratic release, while palladium is produced in large quantities and is known to corrode SiC, if present in high enough concentration.

Similarly, the temperature range needs to be expanded to increase the confidence in diffusion coefficients for in-pile and out-of-pile release calculations. This study was limited to $1,300°C$, but TRISO fuel is being designed to be subject to accidents as high as $1,800°C$. The temperature range should also be extended to lower temperatures to accurately measure grain boundary diffusion and determine the segregation energies for FPs. It is very likely that the segregation behavior of FPs provides a better picture of the efficacy of SiC in preventing FP release. The effect of radiation on the segregation energy would also provide a better understanding of how radiation is able

to accelerate grain boundary diffusion.

The dose-rates investigated in the ion irradiation study were very high in order to force an effect of irradiation. A more comprehensive study would perform lower dose-rate ion irradiations to investigate the dose-rate scaling and potential changes in point-defect reaction regimes. This study would also validate the use of ion irradiation as an appropriate accelerated testing method for over-size solute diffusion in SiC.

All of these studies require an improvement in the performance of the diffusion couple itself. Leakage of FPs through the cap was observed in all samples. Higher temperature anneals increased the likelihood of SiC cap loss and in combination with the FP leakage through the cap limited this study to $1,300°C$. The PECVD SiC recipe could be optimized to reduce the hydrogen content of the deposited film and reduce the internal stress. A pre-annealing treatment could be used to slowly recrystallize the SiC cap, creating a more uniform and effective PECVD SiC layer. An improved diffusion couple process might deposit a SiC cap using conventional CVD and then implant through the SiC cap to achieve better retention and the ability to probe diffusion at higher temperatures. Pulsed laser deposition (PLD) could also be a viable low temperature deposition process to extend the utility of this design with minimal changes [122].

Varying the fluence of implanted FP could be used to probe the effect of the PyC/SiC interface which controls both the concentrations of FPs that can diffuse into the SiC and the total rate. There is no information on FP solubilities in SiC in either the bulk or the grain boundaries. Some of this information can be gathered from grain boundary segregation energies, but the thermodynamics across the PyC/SiC interface are also critical to the understanding of FP release phenomena.

The assignment of bulk and grain boundary diffusion has been through the interpretation of the concentration profiles in the context of what is observed in literature for model diffusion systems and TRISO fuel. A second method confirming grain boundary

diffusion via TEM or some other imaging technique would be useful in further supporting this theory and providing information on grain boundary structure. This could also be used to identify if there is a grain boundary structure dependence to FP diffusion in either thermal or RED regime.

Finally, this thesis has investigated FP diffusion via experimental methods, which are limited by the difficulty of the experiments and the resolution and sensitivity of current analytic techniques. Any further mechanistic investigation needs to approach the atomistics via computational methods. The first-of-a-kind activation energies measured here provide a target for DFT calculations for hop mechanisms, grain boundary structural dependencies, and the fundamental mechanisms by which radiation affects FP diffusion. It also indicates which sub-lattice these three FPs diffuse via, narrowing down the number of possible hop mechanisms.

BIBLIOGRAPHY

[1] "TECDOC - 978: Fuel Performance and Fission Product Behaviour in Gas-Cooled Reactors," tech. rep., IAEA, Vienna, 1997.

[2] R. Morris, C. Baldwin, F. Montgomery, T. Gerczak, C. Silva, and J. Hunn, "Performance of AGR-1 Fuel at Elevated Temperature: Fission Product Retention at 1600,1700, and 1800C," in *VHTR R&D*, (Idaho Falls, ID), 2013.

[3] R. Hobbins, D. Petti, P. Demkowicz, and R. Morris, "Preliminary Evaluation of AGR-1 Fission Product Release," in *VHTR R&D*, (Idaho Falls, ID), 2013.

[4] J. Hunn, C. Baldwin, C. Silva, T. Gerczak, F. Montgomery, and R. Morris, "Detecvtion and Analysis of Particles with Abnormal Fission Product Retention," in *VHTR R&D*, (Idaho Falls, ID), 2013.

[5] P. Demkowicz and B. Collin, "AGR-1 Silver Release: Comparison of Experiment with PARFUME Predictions," in *VHTR R&D*, (Idaho Falls, ID), 2013.

[6] K. Minato, T. Ogawa, K. Fukuda, M. Shimizu, Y. Tayama, and I. Takahashi, "Fission product behavior in Triso-coated UO2 fuel particles," *Journal of Nuclear Materials*, vol. 208, pp. 266–281, Feb. 1994.

[7] T. N. Tiegs, "Fission Product Pd-SiC Interaction in Irradiated Coated-Particle Fuels," *Nuclear Technology*, vol. 57, pp. 389–398, June 1982.

[8] R. Bullock, "Fission-product release during postirradiation annealing of several types of coated fuel particles," *Journal of Nuclear Materials*, vol. 125, pp. 304–319, Aug. 1984.

[9] I. van Rooyen, D. Janney, B. Miller, P. Demkowicz, and J. Riesterer, "Electron microscopic evaluation and fission product identification of irradiated TRISO coated particles from the AGR-1 experiment: A preliminary review," *Nuclear Engineering and Design*, vol. 271, pp. 114–122, May 2014.

[10] T. J. Gerczak, L. Tan, T. R. Allen, S. Khalil, D. Shrader, Y. Liu, D. Morgan, and I. Szlufarska, "Experimental and simulation insight on the transport of silver fission product in SiC - HTR2008-58131," 2008.

[11] J. van der Merwe, "Evaluation of silver transport through SiC during the German HTR fuel program," *Journal of Nuclear Materials*, vol. 395, pp. 99–111, Dec. 2009.

[12] D. Petti, J. Buongiorno, J. Maki, R. Hobbins, and G. Miller, "Key differences in the fabrication, irradiation and high temperature accident testing of US and German TRISO-coated particle fuel, and their implications on fuel performance," *Nuclear Engineering and Design*, vol. 222, pp. 281–297, June 2003.

[13] L. L. Snead, T. Nozawa, Y. Katoh, T.-S. Byun, S. Kondo, and D. A. Petti, "Handbook of SiC properties for fuel performance modeling," *Journal of Nuclear Materials*, vol. 371, pp. 329–377, Sept. 2007.

[14] D. Shrader, S. M. Khalil, T. Gerczak, T. R. Allen, A. J. Heim, I. Szlufarska, and D. Morgan, "Ag diffusion in cubic silicon carbide," *Journal of Nuclear Materials*, vol. 408, pp. 257–271, Jan. 2011.

[15] R. M. Van Ginhoven, A. Chartier, C. Meis, W. J. Weber, and L. René Corrales, "Theoretical study of helium insertion and diffusion in 3C-SiC," *Journal of Nuclear Materials*, vol. 348, pp. 51–59, Jan. 2006.

[16] T. Oda, Y. Zhang, and W. J. Weber, "Study of intrinsic defects in 3C-SiC using first-principles calculation with a hybrid functional.," *The Journal of chemical physics*, vol. 139, p. 124707, Sept. 2013.

[17] A. Mattausch, M. Bockstedte, and O. Pankratov, "Interstitials in SiC: a model for the DII center," *Physica B: Condensed Matter*, vol. 308-310, pp. 656–659, Dec. 2001.

[18] M. Bockstedte, A. Mattausch, and O. Pankratov, "Ab initio study of the migration of intrinsic defects in 3 C SiC," *Physical Review B*, vol. 68, p. 205201, Nov. 2003.

[19] A. Zywietz, J. Furthmüller, and F. Bechstedt, "Vacancies in SiC: Influence of Jahn-Teller distortions, spin effects, and crystal structure," *Physical Review B*, vol. 59, pp. 15166–15180, June 1999.

[20] B. Aradi, A. Gali, P. Deák, J. E. Lowther, N. T. Son, E. Janzén, and W. J. Choyke, "Ab initio density-functional supercell calculations of hydrogen defects in cubic SiC," *Physical Review B*, vol. 63, p. 245202, May 2001.

[21] L. Torpo, T. E. M. Staab, and R. M. Nieminen, "Divacancy in 3 C and 4 H SiC : An extremely stable defect," *Physical Review B*, vol. 65, p. 085202, Jan. 2002.

[22] C. Wang, J. Bernholc, and R. F. Davis, "Formation energies, abundances, and the electronic structure of native defects in cubic SiC," *Physical Review B*, vol. 38, pp. 12752–12755, Dec. 1988.

[23] W. Weber, "Total displacement functions for SiC," *Journal of Nuclear Materials*, vol. 244, pp. 205–211, Apr. 1997.

[24] R. Devanathan, "Displacement threshold energies in β-SiC," *Journal of Nuclear Materials*, vol. 253, pp. 47–52, Mar. 1998.

[25] W. Windl, T. Lenosky, J. Kress, and A. Voter, "First-principles study of point-defect production in Si and SiC," Mar. 1998.

[26] R. Devanathan, "Displacement energy surface in 3C and 6H SiC," *Journal of Nuclear Materials*, vol. 278, pp. 258–265, Apr. 2000.

[27] J. Perlado, "Analysis of displacement cascades and threshold displacement energies in β-sic," *Journal of Nuclear Materials*, vol. 276, pp. 235–242, Jan. 2000.

[28] F. Gao and W. Weber, "Atomic-scale simulation of 50 keV Si displacement cascades in β-SiC," *Physical Review B*, vol. 63, Dec. 2000.

[29] F. Gao, "Native defect properties in β-SiC: Ab initio and empirical potential calculations," *Nuclear Instruments and Methods in Physics Research Section B: Beam Interactions with Materials and Atoms*, vol. 180, pp. 286–292, June 2001.

[30] F. Gao and W. J. Weber, "Computer simulation of disordering and amorphization by Si and Au recoils in 3C–SiC," *Journal of Applied Physics*, vol. 89, no. 8, p. 4275, 2001.

[31] F. Gao, E. Bylaska, W. Weber, and L. Corrales, "Ab initio and empirical-potential studies of defect properties in 3C-SiC," *Physical Review B*, vol. 64, Dec. 2001.

[32] F. Gao and W. Weber, "Cascade overlap and amorphization in 3C-SiC: Defect accumulation, topological features, and disordering," *Physical Review B*, vol. 66, July 2002.

[33] H. Heinisch, L. Greenwood, W. Weber, and R. Williford, "Displacement damage cross sections for neutron-irradiated silicon carbide," *Journal of Nuclear Materials*, vol. 307-311, pp. 895–899, Dec. 2002.

[34] L. Malerba and J. Perlado, "Basic mechanisms of atomic displacement production in cubic silicon carbide: A molecular dynamics study," *Physical Review B*, vol. 65, Jan. 2002.

[35] M. Sawan, L. Snead, and S. Zinkle, "Radiation Damage Parameters for SiC/SiC Composite Structure in Fusion Nuclear Environment," *Fusion Science and Technology*, vol. 44, July 2003.

[36] H. L. Heinisch, L. R. Greenwood, W. J. Weber, and R. E. Williford, "Total DPA Cross Sections for SiC as a Function of Neutron Energy," Mar. 2003.

[37] F. Gao, W. Weber, M. Posselt, and V. Belko, "Atomistic study of intrinsic defect migration in 3C-SiC," *Physical Review B*, vol. 69, June 2004.

[38] R. Devanathan, F. Gao, and W. J. Weber, "Amorphization of silicon carbide by carbon displacement," *Applied Physics Letters*, vol. 84, p. 3909, Apr. 2004.

[39] G. Lucas and L. Pizzagalli, "Ab initio molecular dynamics calculations of threshold displacement energies in silicon carbide," *Physical Review B*, vol. 72, Oct. 2005.

[40] F. Gao, H. Xiao, X. Zu, M. Posselt, and W. Weber, "Defect-Enhanced Charge Transfer by Ion-Solid Interactions in SiC using Large-Scale Ab Initio Molecular Dynamics Simulations," *Physical Review Letters*, vol. 103, July 2009.

[41] R. Devanathan, W. J. Weber, and F. Gao, "Atomic scale simulation of defect production in irradiated 3C-SiC," *Journal of Applied Physics*, vol. 90, no. 5, p. 2303, 2001.

[42] N. Swaminathan, P. J. Kamenski, D. Morgan, and I. Szlufarska, "Effects of grain size and grain boundaries on defect production in nanocrystalline 3C–SiC," *Acta Materialia*, vol. 58, pp. 2843–2853, May 2010.

[43] L. Malerba, "Molecular dynamics simulation of defect production in irradiated $beta;-SiC," *Journal of Nuclear Materials*, vol. 283-287, pp. 794–798, Dec. 2000.

[44] J. Perlado, "Behavior and computer simulation of SiC under irradiation with energetic particles," *Journal of Nuclear Materials*, vol. 251, pp. 98–106, Nov. 1997.

[45] R. Devanathan, W. Weber, and T. Diaz de la Rubia, "Computer simulation of a 10 keV Si displacement cascade in SiC," *Nuclear Instruments and Methods in Physics Research Section B: Beam Interactions with Materials and Atoms*, vol. 141, pp. 118–122, May 1998.

[46] J. C. Fisher, "Calculation of Diffusion Penetration Curves for Surface and Grain Boundary Diffusion," *Journal of Applied Physics*, vol. 22, p. 74, Apr. 1951.

[47] L. G. Harrison, "Influence of dislocations on diffusion kinetics in solids with particular reference to the alkali halides," *Transactions of the Faraday Society*, vol. 57, p. 1191, Jan. 1961.

[48] D. Gryaznov, J. Fleig, and J. Maier, "An improved procedure for determining grain boundary diffusion coefficients from averaged concentration profiles," *Journal of Applied Physics*, vol. 103, p. 063717, Mar. 2008.

[49] R. E. Hoffman and D. Turnbull, "Lattice and Grain Boundary Self-Diffusion in Silver," *Journal of Applied Physics*, vol. 22, p. 634, Apr. 1951.

[50] R. E. Hoffman and D. Turnbull, "Effect of Impurities on the Self-Diffusion of Silver," *Journal of Applied Physics*, vol. 23, p. 1409, June 1952.

[51] J. Sommer, C. Herzig, S. Mayer, and W. Gust, "Grain Boundary Self-Diffusion in Silver Bicrystals," in *Defect and Diffusion Forum*, vol. 66-69, pp. 843–848.

[52] G. Mathieu, P. Gas, A. Combe-Brun, and J. Bernardini, "Bulk and grain boundary self diffusion of silver in Ag-O solid solutions," *Acta Metallurgica*, vol. 31, pp. 1661–1667, Oct. 1983.

[53] Y. Mishin and C. Herzig, "Grain boundary diffusion: recent progress and future research," *Materials Science and Engineering: A*, vol. 260, pp. 55–71, Feb. 1999.

[54] J. Sommer and C. Herzig, "Direct determination of grain-boundary and dislocation self-diffusion coefficients in silver from experiments in type-C kinetics," *Journal of Applied Physics*, vol. 72, p. 2758, Oct. 1954.

[55] J. Mimkes and M. Wuttig, "Exact Solution for a Model of Dislocation Pipe Diffusion," *Physical Review B*, vol. 2, pp. 1619–1623, Sept. 1970.

[56] J. Robinson and N. Peterson, "Correlation effects in grain boundary diffusion," *Surface Science*, vol. 31, pp. 586–616, June 1972.

[57] A. M. Walker, F. Zhang, K. Wright, and J. D. Gale, "Magnesium Vacancy Segregation and Fast Pipe Diffusion for the {110} Edge Dislocation in MgO," Dec. 2009.

[58] E. Budke, C. Herzig, S. Prokofjev, and L. Shvindlerman, "Orientation dependence of 195-au and 64-cu diffusion along symmetric [001] tilt grain boundaries in cu," *Materials Science Forums*, vol. 207-209, pp. 465–468, 1996.

[59] A. Suzuki and Y. Mishin, "Atomic mechanisms of grain boundary diffusion: Low versus high temperatures," *Journal of Materials Science*, vol. 40, pp. 3155–3161, June 2005.

[60] Y. Mishin, "An Atomistic View of Grain Boundary Diffusion," in *Defect and Diffusion Forum*, vol. 363, pp. 1–11, May 2015.

[61] H. Nabielek, P. E. Brown, and P. Offermann, "Silver release from coated particle fuel," *Nuclear Technology*, vol. 35, pp. 483–493, Sept. 1977.

[62] W. Schenk, G. Pott, and H. Nabielek, "Fuel accident performance testing for small HTRs," *Journal of Nuclear Materials*, vol. 171, pp. 19–30, Apr. 1990.

[63] E. Kampshoff, N. Wlchli, and K. Kern, "Silicide formation at palladium surfaces. part i: Crystalline and amorphous silicide growth at the pd(110) surface," *Surface Science*, vol. 406, no. 13, pp. 103 – 116, 1998.

[64] G. Méric de Bellefon and B. Wirth, "Kinetic Monte Carlo (KMC) simulation of fission product silver transport through TRISO fuel particle," *Journal of Nuclear Materials*, vol. 413, pp. 122–131, June 2011.

[65] H. J. MacLean, *Silver transport in CVD silicon carbide*. PhD thesis, Massachusetts Institute of Technology, 2004.

[66] E. López-Honorato, D. Yang, J. Tan, P. J. Meadows, and P. Xiao, "Silver Diffusion in Coated Fuel Particles," *Journal of the American Ceramic Society*, vol. 93, pp. 3076–3079, Oct. 2010.

[67] E. López-Honorato, H. Zhang, D. Yang, and P. Xiao, "Silver Diffusion in Silicon Carbide Coatings," *Journal of the American Ceramic Society*, vol. 94, pp. 3064–3071, Sept. 2011.

[68] L. Jian-Guo, "Wettability of silicon carbide by liquid silver and binary silver-silicon alloy," *Materials Letters*, vol. 18, pp. 291–298, Feb. 1994.

[69] E. Olivier and J. Neethling, "The role of Pd in the transport of Ag in SiC," *Journal of Nuclear Materials*, vol. 432, pp. 252–260, Jan. 2013.

[70] E. Olivier and J. Neethling, "Palladium transport in SiC," *Nuclear Engineering and Design*, vol. 244, pp. 25–33, Mar. 2012.

[71] J. T. Maki, D. A. Petti, D. L. Knudson, and G. K. Miller, "The challenges associated with high burnup, high temperature and accelerated irradiation for TRISO-coated particle fuel," *Journal of Nuclear Materials*, vol. 371, pp. 270–280, Sept. 2007.

[72] E. Friedland, J. Malherbe, N. van der Berg, T. Hlatshwayo, A. Botha, E. Wendler, and W. Wesch, "Study of silver diffusion in silicon carbide," *Journal of Nuclear Materials*, vol. 389, pp. 326–331, May 2009.

[73] D. Petti, "Implications of Results from the Advanced Gas Reactor Fuel Development and Qualification Program on Licensing of Modular HTGRs," in *HTR 2014*, (Weihai), 2014.

[74] V. Shankar and G. S. Was, "Proton irradiation creep of beta-silicon carbide," *Journal of Nuclear Materials*, vol. 418, pp. 198–206, Nov. 2011.

[75] R. Kirchhofer, J. D. Hunn, P. A. Demkowicz, J. I. Cole, and B. P. Gorman, "Microstructure of {TRISO} coated particles from the agr-1 experiment: Sic grain size and grain boundary character," *Journal of Nuclear Materials*, vol. 432, no. 13, pp. 127 – 134, 2013.

[76] L. Tan, T. Allen, J. Hunn, and J. Miller, "EBSD for microstructure and property characterization of the SiC-coating in TRISO fuel particles," *Journal of Nuclear Materials*, vol. 372, pp. 400–404, Jan. 2008.

[77] J. Lim, B.-Y. Jeon, and C. Lee, "Post-CMP Cleaning of Metallic Contaminant Removal by Using a Remote Plasma and UV/Ozone," *Journal of Korean Physical Society*, vol. 37, no. 6, p. 1051˜1056, 2000.

[78] J. Sterbentz, "JMOCUP as-Run Daily Depletion Caluclation for the AGR-1 Experiment in ATR B-10 Position," Tech. Rep. INL-11-23655, NGNP, 2011.

[79] B. A. Gurovich and K. E. Prikhodko, "Investigation of dose-temperature dependencies of graphite dimensional and lattice parameters changes under electron irradiation," *Radiation Effects and Defects in Solids*, vol. 154, pp. 39–60, June 2001.

[80] A. Matsunaga, C. Kinoshita, K. Nakai, and Y. Tomokiyo, "Radiation-induced amorphization and swelling in ceramics," *Journal of Nuclear Materials*, vol. 179-181, pp. 457–460, Mar. 1991.

[81] J. F. Ziegler, M. Ziegler, and J. Biersack, "SRIM – The stopping and range of ions in matter (2010)," *Nuclear Instruments and Methods in Physics Research Section B: Beam Interactions with Materials and Atoms*, vol. 268, pp. 1818–1823, June 2010.

[82] R. E. Stoller, M. B. Toloczko, G. S. Was, A. G. Certain, S. Dwaraknath, and F. A. Garner, "On the use of SRIM for computing radiation damage exposure," *Nuclear Instruments and Methods in Physics Research, Section B: Beam Interactions with Materials and Atoms*, vol. 310, pp. 75–80, Sept. 2013.

[83] G. S. Was, *Fundamentals of Radiation Materials Science: Metals and Alloys*. Springer Science & Business Media, 2007.

[84] J. Lindhard and M. Scharff, "Energy dissipation by ions in the kev region," *Physical Review*, vol. 124, no. 1, p. 128, 1961.

[85] T. Jeong, J.-G. Zhu, S. Mao, T. Pan, and Y. J. Tang, "Thermal Characterization of SiC Amorphous Thin Films," *International Journal of Thermophysics*, vol. 33, pp. 1000–1012, Apr. 2012.

[86] E. López-Honorato, C. Chiritescu, P. Xiao, D. G. Cahill, G. Marsh, and T. Abram, "Thermal conductivity mapping of pyrolytic carbon and silicon carbide coatings on simulated fuel particles by time-domain thermoreflectance," *Journal of Nuclear Materials*, vol. 378, pp. 35–39, Aug. 2008.

[87] A. D. L. Claire, "The analysis of grain boundary diffusion measurements," *British Journal of Applied Physics*, vol. 14, pp. 351–356, June 1963.

[88] R. Whipple, "CXXXVIII. Concentration contours in grain boundary diffusion," *The London, Edinburgh, and Dublin Philosophical Magazine and Journal of Science*, vol. 45, pp. 1225–1236, Apr. 1954.

[89] E. Jones, T. Oliphant, P. Peterson, and Others, "{SciPy}: Open source scientific tools for {Python}."

[90] D. S. Kim and Y. H. Lee, "Annealing effects on a-SiC:H and a-SiC:H(F) thin films deposited by PECVD at room temperature," *Thin Solid Films*, vol. 261, pp. 192–201, June 1995.

[91] E. Friedland, N. van der Berg, T. Hlatshwayo, R. Kuhudzai, J. Malherbe, E. Wendler, and W. Wesch, "Diffusion behavior of cesium in silicon carbide at T¿1000 °C," *Nuclear Instruments and Methods in Physics Research Section B: Beam Interactions with Materials and Atoms*, vol. 286, pp. 102–107, Sept. 2012.

[92] E. Friedland, N. van der Berg, J. Malherbe, E. Wendler, and W. Wesch, "Influence of radiation damage on strontium and iodine diffusion in silicon carbide," *Journal of Nuclear Materials*, vol. 425, pp. 205–210, June 2012.

[93] E. Friedland, T. Hlatshwayo, and N. van der Berg, "Influence of radiation damage on diffusion of fission products in silicon carbide," *physica status solidi (c)*, vol. 10, pp. 208–215, Feb. 2013.

[94] J. Bernardini, P. Gas, E. D. Hondros, and M. P. Seah, "The Role of Solute Segregation in Grain Boundary Diffusion," *Proceedings of the Royal Society A: Mathematical, Physical and Engineering Sciences*, vol. 379, pp. 159–178, Jan. 1982.

[95] J. R. Farver and R. A. Yund, "Measurement of oxygen grain boundary diffusion in natural, fine-grained, quartz aggregates," *Geochimica et Cosmochimica Acta*, vol. 55, pp. 1597–1607, June 1991.

[96] A. C. S. Sabioni, A. M. Huntz, F. Millot, and C. Monty, "Self-diffusion in cr 2 o 3 III. Chromium and oxygen grain-boundary diffusion in polycrystals," *Philosophical Magazine A*, vol. 66, pp. 361–374, Sept. 1992.

[97] J. Askill and G. B. Gibbs, "Tracer Diffusion in β-Titanium," *physica status solidi (b)*, vol. 11, no. 2, pp. 557–565, 1965.

[98] K. Maier, H. Mehrer, E. Lessmann, and W. Schüle, "Self-diffusion in nickel at low temperatures," *physica status solidi (b)*, vol. 78, pp. 689–698, Dec. 1976.

[99] I. van Rooyen, T. Lillo, and Y. Wu, "Identification of silver and palladium in irradiated TRISO coated particles of the AGR-1 experiment," *Journal of Nuclear Materials*, vol. 446, pp. 178–186, Mar. 2014.

[100] I. J. van Rooyen, E. Olivier, J. H. Neethlin, I. J. van Rooyen, E. Olivier, and J. H. Neethlin, "Investigation of the Distribution of Fission Products Silver, Palladium and Cadmium in Neutron Irradiated SIC using a Cs Corrected HRTEM," Oct. 2014.

[101] D. Shrader, I. Szlufarska, and D. Morgan, "Cs diffusion in cubic silicon carbide," *Journal of Nuclear Materials*, vol. 421, pp. 89–96, Feb. 2012.

[102] D. McLean, *Grain boundaries in metals*. Clarendon Press, 1957.

[103] M. P. Seah and E. D. Hondros, "Grain Boundary Segregation," *Proceedings of the Royal Society A: Mathematical, Physical and Engineering Sciences*, vol. 335, pp. 191–212, Oct. 1973.

[104] J. Rabone and A. Kovács, "A DFT investigation of the interactions of Pd, Ag, Sn, and Cs with silicon carbide," *International Journal of Quantum Chemistry*, vol. 114, pp. 1534–1545, Nov. 2014.

[105] D. P. Birnie, "A Model for Silicon Self-Diffusion in Silicon Carbide: Anti-Site Defect Motion," *Journal of the American Ceramic Society*, vol. 69, pp. C–33–C–35, Feb. 1986.

[106] M. H. Hon and R. F. Davis, "Self-diffusion of14C in polycrystalline β-SiC," *Journal of Materials Science*, vol. 14, pp. 2411–2421, Oct. 1979.

[107] M. H. Hon, R. F. Davis, and D. E. Newbury, "Self-diffusion of 30Si in polycrystalline ?-SiC," *Journal of Materials Science*, vol. 15, pp. 2073–2080, Aug. 1980.

[108] S. Dwaraknath and G. S. Was, "Development of a multi-layer diffusion couple to study fission product transport in β-SiC," *Journal of Nuclear Materials*, vol. 444, no. 1-3, pp. 170–174, 2014.

[109] K. Fukuda and K. Iwamoto, "Concentration profiles of fission products in the coating layers of irradiated fuel particles," *Journal of Nuclear Materials*, vol. 66, pp. 55–64, Apr. 1977.

[110] A. N. Gudkov, V. A. Kashparov, A. A. Kotlyarov, N. N. Ponomarev-Stepnoi, I. G. Prikhod'ko, and A. A. Khrulev, "Behavior of solid fission products in coated fuel particles of a high-temperature gas-cooled reactor," *Soviet Atomic Energy*, vol. 67, pp. 594–599, Aug. 1989.

[111] W. Amian and D. Stöver, "Diffusion of Silver and Cesium in Silicon-Carbide Coatings of Fuel Particles for High-Temperature Gas-Cooled Reactors," *Nuclear Technology*, vol. 61, pp. 475–486, June 1983.

[112] B. Collin, "Comparison of fission product release predictions using PARFUME with results from the AGR-1 irradiation experiment," Tech. Rep. INL-14-31976, Idaho National Laboratory, Idaho Falls, ID (United States), Sept. 2014.

[113] J. Kalnin, E. Kotomin, and J. Maier, "Calculations of the effective diffusion coefficient for inhomogeneous media," *Journal of Physics and Chemistry of Solids*, vol. 63, no. 3, pp. 449 – 456, 2002.

[114] R. Martin, "Compilation of Fuel Performance and Fission Product Transport Models and Database for MHTGR Design," Tech. Rep. ORNL/NPR-91/6, Oak Ridge National Laboratory (ORNL), Oak Ridge, TN, Oct. 1993.

[115] F. Montgomery, "Fission-product sic reaction in htgr fuel," tech. rep., General Atomic Co., San Diego, CA (USA), 1981.

[116] Y. Kurata, K. Ikawa, and K. Iwamoto, "Fission product release from triso-coated uo 2 particles at 1940 to 2320 c," *Journal of Nuclear Materials*, vol. 98, no. 1, pp. 107–115, 1981.

[117] F. MONTGOMERY, B. MYERS, and N. PACKAN, "Hrb-22 capsule irradiation test for htgr fuel (jaeri/usdoe collaborative irradiation test)," *JAERI-Research*, vol. 98, p. 021, 1998.

[118] H. ALLELEIN, "Fission product behavior in particular 137csin htr-triso-coated particle fuel," *Jiil-1695, Kernforschungsanlage Julich (Dec. 1980)(in German)*.

[119] W. Amian and D. Stöver, "Diffusion of silver and cesium in silicon-carbide coatings of fuel particles for high-temperature gas-cooled reactors," *Nuclear Technology*, vol. 61, no. 3, pp. 475–486, 1983.

[120] H. Nabielek and B. Myers, "Fission product retention in htr fuel," in *Gas-cooled reactors today (Vol. 2). Advances in fuel, core and structural materials*, 1982.

[121] R. Gontard and H. Nabielek, "Performance evaluation of modern htr triso fuels," *Forschungszentrum Jülich GmbH, HTA-IB-05/90*, 1990.

[122] A.-M. Reinecke, M. Lustfeld, W. Lippmann, and A. Hurtado, "Creation of leak-proof silicon carbide diffusion barriers by means of pulsed laser deposition," *Nuclear Engineering and Design*, vol. 271, pp. 92–98, May 2014.